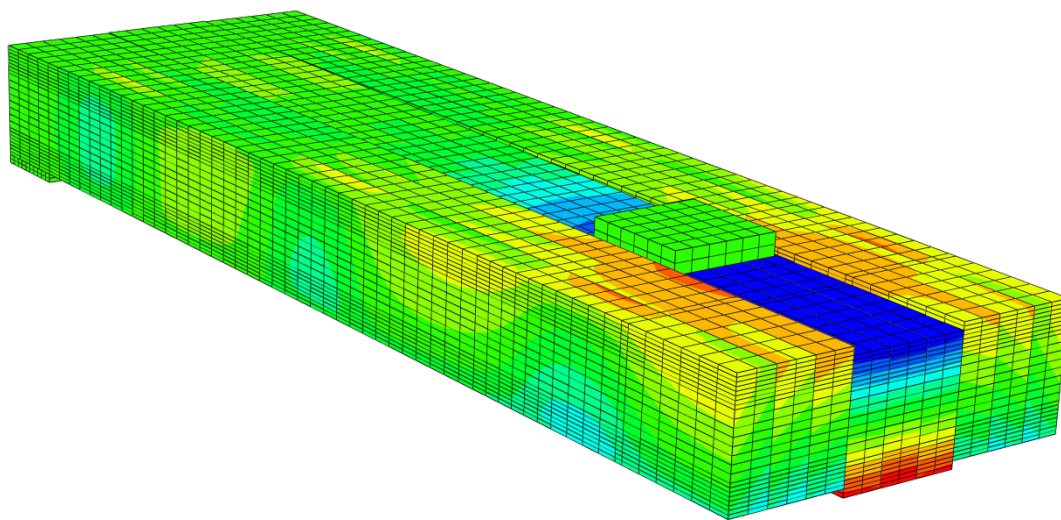


# CHALMERS



## Finite Element Modelling of Interlaminar Slip in Stress-Laminated Timber Decks

Friction Interaction Modelling Using Abaqus

*Master of Science Thesis in the Master's Programme Structural Engineering and Building Performance Design*

JOAKIM CARLBERG  
BINYAM TOYIB

Department of Civil and Environmental Engineering  
*Division of Structural Engineering*  
*Steel and Timber Structures*  
CHALMERS UNIVERSITY OF TECHNOLOGY  
Göteborg, Sweden 2012  
Master's Thesis 2012:77



MASTER'S THESIS 2012:77

# Finite Element Modelling of Interlaminar Slip in Stress-Laminated Timber Decks

Friction Interaction Modelling Using Abaqus

*Master of Science Thesis in the Master's Programme Structural Engineering and Building Performance Design*

JOAKIM CARLBERG

BINYAM TOYIB

Department of Civil and Environmental Engineering  
*Division of Structural Engineering*  
*Steel and Timber Structures*

CHALMERS UNIVERSITY OF TECHNOLOGY  
Göteborg, Sweden 2012

Finite Element Modelling of Interlaminar Slip in Stress-Laminated Timber Decks  
Friction Interaction Modelling Using Abaqus

*Master of Science Thesis in the Master's Programme Structural Engineering and  
Building Performance Design*

JOAKIM CARLBERG

BINYAM TOYIB

© JOAKIM CARLBERG & BINYAM TOYIB, 2012

Examensarbete / Institutionen för bygg- och miljöteknik,  
Chalmers tekniska högskola 2012:77

Department of Civil and Environmental Engineering  
Division of Structural Engineering  
Steel and Timber Structures  
Chalmers University of Technology  
SE-412 96 Göteborg  
Sweden  
Telephone: + 46 (0)31-772 1000

Cover:

FE model of a stress-laminated timber deck after initiation of slip showing deformations and contour plot of bending stresses, using a symmetry boundary condition at the mid-section. For more information, see Section 6.

Chalmers Reproservice / Department of Civil and Environmental Engineering  
Göteborg, Sweden 2012

Finite Element Modelling of Interlaminar Slip in Stress-Laminated Timber Decks  
Friction Interaction Modelling Using Abaqus

*Master of Science Thesis in the Master's Programme Structural Engineering and Building Performance Design*

JOAKIM CARLBERG

BINYAM TOYIB

Department of Civil and Environmental Engineering

Division of Structural Engineering

Steel and Timber Structures

Chalmers University of Technology

ABSTRACT

The stress-laminated timber (SLT) bridge deck is a common timber bridge structure and a satisfactory alternative to short-span bridges in terms of cost and performance. SLT decks consist of a series of timber or glulam beams side by side and compressed together using high-strength steel bars. The tensile forces introduced into the bars compress the laminations together so that the behaviour of the timber deck is similar to an orthotropic solid timber plate. A concentrated load is distributed from the loaded lamination onto the adjacent laminations due to the resisting friction between the stressed laminations. The aim of this thesis was to better understand the different responses observed in experimental tests and, with finite element models, study such details that would not be noticed in experimental tests, e.g. pre-stress distribution. The core process was to understand and express the frictional behaviour between laminations when subjected to high load levels using the commercial finite element software Abaqus. The modelling was based on linear elastic material but includes contact with friction between laminations. The results showed that the finite element model gives reliable results and capture the non-linear behaviour of the SLT deck before failure. The drawn conclusions can be used for further parameter studies and predictions of the ultimate capacity of such structures.

Key words: Stress-laminated timber deck, timber bridges, interlaminar slip, contact modelling, friction modelling, Abaqus

Finit-elementmodellering av interlaminär glidning i tvärspända träplattor  
Modellering av friktion i Abaqus  
Examensarbete inom Structural Engineering and Building Performance Design  
JOAKIM CARLBERG  
BINYAM TOYIB  
Institutionen för bygg- och miljöteknik  
Avdelningen för konstruktionsteknik  
Stål- och träbyggnad  
Chalmers tekniska högskola

## SAMMANFATTNING

Tvärspända träbroplattor är en vanlig brokonstruktionstyp och ett fullgott alternativ för broar med kortare spann vad gäller kostnad och prestanda. De tvärspända träplattorna består av en serie limträbalkar som är placerade sida vid sida och sammanpressade med hjälp av tvärgående höghållfasta stålstag. Dragkrafterna som introduceras i stålstagen pressar samman balkarna så att plattan uppträder som en solid, ortotropisk träplatta. En koncentrerad kraft förs från den lastade balken till intilliggande balkar genom friktionsspänningar mellan de sammanpressade balkarna. Syftet med denna avhandling var att bättre förstå de olika parametrar som observerats i experiment och med finita elementmodeller studera sådana detaljer som inte skulle märkas i experimentella tester, t.ex. förspänningsfördelning. Kärnprocessen var att förstå och uttrycka friktionsbeteendet mellan balkarna när de utsätts för stora laster med hjälp av den kommersiella programvaran Abaqus i vilken analyser av finita elementmodeller utförts. Modelleringen baserades på linjärelastiska material men inkluderar kontakt med friktion mellan balkarna. Resultaten visade att modellen ger tillförlitliga resultat och fångar det olinjära beteende som tvärspända träbroplattor uppvisar. Slutsatser från dessa undersökningar kan vidare användas för fortsatta parameterstudier samt bidra till att förutsäga brottgränsen av denna typ av strukturer.

Nyckelord: Tvärspända träplattor, träbroplattor, träbroar, interlaminär glidning, glidbrott, kontaktmodellering, friktionsmodellering, Abaqus

# Contents

1	INTRODUCTION	1
1.1	Background	1
1.2	Aim and scope	1
1.3	Method	2
1.4	Limitations	2
1.5	Outline	2
2	STRESS-LAMINATED TIMBER BRIDGE DECKS	3
2.1	Historical background	3
2.2	Pre-stressing in SLT decks	3
2.3	Butt joints	5
2.4	Friction	7
2.4.1	Coulomb friction	7
2.4.2	Static and kinetic friction	8
2.5	Glue-laminated timber	9
2.5.1	Coefficient of friction	10
3	FE MODELLING	11
3.1	Background	11
3.2	Element type	11
3.2.1	Reduced integration	12
3.3	Material properties	12
3.4	Load application	13
3.5	Non-linear FE modelling	13
3.5.1	Definition	13
3.5.2	Contact	13
3.5.2.1	Penalty friction	14
3.5.2.2	Static kinetic exponential decay	15
3.5.2.3	Lagrange multiple formulation	17
3.5.2.4	Rough friction	17
3.5.2.5	User-defined friction	17
3.5.3	Incremental loading	17
3.5.3.1	Time step	17
3.5.3.2	Iteration method	18

3.5.3.3	Convergence and tolerances	18
4	MODEL 1 - BOX ON A PLANE	20
4.1	Description	20
4.2	Material properties	21
4.3	Time step	22
4.4	Interaction	24
4.5	Load application	25
4.6	Mesh	28
4.7	Contact pressure	30
5	MODEL 2 – SIMPLIFIED SLT DECK	33
5.1	Background	33
5.2	Model with one beam	34
5.2.1	Material properties	34
5.2.2	Boundary conditions and load application	34
5.2.3	Element mesh	35
5.2.4	Results	37
5.3	Model with three beams	40
5.3.1	Material properties	41
5.3.2	Boundary conditions and load application	41
5.3.3	Type of pre-stressing	41
5.3.4	Influence of pre-stress level	46
5.3.4.1	Beam deflection	46
5.3.4.2	Longitudinal bending stress	49
5.3.4.3	Vertical shear stress between beams	50
5.3.4.4	Horizontal shear stress between beams	51
5.3.4.5	Reaction force	52
5.3.5	Elastic slip	57
5.3.5.1	Beam deflection	57
5.3.5.2	Longitudinal bending stress	57
5.3.5.3	Vertical shear stress between beams	58
5.3.5.4	Reaction force	59
5.3.6	Modulus of elasticity in longitudinal direction	59
5.3.6.1	Beam deflection	60
5.3.6.2	Longitudinal bending stress	61

5.3.6.3	Vertical shear stress between beams	62
5.3.6.4	Horizontal shear stress between beams	67
5.3.6.5	Reaction force	67
6	MODEL 3 – FULL-SCALE SLT DECK	69
6.1	Material properties	69
6.2	Boundary condition and load application	70
6.3	Mesh	71
6.4	Results	71
7	DISCUSSION	77
7.1	Box on a plane	77
7.2	Model with three beams	77
7.3	Full-scale model	78
8	CONCLUSION	80
8.1	General conclusions	80
8.2	Suggestions for further research	80
9	REFERENCES	81
	APPENDIX - SIMPLIFIED PRE-STRESS MODEL	83



## Preface

In this thesis, studies of how to model frictional behaviour between laminations in a stress-laminated timber deck using the finite element software Abaqus were performed. This was done by first studying a very simple model in order to learn the basic particularities of contact modelling. The acquired knowledge from this study was then applied on a series of studies of simplified stress-laminated timber bridge decks.

The thesis was carried out from January 2012 to June 2012. The work is a part of the research project “Competitive bridges”, and it was carried out at the Division of Structural Engineering, Steel and Timber Structures, Chalmers University of Technology. The research project is financed as a part of VINNOVA’s trade research programme with the two timber bridge manufactures, Moelven Töreboda AB and Martinsons Träbroar AB as the main financiers. The project was carried out with PhD-student Kristoffer Ekholm at Chalmers and Dr. Morgan Johansson at Reinertsen Sverige AB as supervisors and Professor Robert Kliger as examiner.

We would like to express our sincere gratitude and appreciation to our supervisors Kristoffer Ekholm and Morgan Johansson for their advice and tireless support throughout the whole course of this project.

Special thanks are also directed to our opponent group Karl Engdahl and Kresnadya Rousstia for their feedback and cooperation and to our families for their support and patience.

Göteborg, June 2012

Joakim Carlberg  
Binyam Toyib

### **Roman upper-case letters**

$A$	Cross-sectional area
$C$	Centre to centre spacing of pre-stressing plates
$C_B$	Butt joint factor
$E$	Modulus of elasticity
$E_L$	Modulus of elasticity in the longitudinal direction
$F$	Concentrated force
$F_{crit}$	Critical friction force
$F_f$	Friction force
$F_K$	Kinetic friction force
$F_S$	Static friction force
$F_{PS}$	Pre-stressing force
$G$	Shear modulus
$I$	Moment of inertia
$L$	Length
$M$	Bending moment
$N$	Normal force
$V$	Shear force
$W$	Bending resistance

### **Roman lower-case letters**

$l$	Length of the beam
$p$	Normal pressure
$p_l$	Locally applied pre-stress pressure
$p_u$	Uniformly applied pre-stress pressure
$u_z$	Vertical deflection
$x$	Distance along length
$y$	Distance along width
$z$	Distance along height

### **Greek letters**

$\mu$	Coefficient of friction
$\mu_k$	Coefficient of kinetic friction
$\mu_s$	Coefficient of static friction
$\gamma$	Slip rate
$\tau$	Shear stress
$\sigma_{11}$	Bending stress
$\sigma_{22}$	Vertical stress
$\nu$	Poisson's ratio



# 1 Introduction

## 1.1 Background

Stress-laminated timber (SLT) bridge decks consist of a series of timber or glulam beams, or laminations, side by side and compressed together using high-strength steel bars, see Figure 1.1. The tensile force introduced into the bars compresses the laminations together so that the behaviour of the timber deck is similar to an orthotropic solid timber plate providing load carrying capacity for bending moment and shear forces in all direction. The friction between the laminations is mainly dependent on the pre-stress level, surface roughness and moisture content. The friction behaviour between the lamination surfaces affects the load bearing capacity of such bridges.

The current design approach for stress-laminated timber bridge decks assumes that the behaviour is linear during both serviceability and ultimate load states. However, experimental tests have showed that the behaviour, due to slip between laminations, is non-linear before reaching ultimate load. This phenomenon mainly occurs when the pre-stress force is low and heavy load acts locally. The slip between the surfaces creates stress redistribution and irreversible deformation after the deck has been unloaded. Therefore, understanding this behaviour can lead to a safer and more economical design approach for timber bridges in the ultimate limit state.

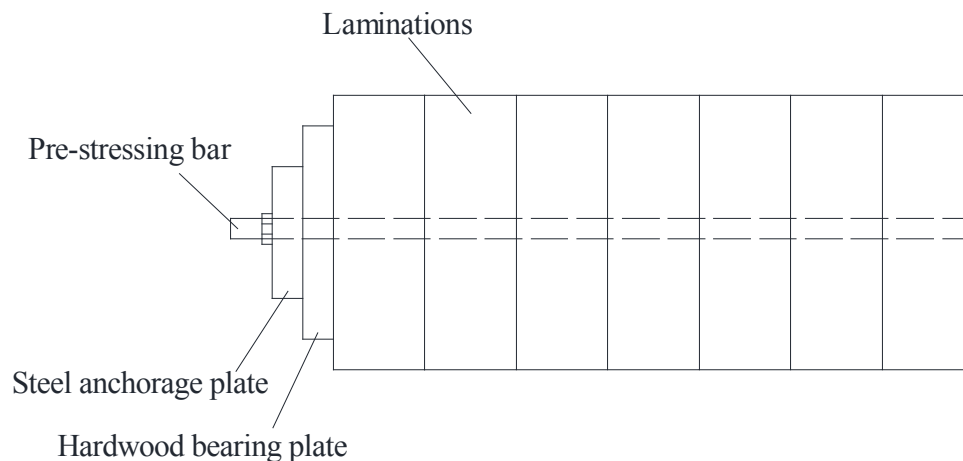


Figure 1.1 Stress-laminated timber deck cross section normally used in Sweden.

## 1.2 Aim and scope

The main aim of the thesis is to model the non-linear behaviour of SLT bridge decks using the commercial finite element program Abaqus and study what importance different parameters have on the final behaviour. This is to better understand the different responses observed in experimental tests and, using finite element models, study such details that would not be noticed in experimental tests, e.g. the distribution of pre-stress in the deck. The core process will be to understand and express the frictional behaviour between laminations when loaded until failure. This can further be used for parameter studies and prediction of the ultimate capacity of such structures.

## 1.3 Method

A literature study was carried out to get general information concerning stress-laminated timber decks. The finite element modelling started from very simplified cases to more advanced models which consider different parameters in order to capture the real behaviour of SLT decks. Experiments related to these studies have been performed at Chalmers, Ekholm (2012), and experimental results were used for comparison with the numerical analyses made in Abaqus using the procedure from a previous master's thesis by Hellgren and Lundberg (2011).

## 1.4 Limitations

Stress-laminated timber bridges are dependent on the pre-stress force applied from the steel bars. However, this stress is not constant throughout the service life of the deck due to stress relaxation in the steel bars and creep in the timber. These long-term effects are not included in the full-scale model.

The actual loading condition of SLT bridge decks is that they are exposed to moving loads and cyclic load actions on the deck. However, the tests and the finite element model are exposed to static loads at specific load positions.

## 1.5 Outline

The outline of this thesis describes the layout and content of the project. A literature review was made before a series of studies were conducted. Discussion and conclusion were made based on the observations of different models.

*Chapter 2* presents a literature study including a brief history of SLT bridge decks. Different parameters involved in SLT bridge decks are discussed.

*Chapter 3* provides a brief discussion of finite element modelling. Different frictional models that exist in Abaqus are discussed.

*Chapter 4* covers a simplified finite element model of friction. This model is used to better understand how contact and friction is modelled with finite elements in Abaqus.

*Chapter 5* presents simplified models of SLT bridge decks. These models were used to understand how different parameters influence the behaviour of SLT bridge decks.

*Chapter 6* contains a full-scale model with the same dimension and material properties as experimental tests that have been performed at Chalmers by Ekholm (2012). Comparisons of finite element results with experimental test results are presented.

*Chapter 7* presents the discussion of various observations of the different analyses performed in previous chapters.

*Chapter 8* provides conclusions that can be drawn from this project. Suggestions for further research are also presented.

## 2 Stress-laminated timber bridge decks

### 2.1 Historical background

In the mid-1970s, the technique of compressing a deteriorated nail-laminated timber bridge was developed as a method to rehabilitate the bridge temporarily before replacing it completely. This was done by adding steel bars above and below the deck to then tension them in order for the deck to be compressed, see Figure 2.1. The resulting effect was so impressive that the scheduled replacement of the bridge was cancelled. Naturally, interest arose in using the technique for construction of new bridges. The first design codes for such structures were included in the Ontario Highway Bridge Design Code in 1979, Ritter (1990).

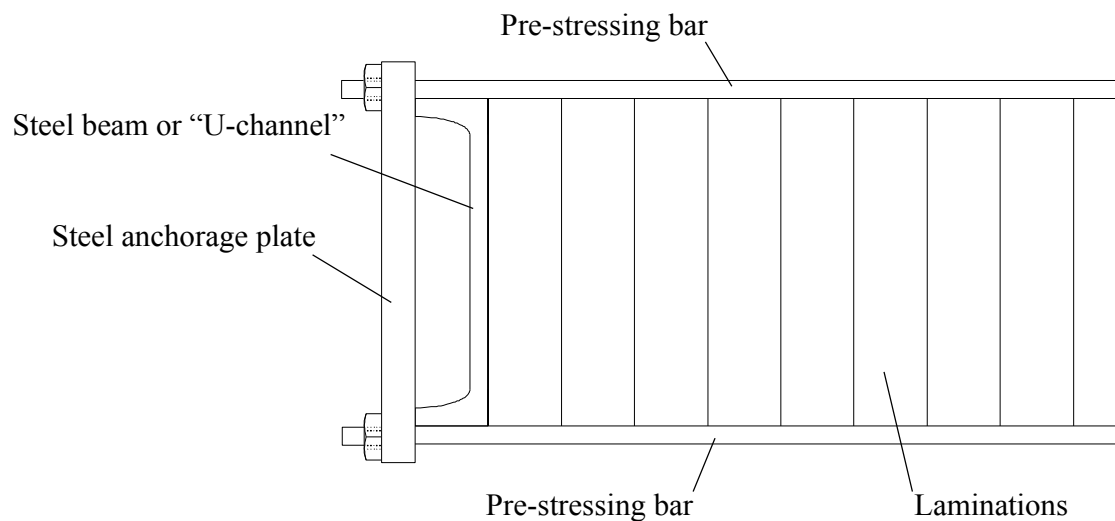


Figure 2.1 Anchorage configuration with steel bars above and below deck according to Ritter (1990).

The SLT technique spread outside from Canada in the mid-1980s and during the second half of the decade numerous bridges were built in USA. During the 1990s a joint investment was conducted by the Nordic countries for the development of timber bridge construction and the introduction of SLT bridge decks. This created a revival for timber bridges in the Nordic countries and since 1994 design criteria for SLT bridge decks are included in the Swedish road authorities design codes.

### 2.2 Pre-stressing in SLT decks

The load transfer in SLT decks is developed by the applied compression of pre-stressing and friction between laminations. The pre-stress is introduced in the high strength steel bars positioned through pre-drilled holes in the deck. The holes in the deck are generally made twice the size of the pre-stressing bars to avoid any "dowel" action. The main advantage of pre-stressing is to better distribute the concentrated loads from the wheels by squeezing the laminations together, attaining the behaviour of an orthotropic slab.

There are failure modes that must be prevented by the pre-stressing. The first failure mode is the development of gap between laminations due to transversal bending moment, see Figure 2.2. This gap between two laminations in the deck reduces the interlaminar contact and also creates a risk for moisture and debris penetration into the deck. Such a gap can be accepted in ultimate limit state, though. The second failure mode is the vertical interlaminar slip due to transversal shear stress, see Figure 2.3. Horizontal interlaminar slip is another mode of distortion that may occur at low load levels creating non-linear behaviour in the decks, however, it is normally not considered as a failure mode in the literature.

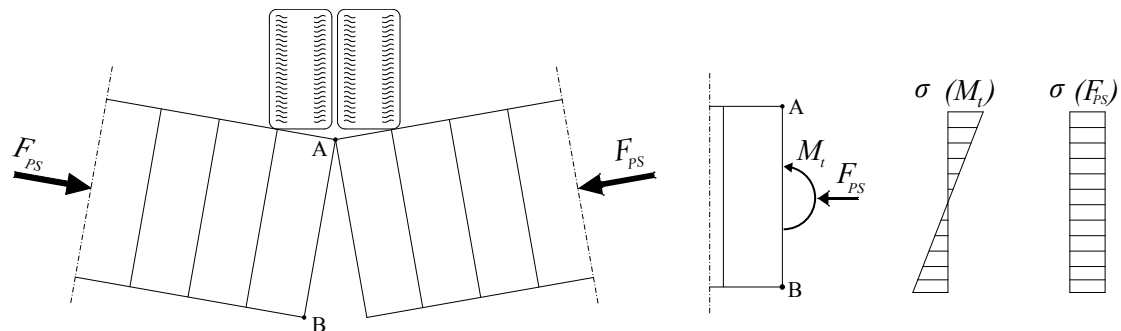


Figure 2.2 Gaps forming due to bending moment. To the right, the stresses due to moment,  $M_t$ , and pre-stressing force,  $F_{PS}$ .

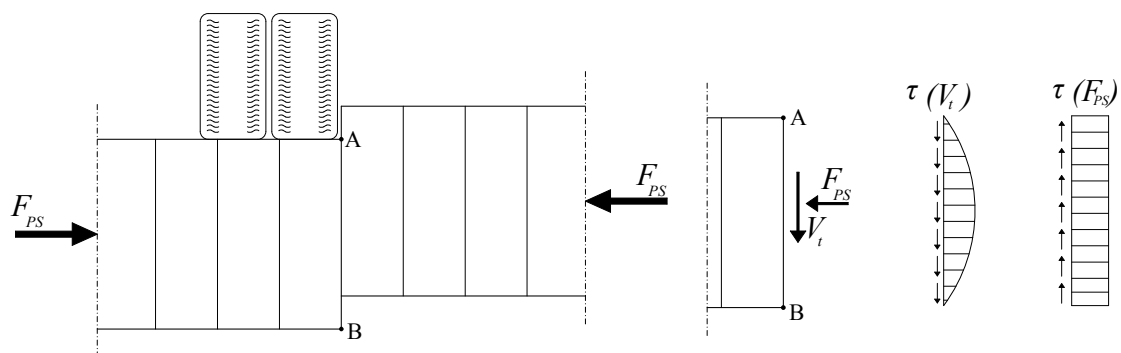


Figure 2.3 Interlaminar slip between laminations due to transversal shear force. To the right, the stresses due to shear,  $V_t$ , and pre-stressing force,  $F_{PS}$ .

The pre-stressing force can be reduced due to creep in the wood. Creep is the slow change in the dimensions of a material due to prolonged, constant stress. Even though the term creep is used, the long-term stress in the wood is not constant in time due to factors like stress relaxation in the steel bars and temperature variation. Taylor *et al.* (1983) carried out a series of laboratory tests to investigate the loss of pre-stress due to wood creep. The effects of wood species, stiffness ratio, tensioning sequence, and relative humidity were examined. The test results showed that the stress ratio between the final stress level and initial stress level did not fall below 50 %. Oliva and Dimakis (1989) reported a loss of 60 % and stated the cause of the loss to drying and shrinkage of the wood. DiCarlantonio (1988) performed tests without the use of a distribution channel (U-channel of steel used to spread out the pre-stress) and

measured an average loss of pre-stress of 40 %. The crushing of the wood under the anchor plates, due to high concentrated forces, was the cause for some of the losses.

Temperature change also has an effect on the pre-stressing force. Since the coefficient of thermal expansion of the wood perpendicular to grain is greater than that of steel, a drop in temperature will result in a decrease of the pre-stress force and an increase in temperature will increase the pre-stress force. Seasonal temperature change is more significant than daily temperature fluctuations since daily temperature variation is small. If a bridge is constructed during the summer and creep losses occur shortly after jacking, additional temporary loss of pre-stress can occur in the winter due to temperature change, Sarisley *et al.* (1990).

Ritter, Wacker *et al.* (1995) made an observation on the effect of moisture content variation in the deck which has an influence on the pre-stressing force in the bars. Seasonal variation or local effect due to standing water on the deck can cause variation in moisture content of the deck. Local crushing of the lamination could occur if the swelling of the deck is significant.

According to Eurocode 5.2, EN 1995-2 (2004), the long-term pre-stress between the laminations should not fall below 350 kPa throughout the service life of the deck. Eurocode 5.2 also states that the long-term pre-stress can be assumed to be greater than 350 kPa, as long as the initial pre-stress is greater than 1000 kPa, the moisture content at the point of assembly is less than 16 % and the deck is protected from large moisture variation.

In order to get proper performance of the SLT deck, sufficient level of uniform, compressive pre-stressing must be maintained. To maintain the minimum pre-stress level, the following sequence is recommended:

1. The deck is initially assembled and stressed to the design level required for the structure.
2. The deck is re-stressed to the full level approximately 1 week after the initial stress.
3. Final stress is completed 4 to 6 weeks after the second stressing.

With this stressing sequence the maximum expected loss due to creep will be reduced. In addition to this, it is also necessary to regularly check the pre-stress levels over the life of the structure as part of the maintenance program. It will be necessary to re-stress if the pre-stress level is found to be less than the limit, Ritter (1990).

## 2.3 Butt joints

Butt joints can be considered as intentional imperfections as opposed to natural imperfections such as knots or grain deviation in laminations. Butt joints are used to join laminations to enable the stress-laminated timber decks to span longer than the maximum length of the individual laminations. Regular patterns of butt joints are used throughout stress-laminated timber decks such as the "one in four" butt joint pattern, which means the butt joints are repeated every fourth lamination along the transverse cross section of the deck, see Figure 2.4.

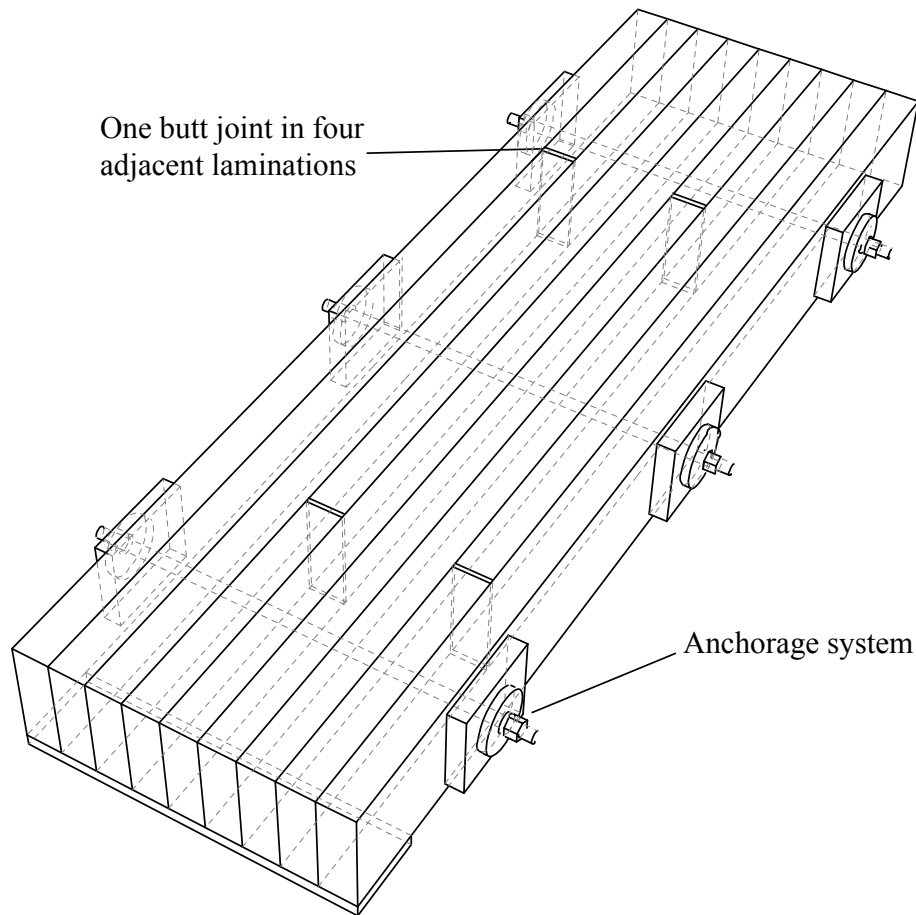


Figure 2.4 Butt joints in a stress-laminated timber deck with a 1 in 4 pattern.

Butt joints are not able to transfer any bending moment provided that two laminations are not in contact lengthwise. The load transfer takes place through the friction between the butt-jointed lamination and the adjacent laminations. The full flexural capacity of the butt-jointed lamination is reached at a certain distance from the butt joints and this distance is called “development length”.

For regular and repeating butt joint patterns, one complete pattern can be used as representative of the deck to establish the bending stiffness of the wood assembly. Simple beam theory can be used to model the response of a representative deck section, assuming that one wheel line load of the design vehicle is distributed over a wheel load distribution width,  $D_w$ . Distribution width,  $D_w$ , is affected by butt joint frequency by means of reducing the longitudinal modulus of elasticity,  $E_L$ , using a factor  $C_B$ . Ritter (1990) provides a table of butt joint factors,  $C_B$ , for a frequency of butt joints appearing within a 1.22 m distance along the span of the deck, see Table 2.1.

Table 2.1 Butt joint factor,  $C_B$ , for stress-laminated timber bridge decks.

Butt joint frequency	$C_B$
1 in 4	0.80
1 in 5	0.85
1 in 6	0.88
1 in 7	0.90
1 in 8	0.93
1 in 9	0.93
1 in 10	0.94
No butt joints	1.00

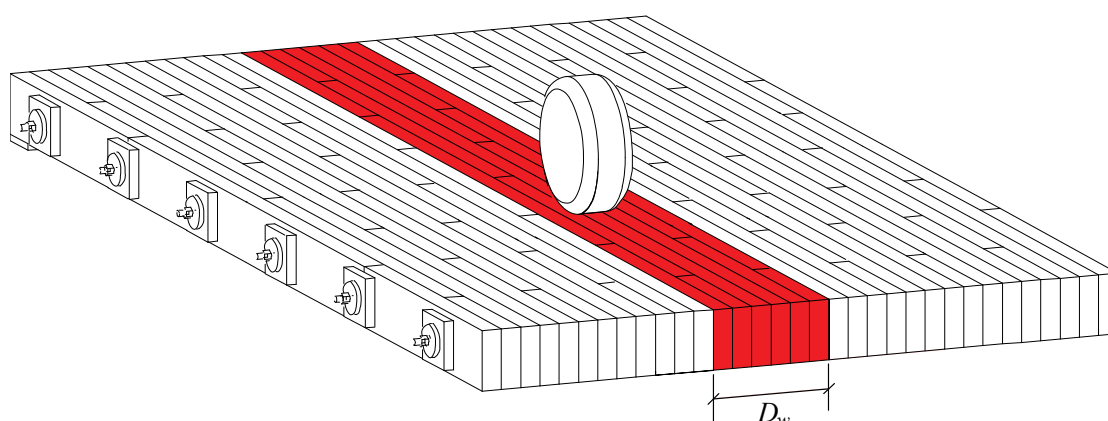


Figure 2.5 Part of a deck with wheel line load and equivalent beam width,  $D_w$ .

## 2.4 Friction

### 2.4.1 Coulomb friction

The Coulomb frictional model gives a first order approximation of friction by relating the maximum allowable frictional shear stress across the interface with the contact pressure between the contacting bodies. Before two contacting surfaces start sliding relative to one another, the surfaces can carry shear stress up to a certain magnitude across their interface; this state is known as sticking, see Figure 2.6. Based on Coulomb friction the critical friction stress,  $\tau_{crit}$ , at which sliding starts is given as a fraction of contact pressure,  $\sigma$ , see Equation 2.3. The fraction,  $\mu$ , is known as the coefficient of friction.

$$\tau_{crit} = \mu \cdot \sigma_p \quad (2.3)$$

Where:

$\tau_{crit}$  Critical friction stress

$\sigma_p$  Contact pressure

$\mu$  Coefficient of friction

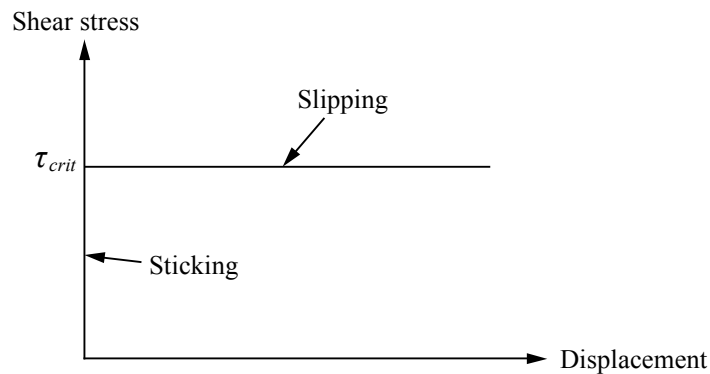


Figure 2.6 Ideal Coulomb friction model.

## 2.4.2 Static and kinetic friction

The friction force  $F_f$  between two or more bodies compressed together with the normal force  $N$  show the following property in a simple approximation.

Static friction is the force  $F_s$  required to move the body from its state of rest. This force is roughly approximated with the normal force  $N$ .

$$F_s = \mu_s \cdot N \quad (2.4)$$

Where:

$\mu_s$  Coefficient of static friction

Kinetic friction is the resisting force after the bodies start moving in relation to each other. Kinetic friction  $F_k$  is also proportional to the normal force  $N$ .

$$F_k = \mu_k \cdot N \quad (2.5)$$

Where:

$\mu_k$  Coefficient of kinetic friction

The coefficient of kinetic friction is usually less than the coefficient of static friction when the material is the same in both surfaces.

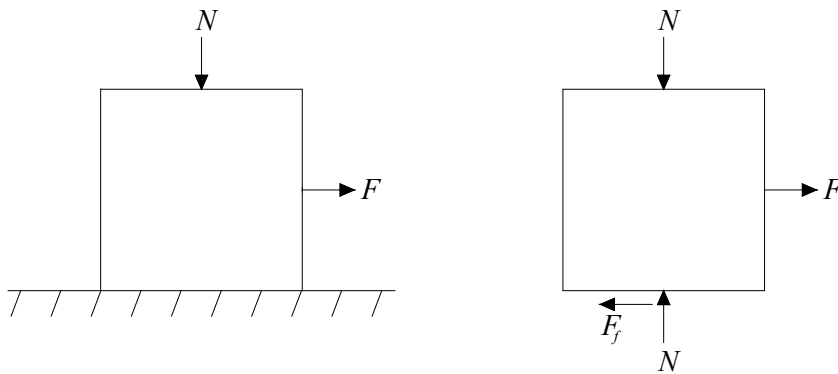


Figure 2.7 Box loaded by normal and tangential force in the plane and its corresponding free-body diagram.

## 2.5 Glue-laminated timber

Glue-laminated timber, also known as glulam, is composed of several layers bonded together with durable, moisture resistant adhesive. The lamellas are glued together with grain parallel to the length. The thickness of the lamellas is between 25 to 50 mm, FPL Wood Hand book (2010). In Sweden the minimum number of lamellas for it to be called glulam is four. Norway spruce is the most common timber used to manufacture glulam in Sweden.



Figure 2.8 Glulam beams with different widths.

Glulam beams can be made straight or curved which gives more flexibility for design. The glulam beam can be made from lamellas of equal strength in all layers or lamellas with different strength. In combined glulam they are arranged in a way so that lamellas with higher strength are put in the top and the bottom of the beam where the bending stresses are higher.

### **2.5.1 Coefficient of friction**

The coefficient of friction of timber including the glulam beam is affected by different factors. Some of the main factors affecting the coefficient of friction in timber are fibre direction, surface roughness and moisture content.

The transversal and longitudinal friction coefficient are the main components in stress laminated timber bridge decks as the resistance is developed by the interaction of the glulam beams. Due to the interlocking between the fibres when two wood surfaces interact with each other the friction coefficient is higher in the transverse direction than in the longitudinal fibre direction, Kalbitzer (1999).

The surface roughness is dependent on whether the wood is sawn or planed where sawn wood often has a higher coefficient of friction than planed wood due to higher surface roughness, Kalbitzer (1999). In the experimental tests by Ekholm (2012), planed glulam beams made of spruce were used.

Moisture content is another factor that influences the coefficient of friction of the glulam beams. An increase in moisture content of the beams from oven dry to fibre saturation, which typically is around 30%, increases the coefficient of friction. The friction coefficient is more constant when the moisture content is increased further.

## 3 FE modelling

### 3.1 Background

Conventionally stress-laminated timber bridge decks are analysed using linear elastic modelling with shell elements. This approach generates some results that do not correlate well with results observed in experiments, e.g. underestimated deflections and stresses as well as high torsional moments which do not appear in reality due to stress redistribution, slipping and opening between the laminations, Ekholm *et al.* (2011).

The modelling in this thesis was instead based on linear elastic material but included the interaction between laminations in order to capture and study the non-linear phenomena caused by interlaminar slip and opening.

### 3.2 Element type

Different element types are used in finite element modelling to perform the analyses. Some of the element types are continuum (solid) elements, shell elements, beam element and truss element. Based on what type of analysis is going to be done, different types of solid elements can be used in finite element models. In this thesis 2D and 3D solid elements were used. For modelling the 2D box on a plane, as seen in Section 4, a 4-node bilinear plane stress quadrilateral, reduced integration, hourglass control, i.e. CPS4R, was used in Abaqus. The glulam beams for the other models were modelled using a 3D solid element type, specifically the 8-node linear brick with reduced integration and hourglass control, titled C3D8R, see Figure 3.1. It is a first order element with linear interpolation in each direction and it shows good convergence for contact analysis, Hellgren and Lundberg (2011). The 20-node brick element (C3D20) is generally superior for stress analysis but is not as suitable for contact problems. The results from the eight-node element are adequate as long as the mesh is fine enough, Ekholm *et al.* (2011).

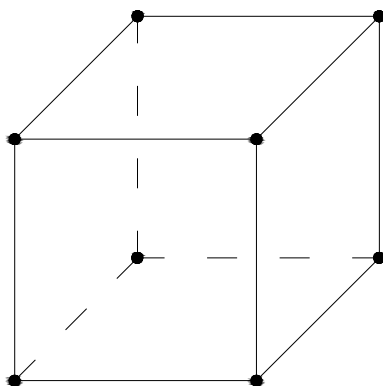


Figure 3.1 8-node linear brick element, C3D8R.

### 3.2.1 Reduced integration

Reduced integration is an optimized method used to decrease the amount of necessary calculations and subsequently reduce the needs for data storage and CPU time. This method can be applied to quadrilateral and hexahedral elements and its minimum amount of integration points are sufficient to integrate precisely the contributions of the strain field that are one order less than the order of interpolation. The integration point is placed at the location which provides the highest accuracy within the element; the so-called Barlow points, Barlow (1976).

A disadvantage with the reduced integration procedure is the possible occurrence of deformation modes which does not cause any strain at the integration points. This zero-energy deformation mode is sometimes referred to as “hourglassing” because of the resulting geometry of the elements when the deformation propagates through the mesh. It will also cause inaccurate solutions, as can be seen in Section 4.5. Abaqus has a way of preventing this behaviour by adding an additional artificial stiffness to the element, Abaqus (2010).

On the other hand reduced integration may also be required in order to obtain correct stiffness in bending.

### 3.3 Material properties

The material of the glulam beams in the SLT deck was modelled with a linear anisotropic linear elastic material type. The different elastic and shear moduli for different directions were specified in the mechanical elastic part by choosing the “engineering constants” option in Abaqus. The material properties of the glulam were taken from Eurocode 5.2, EN 1995-2 (2004). The material orientation was based on the material properties of glulam in different directions, see *Figure 3.2*.

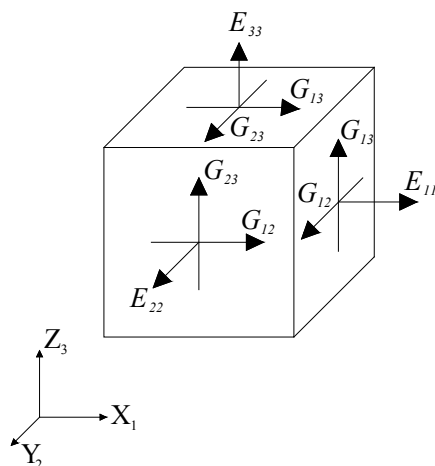


*Figure 3.2 Orientation of material properties*

According to Eurocode 5.2, the relations between modulus of elasticity in different directions are given as:  $E_{11}=E_L$ ,  $E_2=E_3=0.02 \cdot E_{11}$ ,  $G_{12}=G_{13}=0.06 \cdot E_{11}$ ,  $G_{23}=0.1 \cdot G_{12}$ .

Where  $E_L$  is the modulus of elasticity in longitudinal direction.

### 3.4 Load application

The load can be applied in different ways. One method is to put the load as pressure or forces on the structure to get the displacement and stresses. This method is called load-controlled load application. But on the other hand it is also possible to prescribe a displacement to the structure and get the force or pressure needed to cause the specified displacement. This method is called displacement-controlled load application. Displacement-controlled load application is important in modelling non-linear behaviour of the structure and helps to capture the behaviour after the ultimate load is reached, see Figure 3.3.

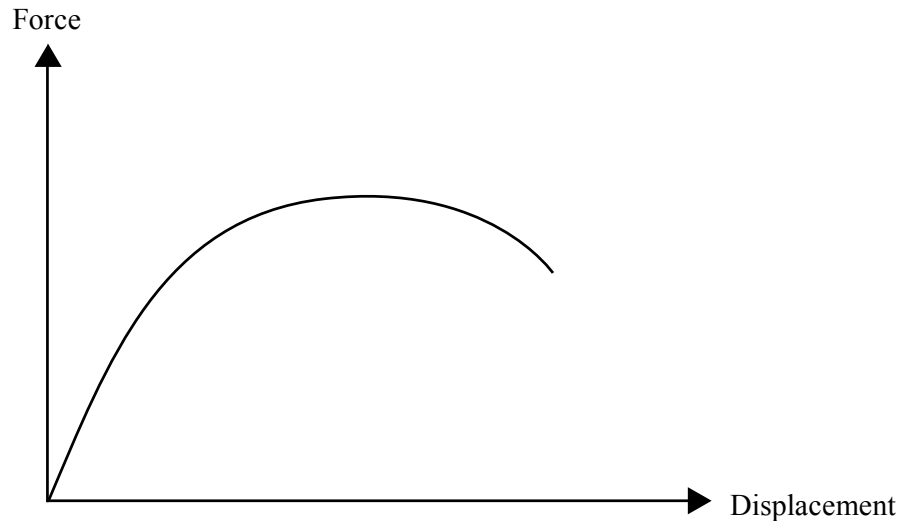


Figure 3.3 Non-linear force-displacement relationship.

### 3.5 Non-linear FE modelling

#### 3.5.1 Definition

Non-linear finite element modelling is performed by introducing non-linear material properties, non-linear geometry and/or non-linear boundaries, Abaqus (2010). It gives a better result when the model is loaded above its elastic limit and where the expected deformation is high. In this thesis non-linear finite element modelling was performed by introducing the non-linear geometry in order to include the second order effect, by activating the NLGEOM feature in Abaqus. Non-linear boundaries were modelled by assigning an elastic-ideally plastic frictional formulation for contact analyses as described in Section 3.5.2.1.

#### 3.5.2 Contact

In finite element analysis, contact calculation involves pairs of surfaces that may come into contact during the analysis. One of the surfaces must be assigned the master surface and the other surface must be assigned the slave surface. The slave node is constrained not to penetrate the master surface. However the master node can penetrate the slave surface, Abaqus (2010).

There are several parameters that control the behaviour of two contacting surfaces. One parameter is the contact formulation 'finite sliding' or 'small sliding' that specifies the expected relative tangential displacement of the two surfaces. Finite sliding is the most general, but it is computationally more demanding. Small sliding

should be used if the relative tangential displacement is likely to be less than the distance between two adjacent nodes. In this thesis finite sliding was used to control the behaviour of two contacting surfaces. Another parameter that can be specified is the relation between the contact pressure and separation between the contacting surfaces. In this thesis hard contact was chosen which means the interface cannot withstand any tension, Abaqus (2010).

There are different frictional formulations in Abaqus depending on the level of the model to capture the real frictional behaviour. The basic Coulomb friction model is used as a base for the different frictional models. These frictional formulations are:

- Penalty friction
- Static kinetic exponential decay
- Lagrange multiplier
- Rough friction
- User-defined friction

These methods are briefly described in Sections 3.5.2.1-3.5.2.5. For all models studied in this thesis, penalty friction formulation has been used to model a modified Coulomb friction by introducing the elastic slip in the sticking phase.

### 3.5.2.1 Penalty friction

Penalty friction formulation includes a stiffness that allows some relative motion, i.e. elastic slip, of the actual surfaces when they are in the sticking phase. Elastic slip affects the frictional behaviour before the slipping phase occurs. Elastic slip is an elastic displacement during the sticking phase, see Figure 3.4.

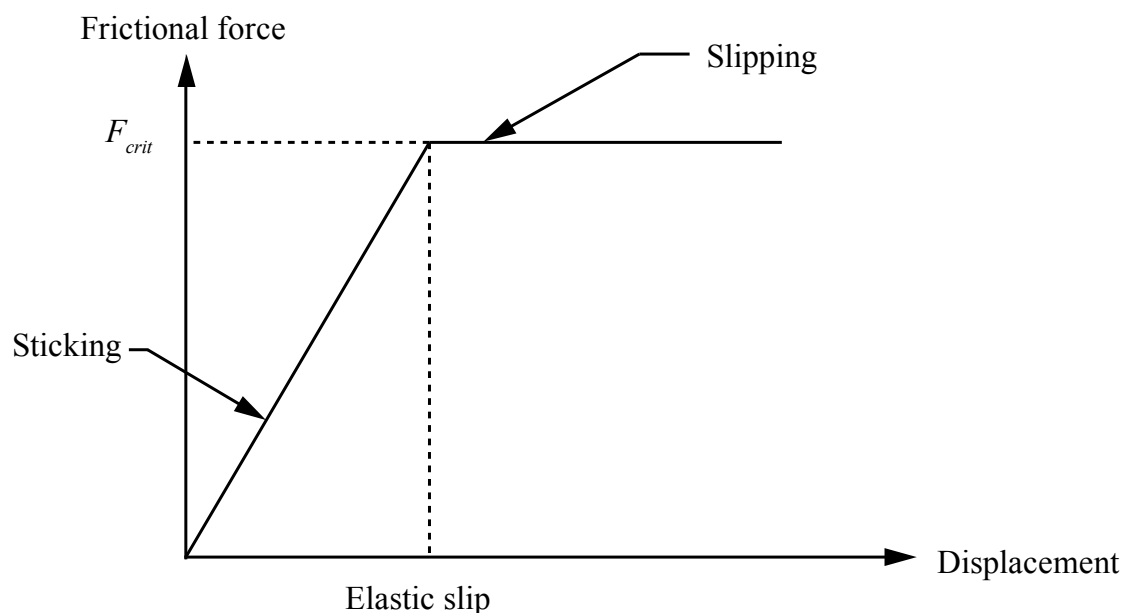


Figure 3.4 *A general friction curve with penalty formulation according to Abaqus (2010).*

In reality the elastic slip is assumed to correspond to the elastic displacement in the surface roughness. To find the correct elastic slip value for the analysis is difficult. However, the elastic slip value can be adjusted to real material parameters to capture the real behaviour of the slip.

In Abaqus the elastic slip can be specified either as a fraction of the element length or as an absolute distance. By default the elastic slip is defined as 0.5% of the average length of all contact surface elements in the model. However, when using the absolute distance the elastic slip is independent of the element size. In this thesis absolute distance was used to specify the elastic slip.

Isotropic frictional property is used by default in Abaqus when using penalty frictional formulation. However, it is also possible to use anisotropic friction by putting two different friction coefficients, where  $\mu_1$  is the coefficient of friction in the first slip direction and  $\mu_2$  is the coefficient of friction in the second slip direction. The critical friction force, for the two directions, forms an ellipse region with the two extreme points being  $F_1^{crit} = \mu_1 \cdot N$  and  $F_2^{crit} = \mu_2 \cdot N$ , see Figure 3.5. The size of this region depends on the contact force between the parts. The slip occurs in the normal direction to the critical shear stress surface, Abaqus (2010).

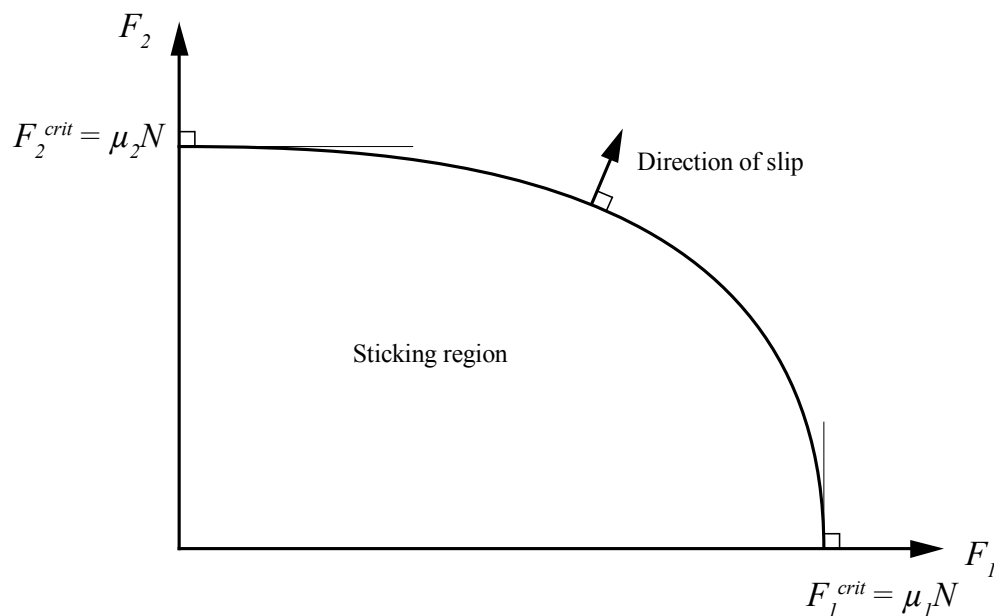


Figure 3.5 Critical shear force surface for anisotropic friction according to Abaqus (2010).

### 3.5.2.2 Static kinetic exponential decay

Static kinetic exponential decay formulation is an extension of the penalty friction formulation which also introduces elastic slip. In the default model the static friction coefficient corresponds to the value given at zero slip rate, and the kinetic friction coefficient corresponds to the value given at the highest slip rate. The transition between static and kinetic friction is defined by the values given at intermediate slip rate, see Figure 3.6. In this model the static and kinetic friction coefficients can be functions of contact pressure, temperature, and field variables, Abaqus (2010).

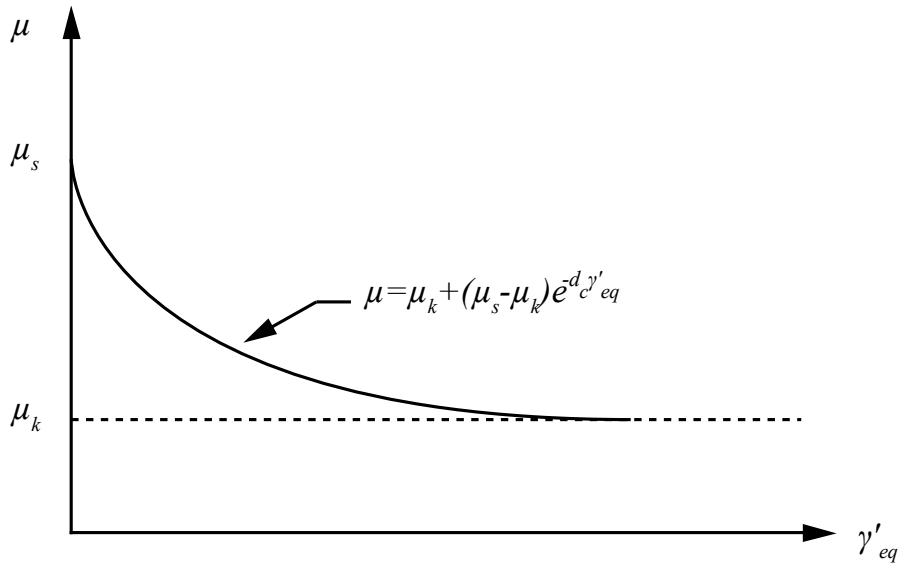


Figure 3.6 Static kinetic exponential decay formulation where  $d_c$  is the decay coefficient and  $\gamma'_{eq}$  is the equivalent slip rate according to Abaqus (2010).

Alternatively, it is also possible to provide test data points to fit the exponential model. At least two data points must be provided. The first point represents the static coefficient of friction specified when the slip rate is zero ( $\gamma'_1=0, \mu_1=\mu_s$ ) and the second point at a certain slip rate ( $\gamma'_2, \mu_2$ ) corresponds to an experimental measurement taken at a reference slip rate  $\gamma'_2$ . An additional data point can be specified to characterize the exponential decay for infinite slip rate. If this additional data point is omitted, Abaqus will automatically provide a third data point ( $\gamma'_\infty, \mu_\infty$ ), to model the assumed asymptotic value of the friction coefficient at infinite velocity, see Figure 3.7.

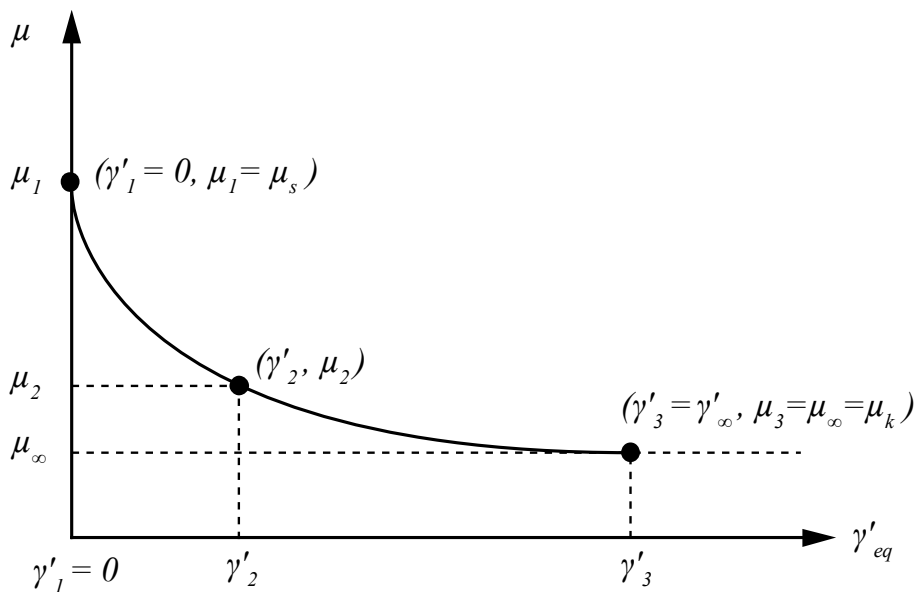


Figure 3.7 Test data formulation according to Abaqus theory manual (2010).

### 3.5.2.3 Lagrange multiple formulation

Lagrange multiple formulation sets the relative motion between two closed surfaces, elastic slip, to zero until  $F = F_{crit}$ . However, the Lagrange multipliers increase the computational cost and has convergence problem if points are iterating between sticking and slipping condition. Lagrange friction formulation should be used only in problems where the resolution of the sticking/ slip behaviour is of utmost importance, Abaqus (2010).

### 3.5.2.4 Rough friction

Rough friction formulation specifies an infinite coefficient of friction ( $\mu = \infty$ ) and prevent elastic slip. Once surfaces are closed and undergo rough friction, they should remain closed. If a closed contact interface with rough friction opens due to large shear stress, convergence difficulties may arise. Rough friction model is usually used in relation with the no-separation contact pressure-overclosure relationship for motion normal to the surface, which forbids separation of the surface once they are closed, Abaqus (2010).

### 3.5.2.5 User-defined friction

User-defined friction formulation gives a possibility to make friction dependent of slip rate, temperature and field variables. With this method it is possible to state a number of properties associated with friction model, Abaqus (2010).

## 3.5.3 Incremental loading

In a non-linear analysis, the solution may not converge if the load is applied in a single increment. If this is the case, the load must be applied gradually, in a series of smaller increments.

### 3.5.3.1 Time step

In finite element modelling the load is usually applied in a series of steps. Different load and boundary conditions can be defined in each step with linear increments from their value at the start of the step to their values at the end of the step by choosing the ramp option in Abaqus, see Figure 3.8. These increments are generally referred to as time steps in finite element modelling. In Abaqus they are however called increments and are subordinate to what is called time steps in Abaqus. The time steps in Abaqus are in other words only containers for the increments. Many finite element codes will automatically reduce the time step if the solution fails to converge, Bower (2008).

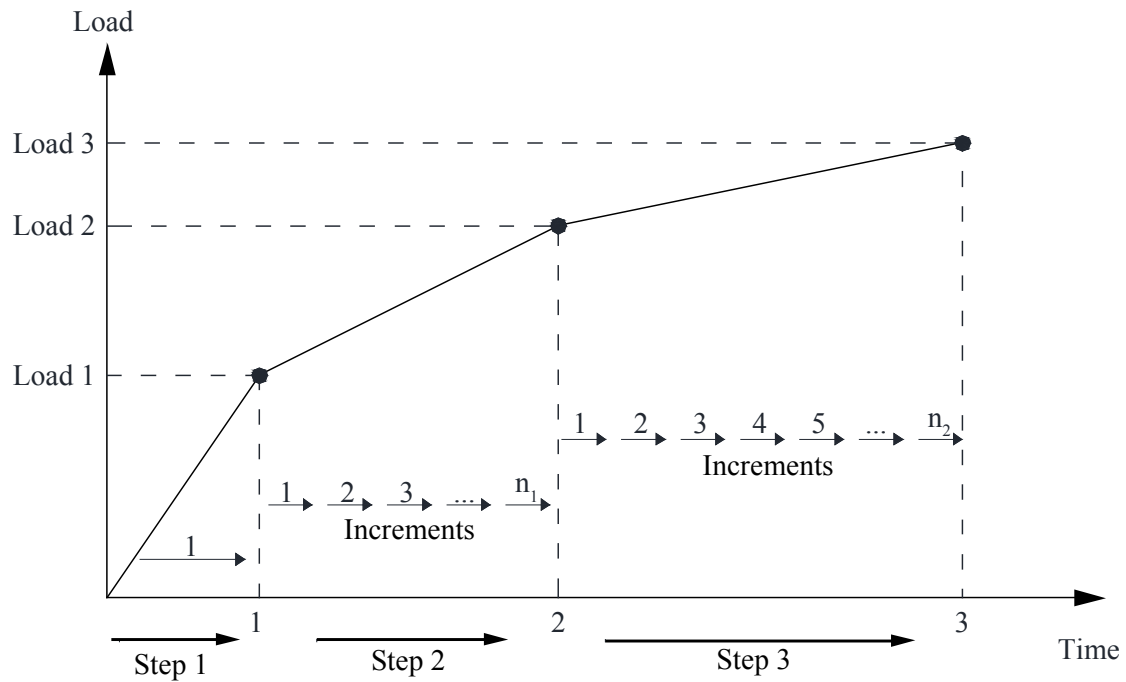


Figure 3.8 Schematic view of how steps and increments can be distributed, according to Bower (2008).

### 3.5.3.2 Iteration method

For each time step increment there can be several iterations. Iteration is an attempt to find equilibrium for that specific increment. The number of iterations depends on when equilibrium is reached. Sometimes the equilibrium condition cannot be fulfilled and the iteration diverge, Abaqus (2010).

There are three different iteration methods to solve equilibrium equation in Abaqus. Those are Full Newton, Quasi Newton (BFGS) and Contact iteration. The analyses in this thesis were made using the Full Newton iteration method.

### 3.5.3.3 Convergence and tolerances

Abaqus uses several criteria to decide whether a solution has converged for a particular iteration or not. Contact problems introduce even more criteria which need to be checked for convergence, the severe discontinuity iteration (SDI) loop as seen in Figure 3.9.



## 4 Model 1 - Box on a plane

### 4.1 Description

To better understand how contact and friction is modelled with finite elements in Abaqus, several simplified models were studied. The first one was the box on a plane, which was a continuation of the study made by Hellgren and Lundberg (2011). This simple model is helpful to understand the basics of contact modelling.

For the majority of the studies the two-dimensional model consists of a box on a plane where the plane is modelled as an elastic plate, see Figure 4.1 (a). Solid 2D elements were used in Abaqus to model the elastic parts. Analyses of rigid bodies were also made where one of the bodies was modelled as a rigid wire element. Different parameters were checked to compare results related to the frictional behaviour. The results from these analyses were used as background for modelling of the full-scale test and to describe and better understand the real behaviour.

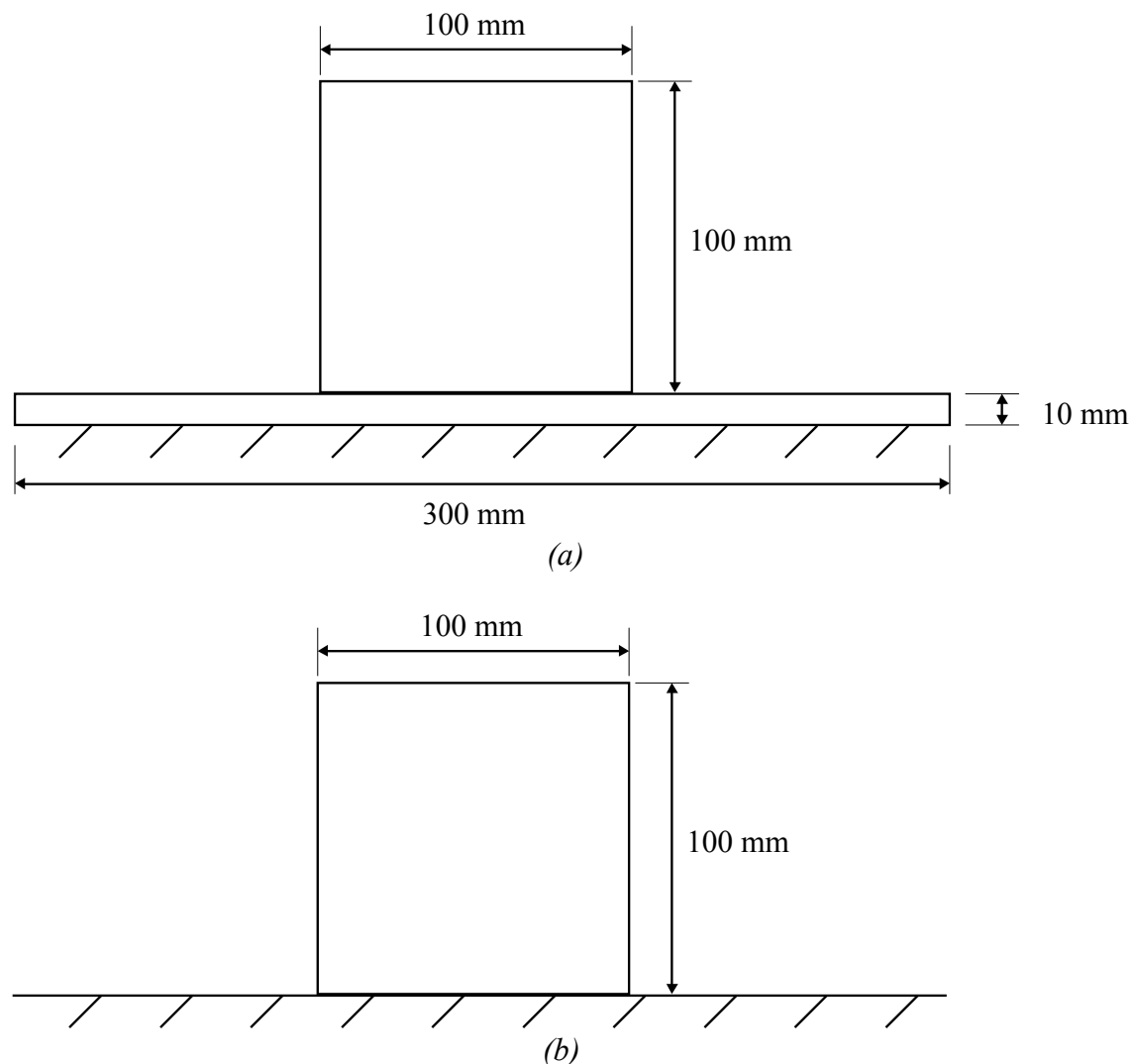


Figure 4.1 a) Elastic box on elastic plate b) Elastic box on rigid surface

The box on a plane model represents the slip between the glulam beams in a stress-laminated timber deck when subjected to load. A contact property was assigned to the contact surfaces and represents the frictional behaviour between the glulam beams. To simulate the pre-stress of a stress-laminated timber deck a pressure was applied on the top surface of the box. The box was prescribed to a displacement which is larger than the elastic slip. In this way both the elastic and non-elastic states were obtained.

## 4.2 Material properties

The box was assigned a material property similar to that of a glulam beam by setting its modulus of elasticity to 12 GPa. In order to simplify the analysis the Poisson ratio,  $\nu$ , was set to zero and isotropic material properties was used so that the modulus of elasticity was equal in all directions.

Frictional shear stress distributions for different modulus of elasticity ratios, as seen in Table 4.1, were investigated to find a good correlation with the analytical distribution. Displacement-controlled load application method was used to capture the behaviour before and after the box starts slipping. A uniform displacement was prescribed for all nodes along the height of the box on both surfaces. However, this method of load application creates an uneven load distribution along the height that lead to the development of moment on the box which is described further in Section 4.5. The developed moment in combination with the vertical applied pressure creates an inclined contact pressure which leads to inclined shear stress distribution, see Figure 4.2. The peak values observed at the edge of the contacting surfaces is related to the contact pressure as discussed in Section 4.7. The peak values are reduced when the elastic ratio,  $\alpha$ , increases.

*Table 4.1 Data used for comparison of elastic moduli between box and plate.*

Modulus of elasticity, $E$ [GPa]		Ratio, $\alpha$ [-]
Box	Plate	$E_{Plate}/E_{box}$
12	1.2	0.1
12	12	1
12	120	10
12	$\infty$	$\infty$

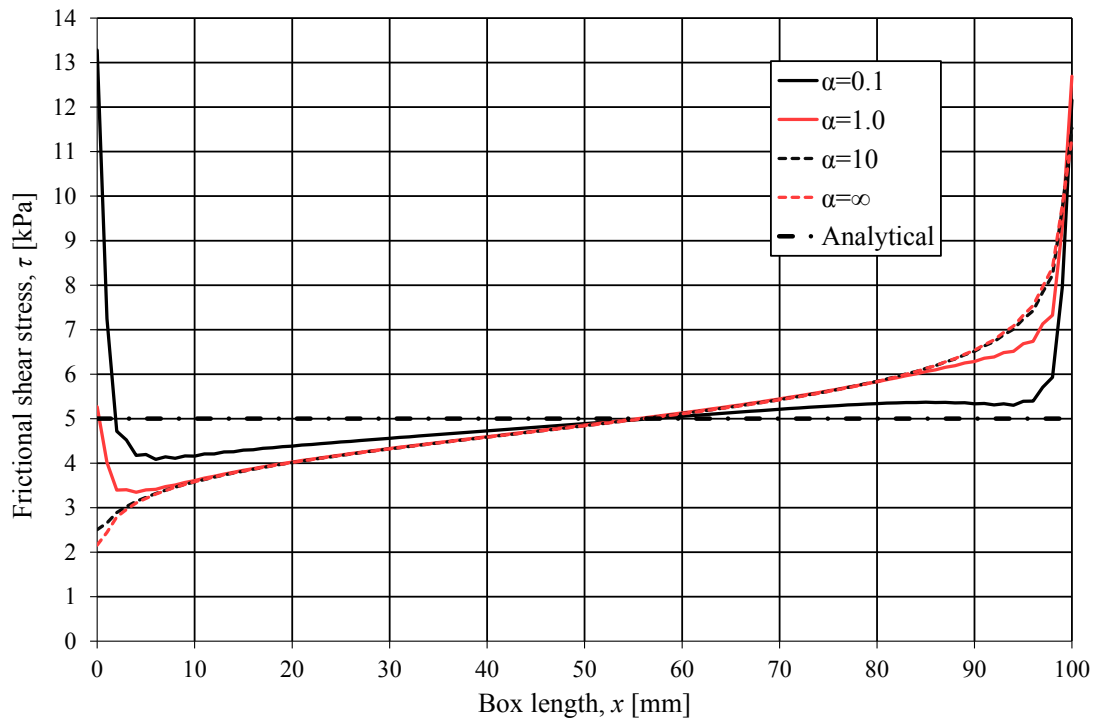


Figure 4.2 Comparison between different levels of elasticity in the box and the plate, where  $\alpha = E_{plate}/E_{box}$ .

### 4.3 Time step

Time step, with its subordinate increments, is one of the parameters that influence the result of the analysis, as described in Section 3.5.3.1. It needs to be set up properly to get a useful solution of the model. Two time steps were used in the model to catch the behaviour before and after the box started sliding. The first time step included the incremental application of the vertical pressure load which was propagated during the second time step where the horizontal load was applied progressively.

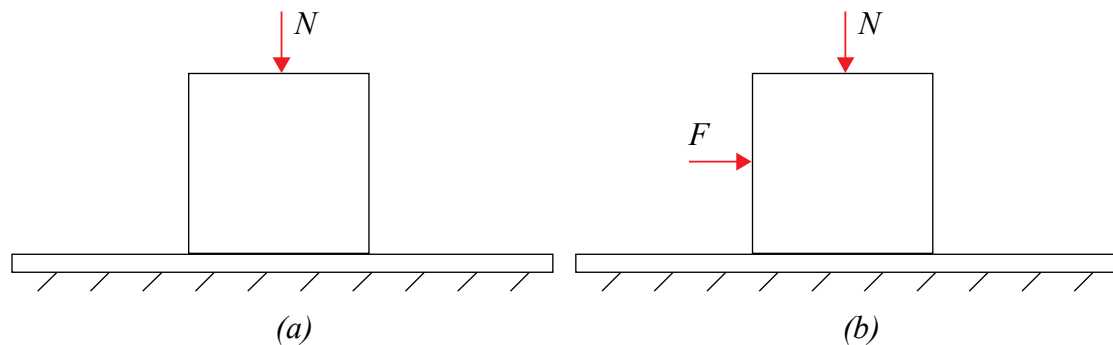


Figure 4.3 a) Step 1 – pre-stress is applied. b) Step 2 – horizontal load is applied.

The effect of different time step increments for the resulting force-displacement curve is demonstrated in Figure 4.4 where the normal force  $N$  was set to 1.0 kN, the coefficient of friction  $\mu$  to 0.5, the elastic slip was set to 0.18 mm and the total applied displacement was set to 1 mm.

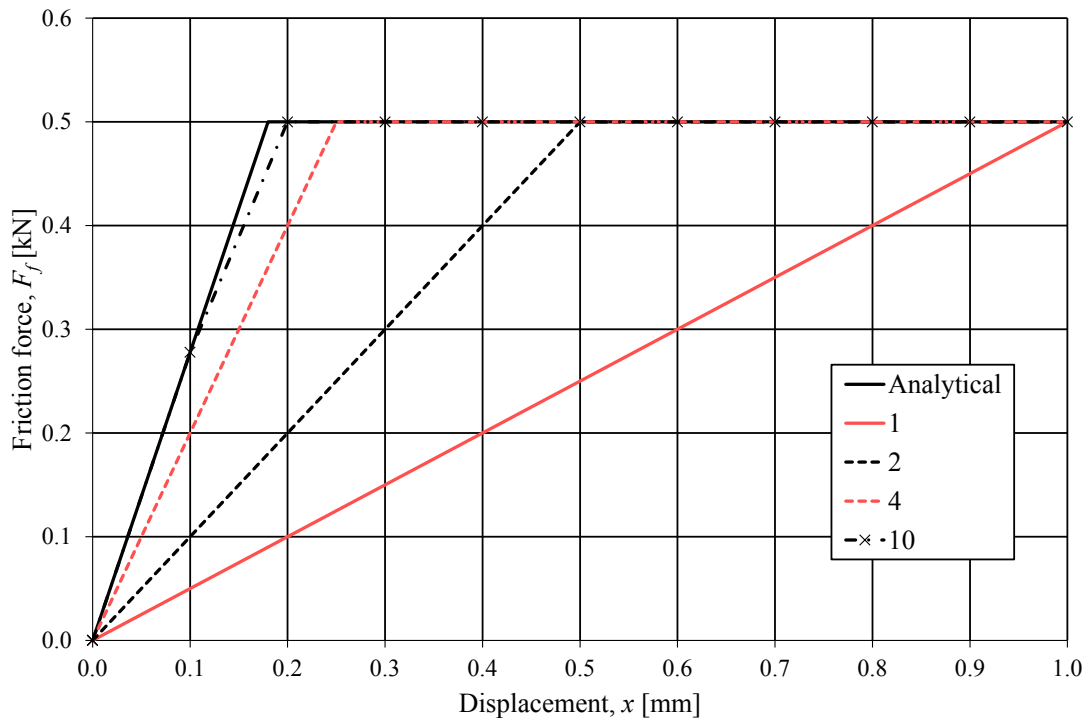


Figure 4.4 Force-displacement curve for different amounts of time step increments.

As seen in Figure 4.4 none of the time step increments used captures the exact solution for an elastic slip of 0.18 mm, even though 5 and 10 increments create good approximations. Depending on what parameters are to be studied the significance of the time step resolution varies. However for complicated contact problems it may be difficult to specify the time steps which give the real solution. Therefore using small time increments provide better results but on the other hand for too small increments the computational time might be very long without improving the result.

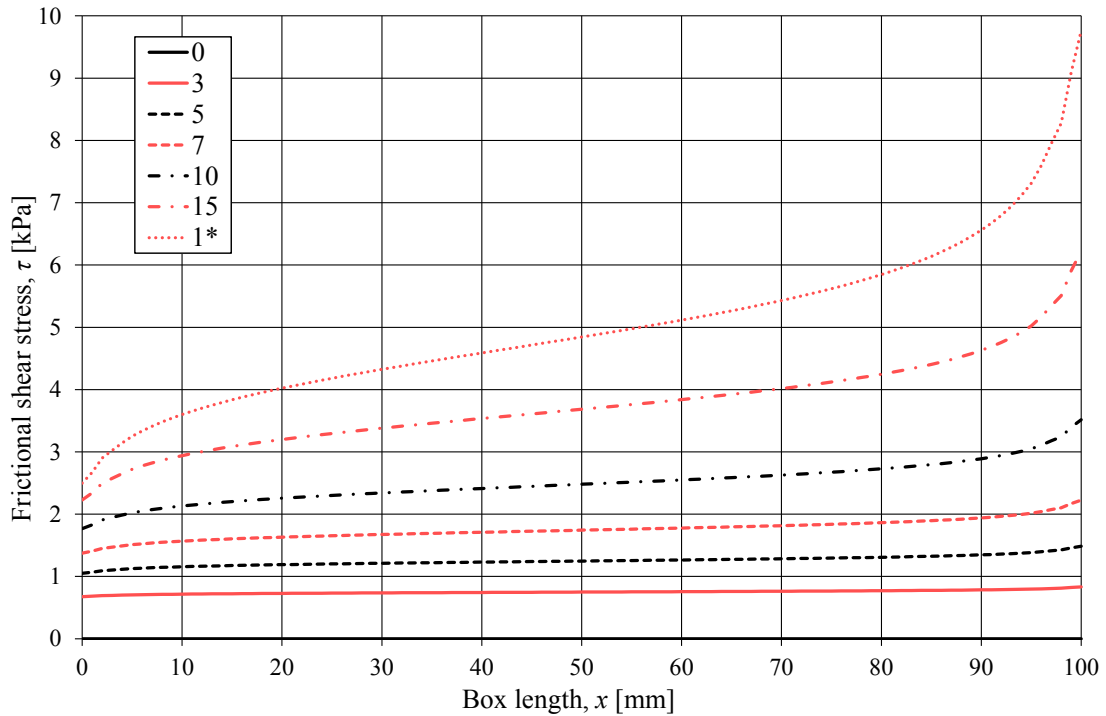


Figure 4.5 Shear stress along the bottom of the box at different time step increments.

Figure 4.5 shows the frictional shear stress along the bottom part of the box for different time step increments including both the elastic and non-elastic phase of the system. Twenty time step increments were used for the first elastic phase. The Figure shows uniform frictional shear stress propagation for an increase in time step increment that corresponds to an increase in the horizontal force on the box until it reaches 5 kN. Once the irreversible non-elastic phase was reached, at increment 20, the frictional shear stress was constant which is denoted by  $I^*$  in the legend of Figure 4.5.

## 4.4 Interaction

The frictional behaviour of a contact surface is defined in the interaction module of Abaqus. Penalty friction formulation with isotropic material properties was used to model the frictional behaviour of the contact surface. The coefficient of friction was set to 0.5 with an elastic slip of 0.5 mm before it starts to slide. Contact pairs were used with master and slave surfaces. The plate and the rigid surface were defined as the master surface in respective model since the master surface should be chosen to be the stiffer body according to Abaqus (2010). Finite-sliding was used to formulate the separation and sliding of finite amplitude and arbitrary rotation of the surfaces. No adjustment for overclosure was needed as the vertical displacement was found to be smaller than the tolerance specified by default in the program,  $10^{-16}$ . Hard contact was selected from the pressure-overclosure field.

## 4.5 Load application

There were essentially two loads acting on the box in this model, one vertical to put the bodies in contact and one horizontal to make the box slide along the plane. The vertical load was applied as a uniform pressure on top of the box while the horizontal force was applied as a displacement-controlled load. Tests were made with applying the horizontal load in different positions of the model to build on previous thesis by Hellgren and Lundberg (2011) which confirmed that there were differences in results depending on where the load is applied. In the first application method the horizontal load was applied as prescribed displacements of the left and right sides of the box see Figure 4.6 (a). This was done by defining a changing boundary condition in Abaqus, this method will consequently be referred to as BC1. The reason for displacing both sides was to simulate the behaviour of a rigid body movement and obtain a uniformly distributed shear stress.

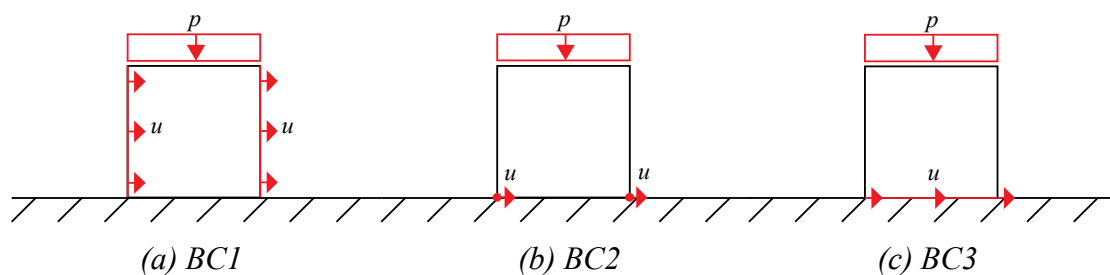


Figure 4.6 Different methods of applying the displacement-controlled load.

The second method of applying the load was by displacing the bottom corner nodes of the box, this method is referred to as BC2. The third method was by displacing the bottom side of the box and is referred to as BC3. The resulting frictional shear stress distribution over the length of the box for these different methods of load application differs noticeably as shown in Figure 4.7. Methods BC1 and BC2 have an inclined distribution whereas BC3 gave the expected result of 5 kPa when using 10 kPa of pressure and a coefficient of friction of 0.5.

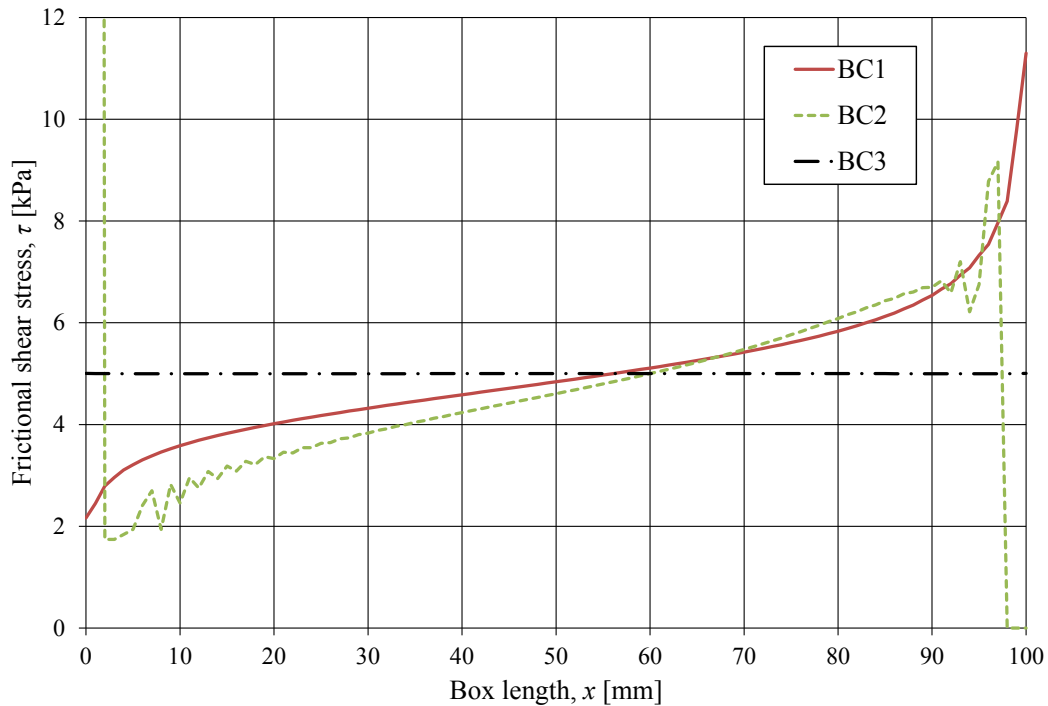


Figure 4.7 Shear stress distribution on the bottom surface of the box for the different load application methods.

In the earlier thesis by Hellgren and Lundberg the inclination of the frictional force for BC1 was explained to be caused by a moment from the force resultant at half the height of the box as shown in Figure 4.8. This is accurate when the applied load is a force or a pressure.

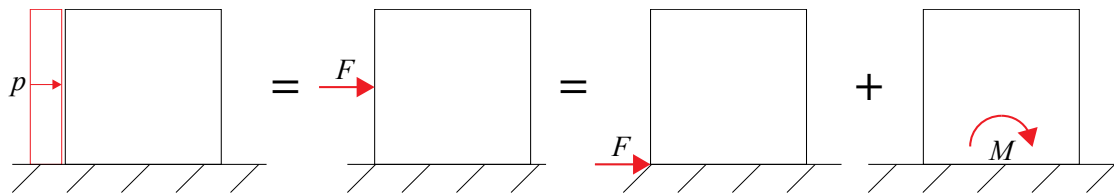


Figure 4.8 Free-body diagrams of a box displaced by a pressure.

However when using a displacement-controlled load prescribed to displace the full height of the sides evenly, the required pressure varies along the height of the box. This is because it is elastic and deforms more at the top where there are no restraints. The friction between the bodies is the only resistance for the sliding box which explains the concentration of pressure at the lower part of the box when using a displacement-controlled load.

Horizontal stresses and deformations of the box for the different boundary conditions can be seen in Figure 4.9. It is evident that stresses concentrate at the corners for BC1 and BC2 while no horizontal stresses are introduced in the box when using BC3. The horizontal scale factor used to display how the box deforms in Figure 4.9 is  $4 \cdot 10^5$  for BC1 and BC3 and  $2 \cdot 10^4$  for BC2, which displays a slightly disturbed deformation. This deformation pattern, observed for BC2, is sometimes referred to as hourglassing and is discussed in Section 3.2.1.

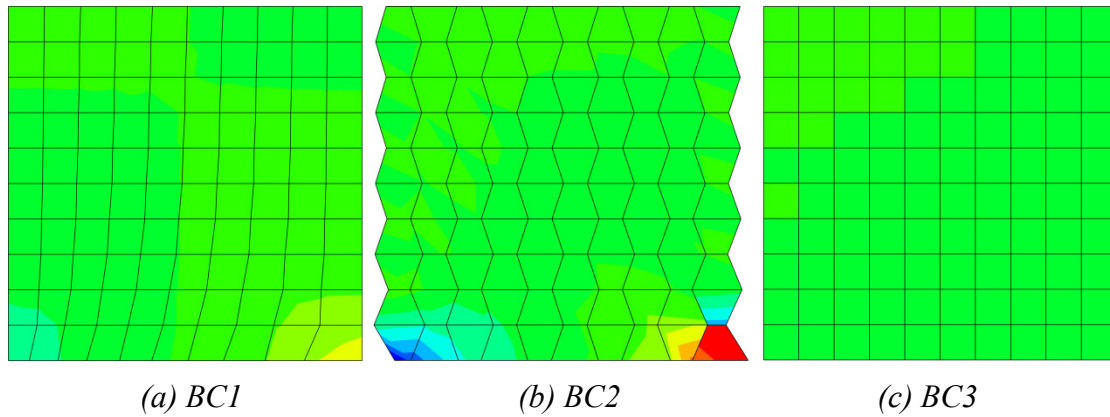


Figure 4.9 Exaggerated deformations of the box for BC1-3 with horizontal stresses plotted. Hourglass pattern was obtained for BC2.

This hourglass deformation is the source of the disturbance seen in Figure 4.7 for BC2 and can be constrained by using enhanced hourglass control for the element. Using enhanced hourglass control setting eliminates the hourglass deformation and the disturbance of the shear stress distribution. The inclination of the shear stress distribution was however somewhat increased.

For BC1, reaction forces from the left side of the box were taken out along the height, as seen in Figure 4.10. Evidently, the pressure distribution is non-uniform and concentrates at the lower part of the box. In the top part there are even tensional forces in order to displace the sides uniformly.

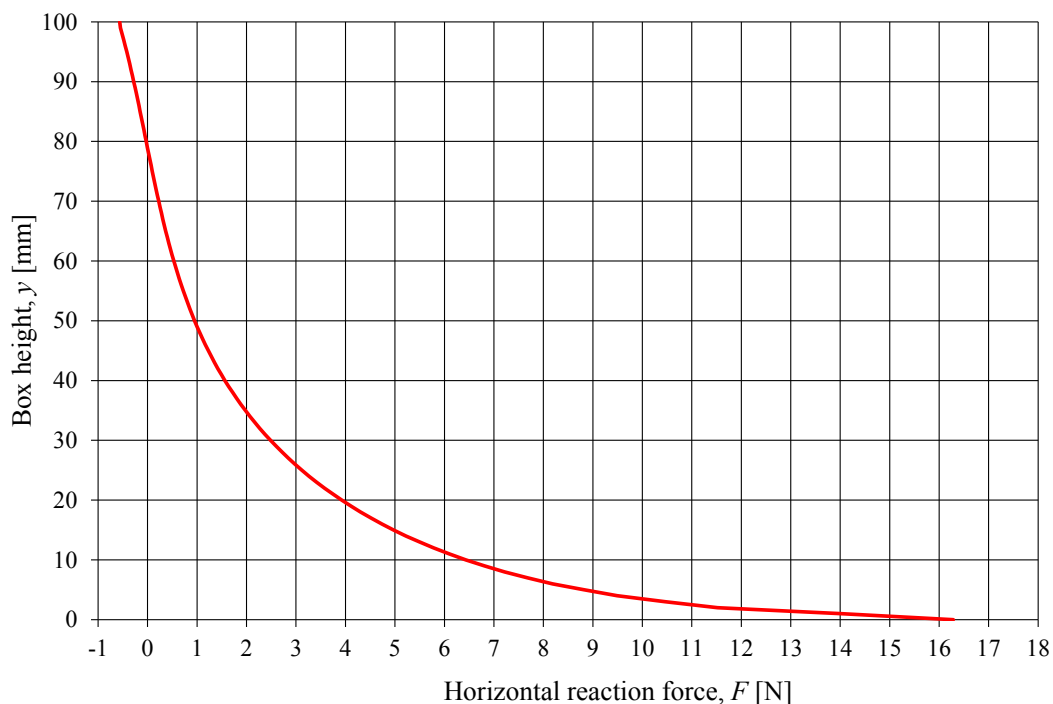


Figure 4.10 Horizontal reaction force along the height of the box.

This occurrence explains why the shear stress distribution is inclined along the length of the box, as seen in Figure 4.7, and a better free-body diagram.

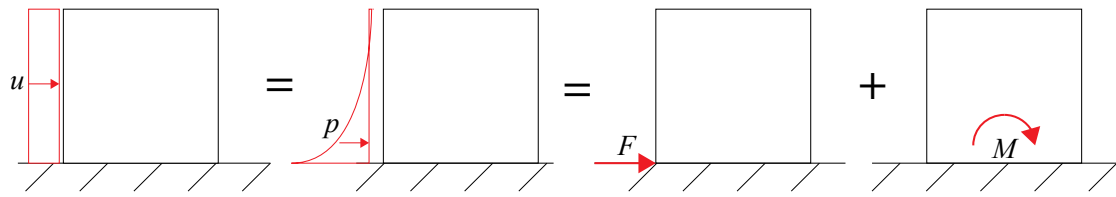


Figure 4.11 Free-body diagrams of a box displaced by a prescribed boundary condition.

## 4.6 Mesh

Three different mesh sizes were examined to get a better understanding of how the mesh size and the arrangement affect the results. The tested meshes were a coarse mesh with  $10 \cdot 10 \text{ mm}^2$  elements (Figure 4.12), a dense mesh with  $1 \cdot 1 \text{ mm}^2$  elements (Figure 4.13) and a mixed mesh consisting of eight rows of  $10 \cdot 10 \text{ mm}^2$  elements in the middle and one row of increased density,  $1 \cdot 10 \text{ mm}^2$ , at the ends of the box (Figure 4.14). Different mesh sizes for the two parts were also considered which can lead to the occurrence of small gaps or penetrations.

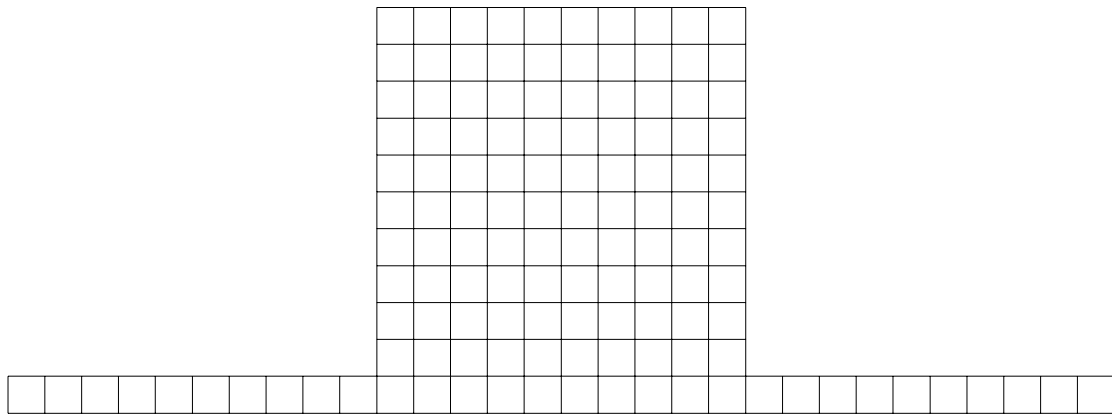


Figure 4.12 Coarse mesh with  $10 \cdot 10 \text{ mm}^2$  element size.

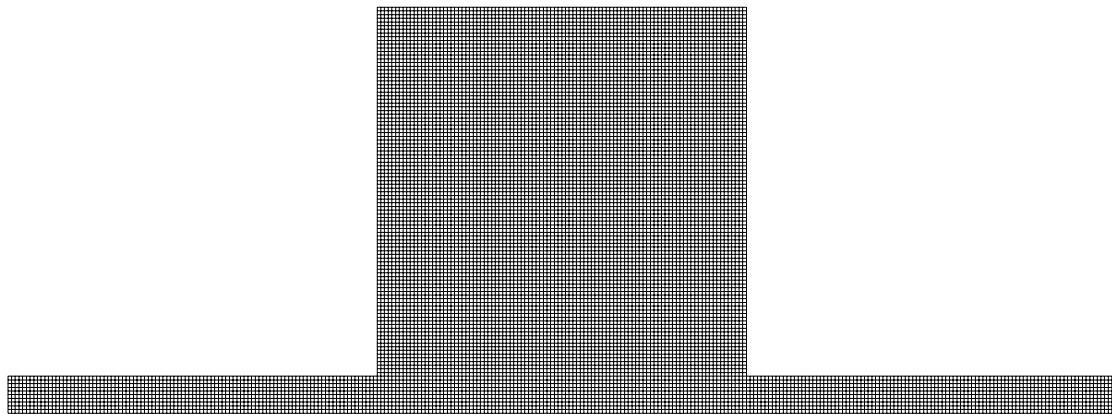


Figure 4.13 Dense mesh with  $1 \cdot 1 \text{ mm}^2$  element size.

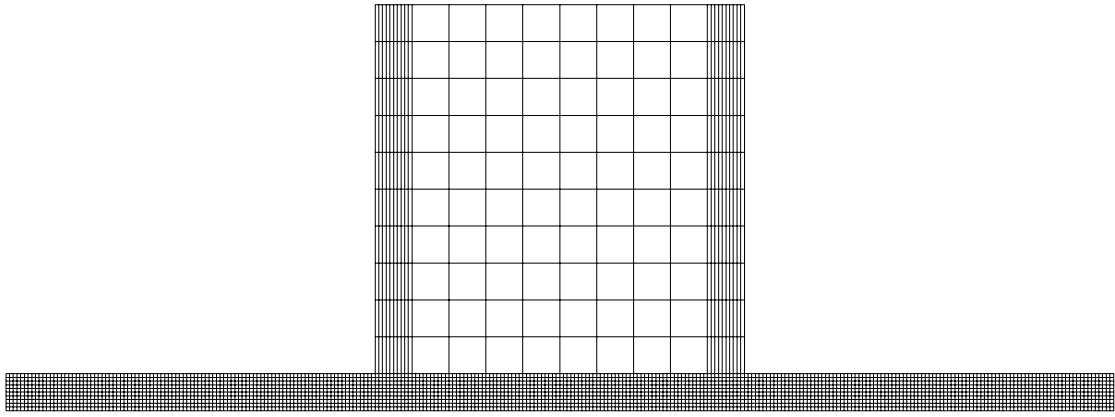


Figure 4.14 Mixed mesh,  $10 \cdot 10 \text{ mm}^2$  with locally increased density,  $1 \cdot 10 \text{ mm}^2$  element size at ends of box.

A comparison in shear stresses for the different mesh sizes and configurations can be seen in Figure 4.15. The shear stresses were taken from the bottom surface of the box and BC1 was used for the analysis.

Peak values were observed at the edges of the box when using the dense mesh and the mixed mesh. The shear stress at the intermediate part of the bottom surface of the box was the same for both dense and coarse mesh sizes. Therefore, it is recommended to use locally increased mesh density, i.e. Figure 4.14, to reduce the computational time.

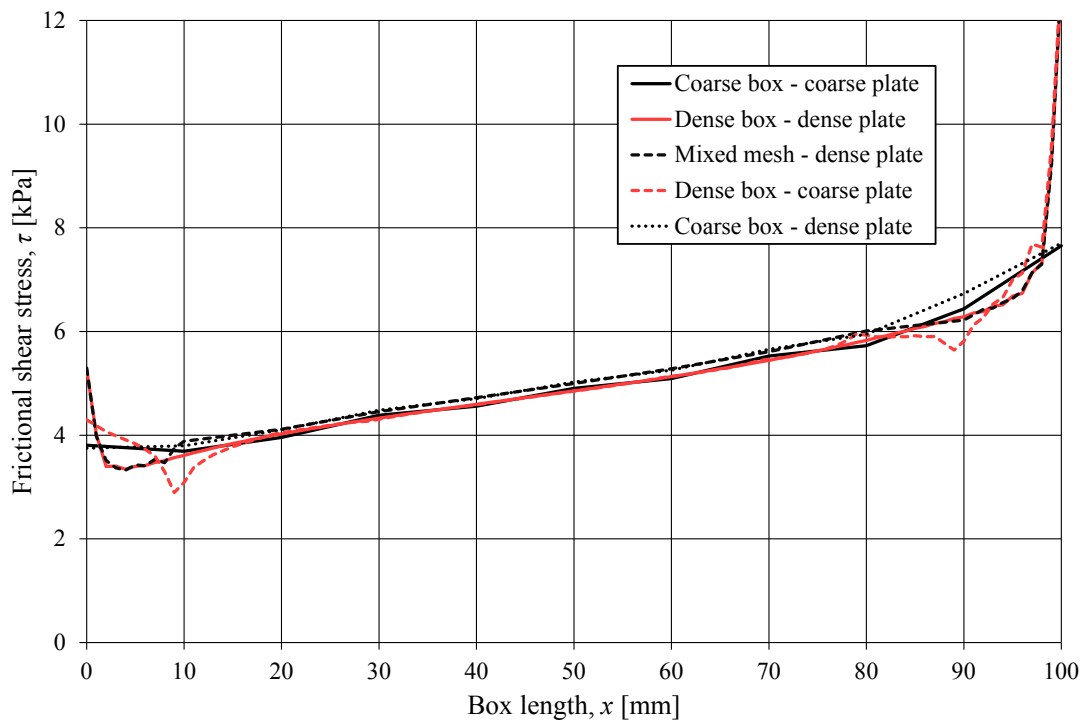


Figure 4.15 Shear stress comparison at the bottom part of the box between different mesh types using BC2.

## 4.7 Contact pressure

Contact pressure distribution is of key interest when examining the frictional behaviour between contact surfaces. The frictional shear stress is proportional to the contact pressure with the ratio of the coefficient of friction after the box starts slipping. Appropriate contact discretization should be used to get an even distribution of the contact pressure. In general, surface-to-surface discretization provides more accurate stress and pressure results than node-to-surface discretization if the surface geometry is reasonably well represented by the contact surfaces, Abaqus (2010).

The effect of modulus of elasticity on the distribution of the contact pressure was investigated with different ratio between the box and plate modulus of elasticity. Figure 4.16 shows the distribution of contact pressure for a 10 kPa pressure applied on the top surface of the box. This was done at the first time step before the horizontal displacement was applied.

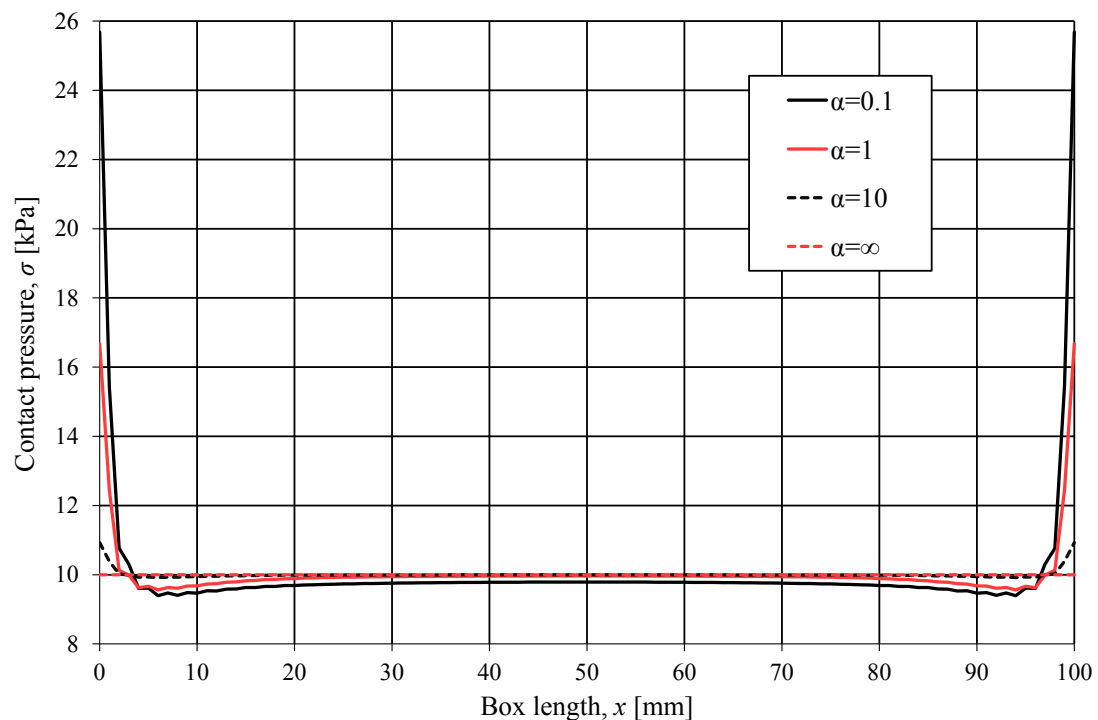


Figure 4.16 Contact pressure along the length of the box before the horizontal load is applied, where  $\alpha = E_{plate}/E_{box}$ .

Contact pressure could be expected to be uniformly distributed. However, peak values at the edge of the box are observed when the modulus of elasticity ratio,  $\alpha$ , decreases. This can be explained by the method Abaqus uses for calculating the contact pressure. The penalty method is used for constraint method by default for finite-sliding, surface-to-surface contact if a “hard” pressure-overclosure relationship is in effect. The penalty method approximates hard pressure-overclosure behaviour. With this method the contact pressure is proportional to the penetration distance, so some degree of penetration will occur, see Figure 4.17.

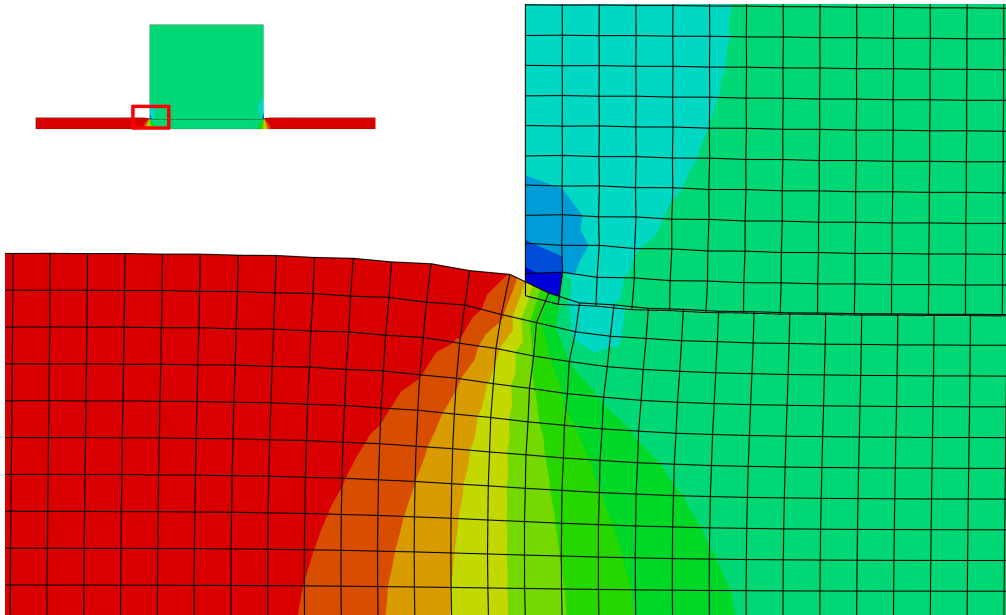


Figure 4.17 Contour plot of vertical stresses,  $\sigma_{22}$ , on deformed shape of the contact corner detail with a scale factor of 200.

An increase in the ratio of modulus of elasticity,  $\alpha$ , reduces the penetration at the outer edges of the box. This is due to the increase in the modulus of elasticity of the plate with respect to the modulus of elasticity of the box that reduces the vertical displacement at the outer contact points of the plate, see Equation (4.2). Therefore, an increase in the ratio,  $\alpha$ , evens out the contact pressure distribution at the outer contact surfaces.

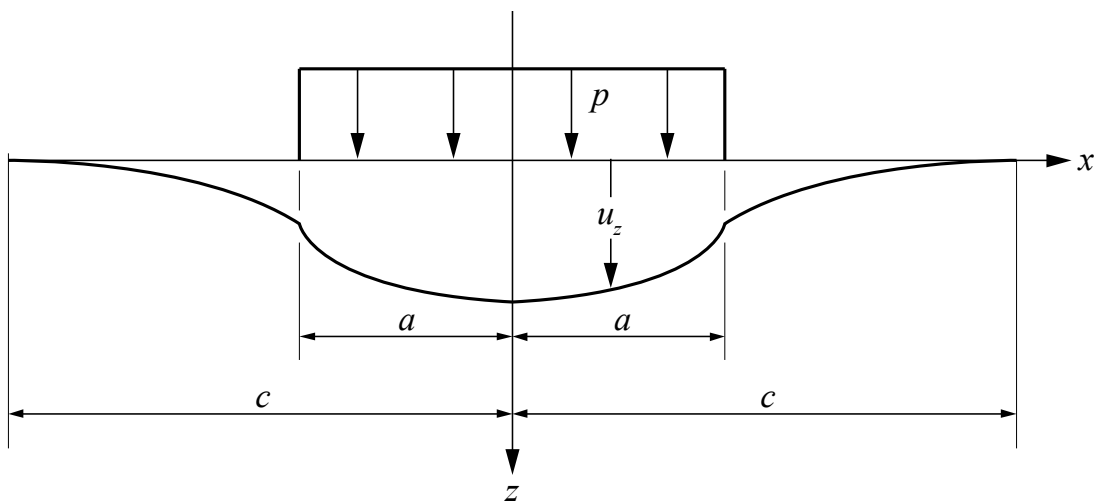


Figure 4.18 Line-loading of an elastic half-space according to Johnson (1985).

$$\frac{\partial u_z}{\partial x} = \frac{-2(1-\nu^2)}{\pi E} P(\ln(a+x) - \ln(a-x)) \quad (4.1)$$

$$u_z = -\frac{(1-\nu^2)}{\pi E} P \left\{ (a+x) + \ln\left(\frac{a+x}{a}\right)^2 + (a-x) \ln\left(\frac{a-x}{a}\right)^2 \right\} + C \quad (4.2)$$

Where:

$E$  Modulus of elasticity of the plate

$\nu$  Poisson's ratio of the plate

$P$  Normal pressure

The constant  $C$  in Equation (4.2) is fixed by the datum chosen for normal displacements. In Figure 4.18 the normal displacement is illustrated on the assumption that  $u_z = 0$  when  $x = \pm c$ .

## 5 Model 2 – Simplified SLT deck

### 5.1 Background

Full-scale experimental tests have been performed at Chalmers in order to better understand the behaviour of SLT decks and the influence of a variety of parameters, see Figure 5.1. The results from tests were used as a background for verifying the full-scale finite element models in Chapter 6.



Figure 5.1 Setup of experimental testing of a narrow SLT deck at Chalmers, Ekholm (2012).

The geometry of a narrow deck is shown in Figure 5.2. The deck was supported on 20 mm thick steel plates placed on steel cylinders with length equal to the width of the slab and the load consists of two point loads which are denoted B in Figure 5.2.

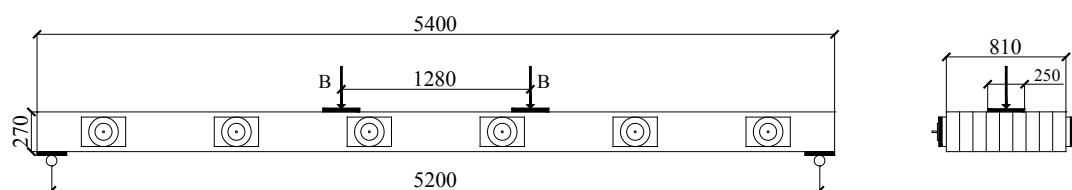


Figure 5.2 Geometry and load condition of the studied slab, dimensions in mm.

The structure consisted of nine laminations with a height of 270 mm and a width of 90 mm, where the load was applied onto the three middle beams in two points on square plates. The beams were pre-stressed together in the transverse direction using six pre-stressing bars attached to the plates.

Before the full-scale model in Figure 5.2 was analysed, a simplified model was made by replacing the nine beams with three beams to reduce the computational time and make parametric studies. A model with one beam was performed to examine the influence of mesh size on the results and to determine the appropriate mesh for both simplified and full-scale models.

## 5.2 Model with one beam

A model with one beam representing the three laminates in the middle part of the slab was analysed, see Figure 5.3. This beam was used to verify the model by comparing bending stress, shear stress and the deflection at mid-span with the results from hand calculation. This comparison was made to determine the appropriate mesh size for the full-scale model.

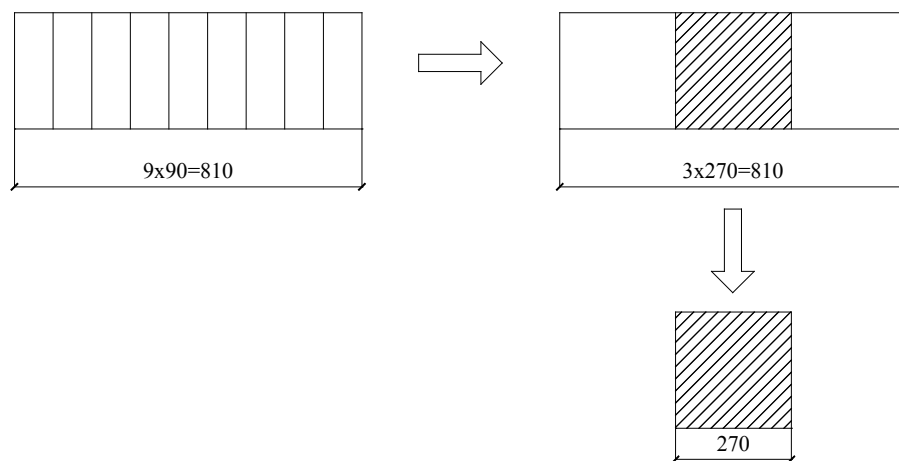


Figure 5.3 Illustration of how one beam was taken out from the full-scale model, dimensions in mm.

### 5.2.1 Material properties

The beam was assigned a modulus of elasticity similar to that of a glulam beam by setting its value to 12 GPa. Isotropic material properties were assigned for this model. Poisson's ratio was set to zero in order to simplify the model as it has no significant influence for such analyses.

### 5.2.2 Boundary conditions and load application

For hand calculations, the beam was modelled as a simply supported beam subjected to a concentrated load of 100 kN at two points, see Figure 5.4. However, in FE modelling a symmetry boundary condition was assigned by setting  $u_x$  to zero at mid-section of the beam to simplify the analyses. On the left part of the FE model, the boundary was assigned on one line of nodes by setting displacement  $u_y$  and  $u_z$  to zero. A distributed pressure load was used for the FE model that corresponds more to the real loading condition in the lab test, see Figure 5.5.

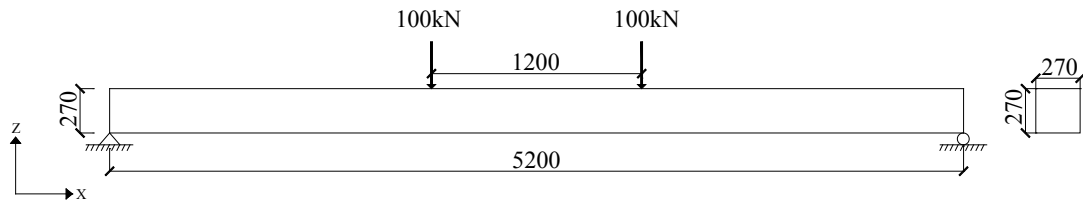


Figure 5.4 Illustration of one beam with acting load used for hand calculations, dimensions in mm.

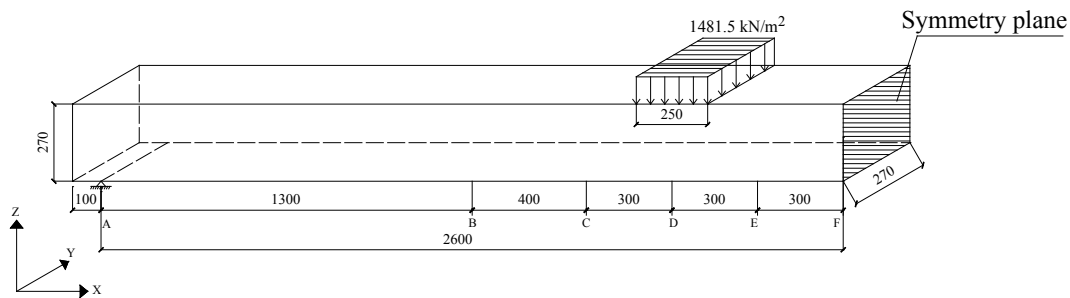


Figure 5.5 Illustration of one beam with acting load and sections where data is taken out from in the FE model, dimensions in mm.

### 5.2.3 Element mesh

The influence of the element mesh was studied using different mesh distributions. The mesh in the transverse direction was chosen to be two elements for each of the original nine beams; thus resulting in  $3 \cdot 2 = 6$  elements for each three beams.

In the vertical direction the mesh distribution was of interest in order to better quantify the distribution of the bending and shear stresses of the cross section. Hence, three regions were defined ( $h/4 + h/2 + h/4$ ) in which the elements were distributed, see Figure 5.6. Five different mesh size distributions for both equally and unequally distributed mesh types were investigated.

- Equally sized element distribution
  - 8 elements (2+4+2)
  - 16 elements (4+8+4)
  - 24 elements (6+12+6)
- Unequally sized element distribution
  - 12 elements (4+4+4)
  - 24 elements (8+8+8)

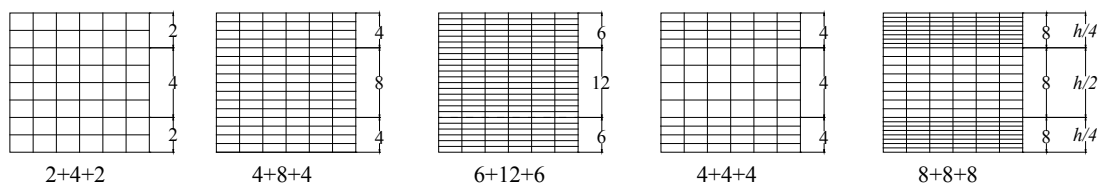


Figure 5.6 Mesh distribution along the height of the beam.

To determine the accuracy of the finite element analysis, a comparison was made with hand calculations for the maximum vertical deflection,  $u_z$ , maximum bending stress,  $\sigma_x$ , and maximum shear stress,  $\tau_{xz}$ . The analyses were made using different mesh sizes along the height direction. The mesh size for the beam was determined to get better result with respect to calculation time and result accuracy.

The maximum vertical deflection,  $u_z$ , in the middle of the beam was calculated according to Equation (5.1), where the first part of the expression represent the deflection due to flexural bending and the second part is deflection due to shear. For symmetrically acting concentrated loads, the vertical deflection at mid-section of the beam should be calculated as twice the value from Equation (5.1). The maximum bending stress in the x-direction,  $\sigma_x$ , was calculated according to Equation (5.2) and the maximum shear stress,  $\tau_{xz}$ , was calculated according to Equation (5.3).

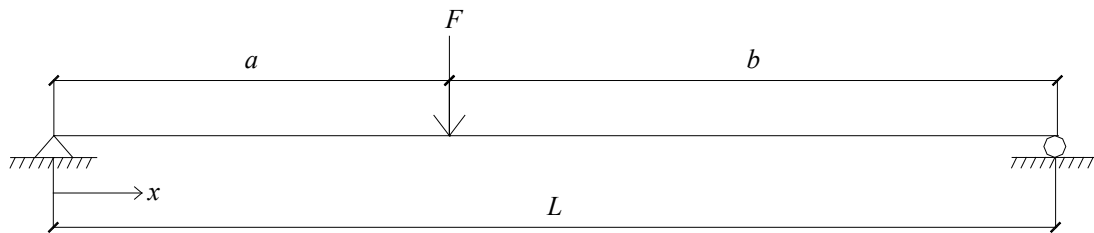


Figure 5.7 Simply supported beam loaded by a concentrated load.

$$\begin{aligned}
 u_z &= \frac{Fbx}{6EIL}(L^2 - b^2 - x^2) + \frac{Fbx}{LAG} & 0 \leq x \leq a \\
 u_z &= \frac{Fb}{6EIL} \left[ \frac{L}{b}(x-a)^3 + (L^2 - b^2)x - x^3 \right] + \frac{Fb(L-x)}{LAG} & a \leq x \leq L
 \end{aligned} \quad (5.1)$$

Where:

- $E$  Modulus of elasticity
- $G$  Shear modulus,  $G = E/2$  for  $\nu = 0$
- $A$  Cross-sectional area
- $I$  Moment of inertia
- $F$  Concentrated force
- $L$  Length of the beam

$$\sigma_x = \frac{M}{W} \quad (5.2)$$

Where:

- $M$  Maximum moment in mid-span
- $W$  Bending resistance of the cross section

$$\tau_{xz} = \frac{3V}{2A} \quad (5.3)$$

Where:

$V$  Maximum shear force

## 5.2.4 Results

Figure 5.8 shows the different mesh distribution used for analysing the bending stress distribution which can be compared against the analytical bending stress calculated using Equation 5.2. The mesh distribution of 8+8+8 elements yields good results at the top and bottom parts of the beam section compared to the other mesh distributions.

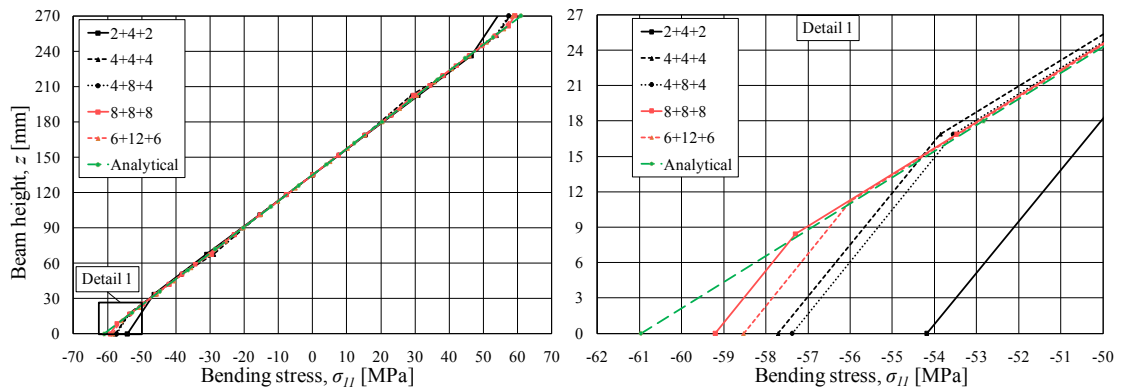


Figure 5.8 Vertical bending stress distribution for different mesh distributions.

The discrepancy between the analytical and numerical solution is due to that the values at the edges, where  $z$  is 0 and 270 mm, are taken from the integration point in that element and not at the outermost fibre. Hence, the stress shown is somewhat underestimated, and for a mesh distribution of 8+8+8 elements it is approximately 3 % too low.

To find an appropriate mesh distribution along the beam height, shear stresses were also investigated for different mesh distributions. To find an undisturbed shear stress distribution, six different sections were considered at different distances from the support section, see Figure 5.9. The stress concentration at the support creates disturbed results at sections close to the support. Section B was chosen for comparison of different mesh distributions and shows a comparatively smooth parabolic shape and maximum shear stress distribution.

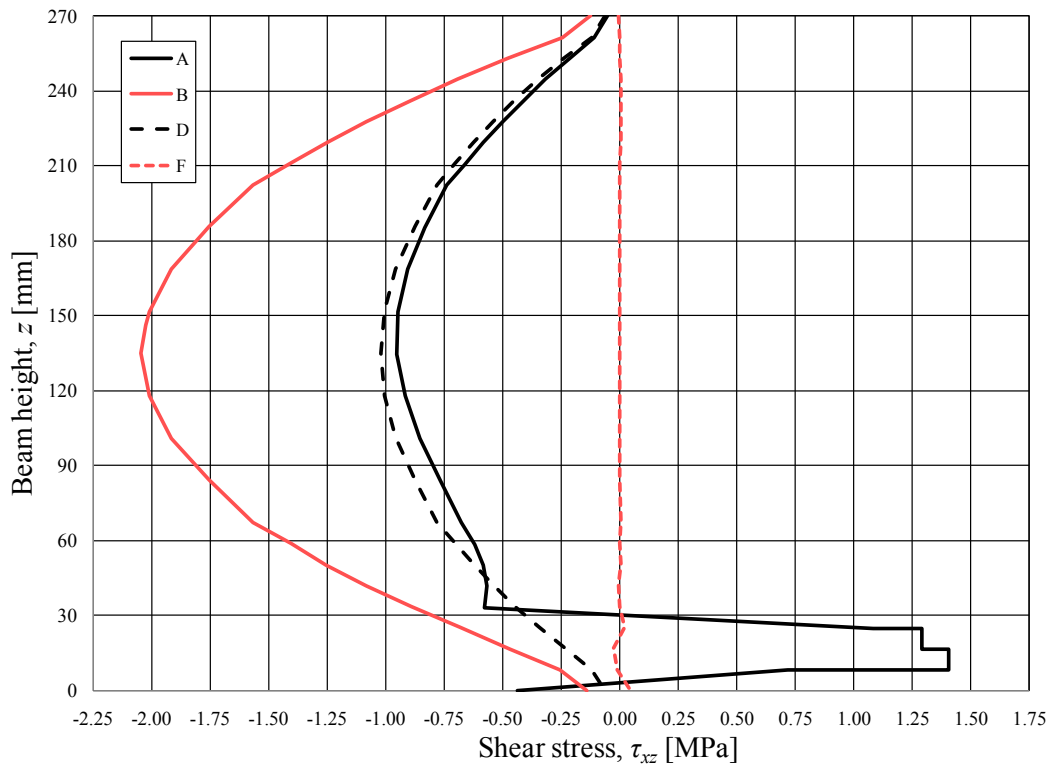


Figure 5.9 Shear stress distribution at different sections, sections are given in Figure 5.5.

The different shear stress distribution for equal and unequal mesh size along height of the beam were compared with the analytical parabolic shear distribution, see Figure 5.10.

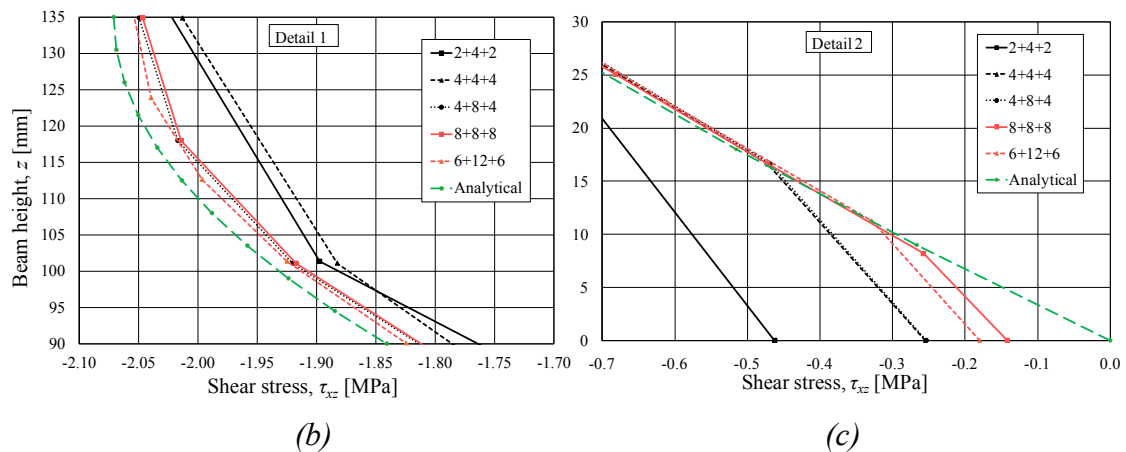
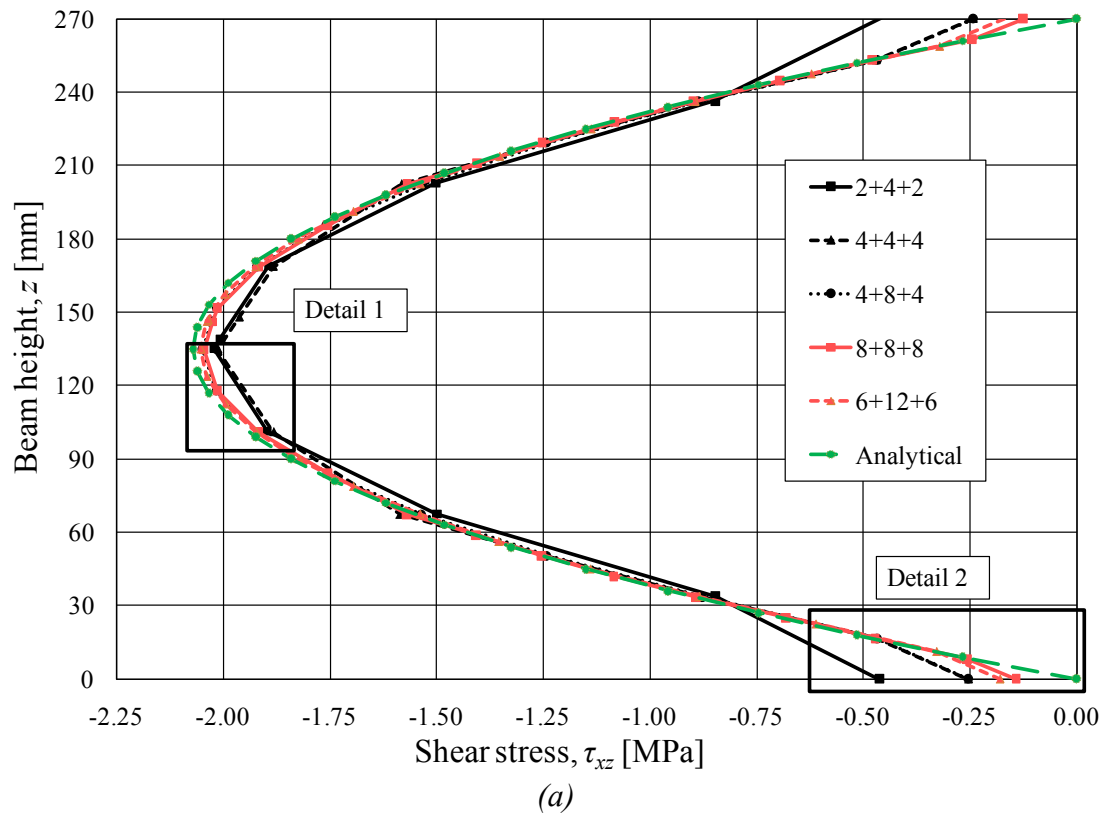


Figure 5.10 Shear stress,  $\tau_{xz}$ , for different mesh distributions.

The shear stresses,  $\tau_{xz}$ , at section B are shown for different mesh distributions in Figure 5.10. The 6+12+6 distribution shows good correspondence with the analytical curve at the mid part of the beam section as shown in Detail 1, Figure 5.10 (b). This is due to the 6+12+6 distribution has a finer mesh size at the mid part of the beam section that gives a high accuracy to the result. On the other hand, the 8+8+8 distribution also gives a good result at the lower and upper part of the beam as it has a finer mesh size in these regions as shown in Detail 2.

A comparison of the finite element analyses for the different mesh distribution against hand calculation is shown in Table 5.1. The mesh distributions with finer mesh sizes show more accurate values compared to the coarser mesh sizes. Due to the need to capture the contact behaviour properly, a non-uniform mesh distribution with finer mesh at the outer edges of the beam was preferred as discussed in Section 4.6.

Unequal mesh distribution with the 8+8+8 distribution was chosen in order to capture good results for both shear and bending stresses.

The vertical deflection at the mid-section of the beam from the FE model was compared with the hand calculation for different mesh distributions. For all different mesh distributions, the ratio between the FE results with the hand calculation was less than 1 % which was acceptable.

Table 5.1 Comparison of different mesh distribution along the height of the beam.

Mesh type	Shear stress		Bending stress		Deflection	
	$\tau_{xz}$ [MPa]	[%]	$\sigma_x$ [MPa]	[%]	$u_z$ [m]	[%]
Analytical	2.07	-	60.96	-	-0.103	-
2+4+2	2.02	2.3	54.18	11.1	-0.104	0.9
4+4+4	2.01	2.8	57.71	5.3	-0.103	0.4
4+8+4	2.05	1.0	57.37	5.9	-0.103	-0.2
8+8+8	2.04	1.2	59.20	2.9	-0.102	-0.4
6+12+6	2.05	0.8	58.52	4.0	-0.102	-0.4

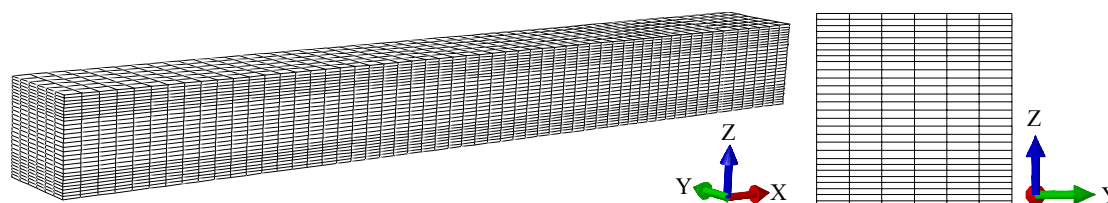


Figure 5.11 The selected mesh distribution, 8+8+8, for one beam.

The longitudinal mesh distribution was determined based on the pre-stress distribution discussed in Section 5.3.3.

### 5.3 Model with three beams

In order to reduce the computational time of the analysis and the complexity of the problems the slab with nine laminations was studied by replacing it to three beams as shown in Figure 5.12. This way all but the most critical surface interactions are excluded so that the overall behaviour is maintained.

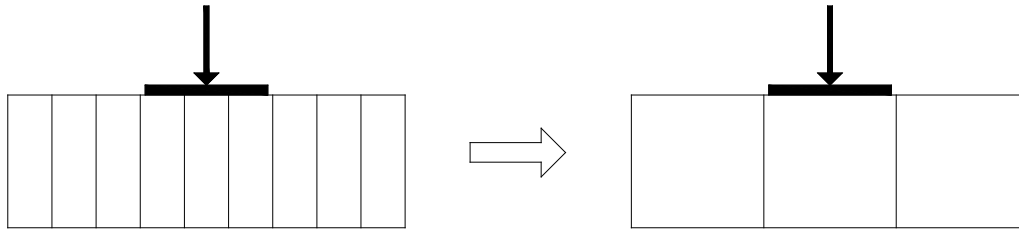


Figure 5.12 Illustration of how the nine laminations were substituted with three beams.

### 5.3.1 Material properties

All the three beams were assigned a material property similar to that of a glulam beam by assigning an anisotropic material with a longitudinal modulus of elasticity set to 12 GPa. The Poisson's ratio was set to zero in order to simplify the model as it has no significant influence for such analyses. The coefficient of friction and elastic slip for the contacting surfaces were set to 0.3 and 0.1 mm respectively.

### 5.3.2 Boundary conditions and load application

A symmetry boundary condition was assigned by setting  $u_x$  to zero at the mid-section of the beams to simplify the analyses, see Figure 5.13. On the left part of the model, the boundary condition was assigned to the bottom part of the beams on one line of nodes by setting vertical displacement,  $u_z$ , to zero. At the bottom, middle node of the middle beam transversal displacement,  $u_y$ , is set to zero. Displacement control was used as the load application method on the loading area. The displacement was set to 150 mm for all analyses.

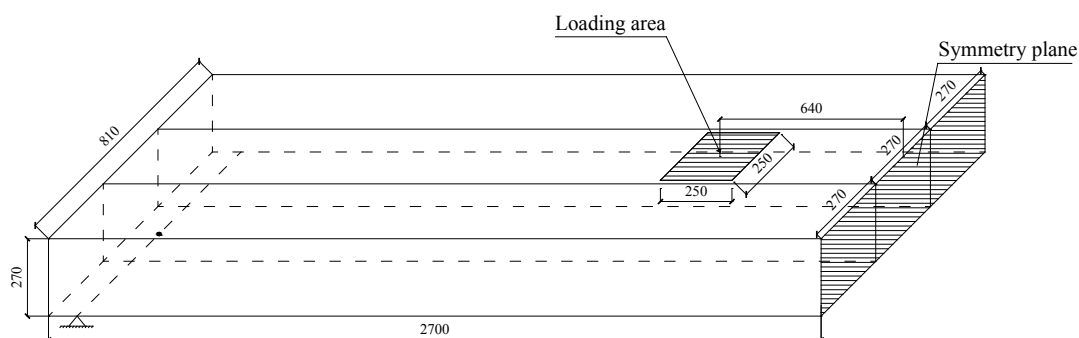


Figure 5.13 Illustration of the model with three beams, dimensions in mm.

### 5.3.3 Type of pre-stressing

Different pre-stressing models were analysed to investigate the differences when using different pre-stressing models. This investigation was used to determine what type of pre-stressing to use for the full-scale model. Two pre-stressing models were studied:

1. Equal pressure applied along the full length of the beam, see Figure 5.14.

2. Equal pressure applied in the local areas corresponding to the anchorage plates, see Figure 5.15.

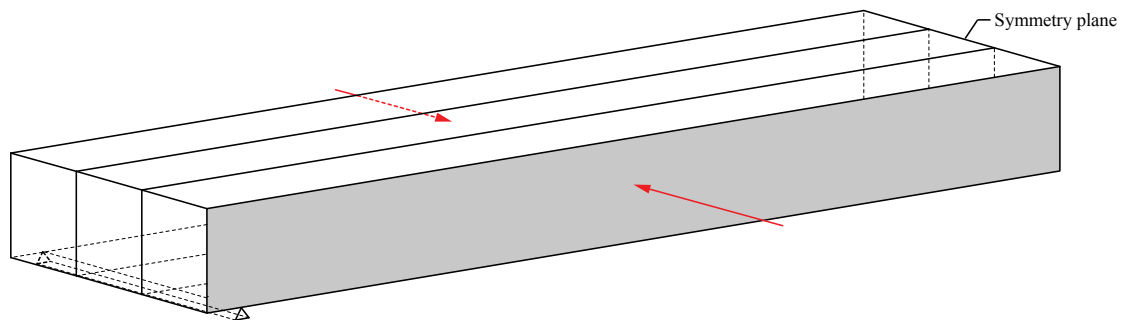


Figure 5.14 Uniformly applied pre-stress pressure along the full length of the outer laminations.

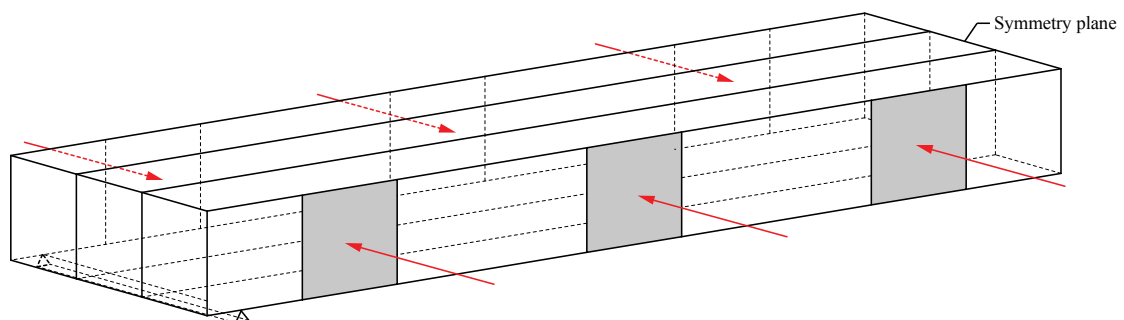


Figure 5.15 Locally applied pre-stress pressure.

The pressure used for the locally applied pre-stress type is given as:

$$p_l = \frac{A_f p_u}{zC} \quad (5.4)$$

Where:

- $p_u$  Uniformly applied pre-stress pressure
- $p_l$  Locally applied pre-stress pressure
- $A_f$  Area of the beam face
- $z$  Height of the beam
- $C$  Centre to centre spacing of pre-stressing plates

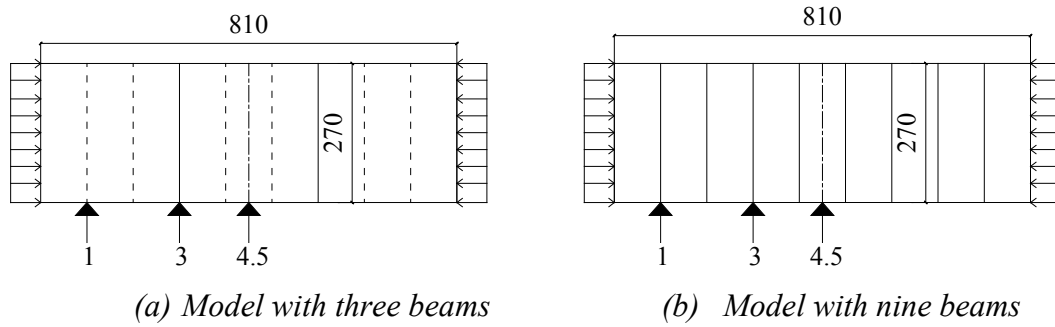


Figure 5.16 Illustration of interlaminar surfaces where the pre-stress distribution was checked.

The difference pre-stress distribution was checked at different lamination surfaces along the deck width as shown in Figure 5.16. The pre-stress distribution at different lamination surfaces for both uniformly applied pre-stress pressure and locally applied pre-stress pressure, see Figure 5.17. For uniformly applied pre-stress along the full length of the outer laminations, the pre-stress will be uniform in all lamination surfaces. However, local pre-stress pressure creates a non-uniform pressure distribution along the length of the beam. The pre-stress distribution evens out when it gets to the inner surfaces of the lamination.

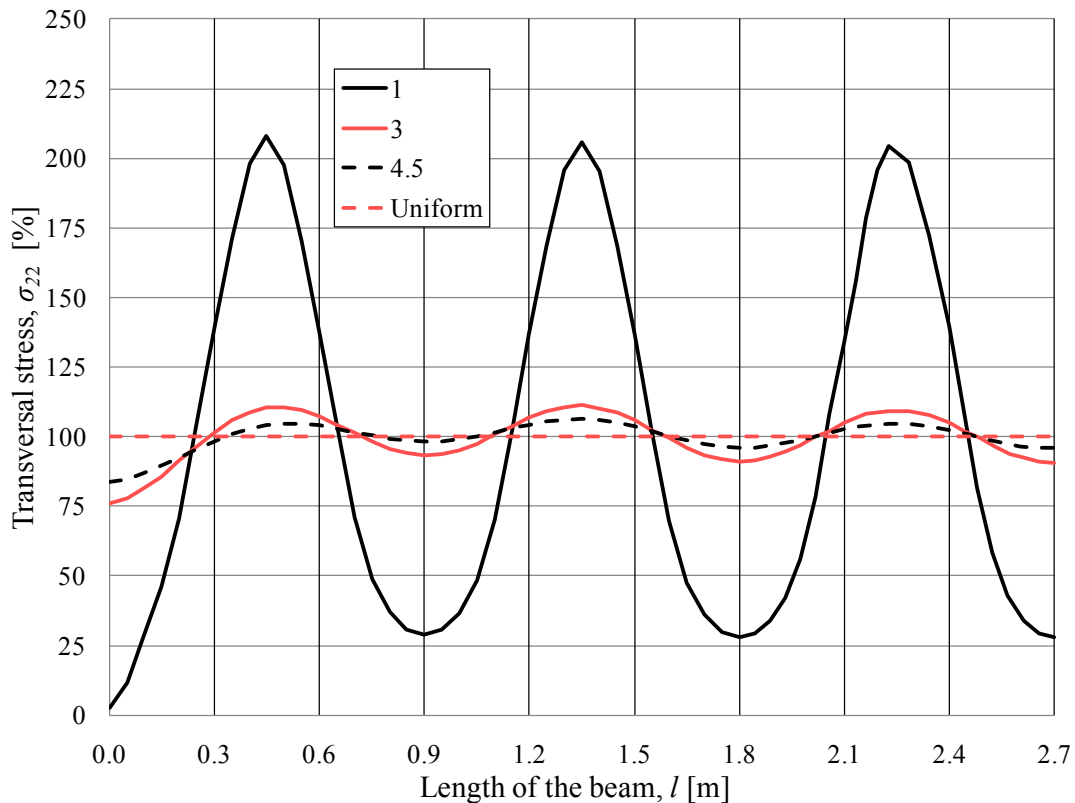


Figure 5.17 Transversal stress distribution of the model with three beams with 600 kPa of pre-stress for uniform and local application. The numbers 1, 3 and 4.5 indicate at what number of laminations into the deck the results were taken for the local pre-stressing type, see Figure 5.16.

The model with three beams results in a more even pressure for locally applied pressure compared to the full-scale model consisting of nine beams. The increased amount of total slip because of the increased number of contact surfaces in the model with nine beams is the reason for the increased uneven pressure distribution compared to the model with three beams, see Figure 5.18.

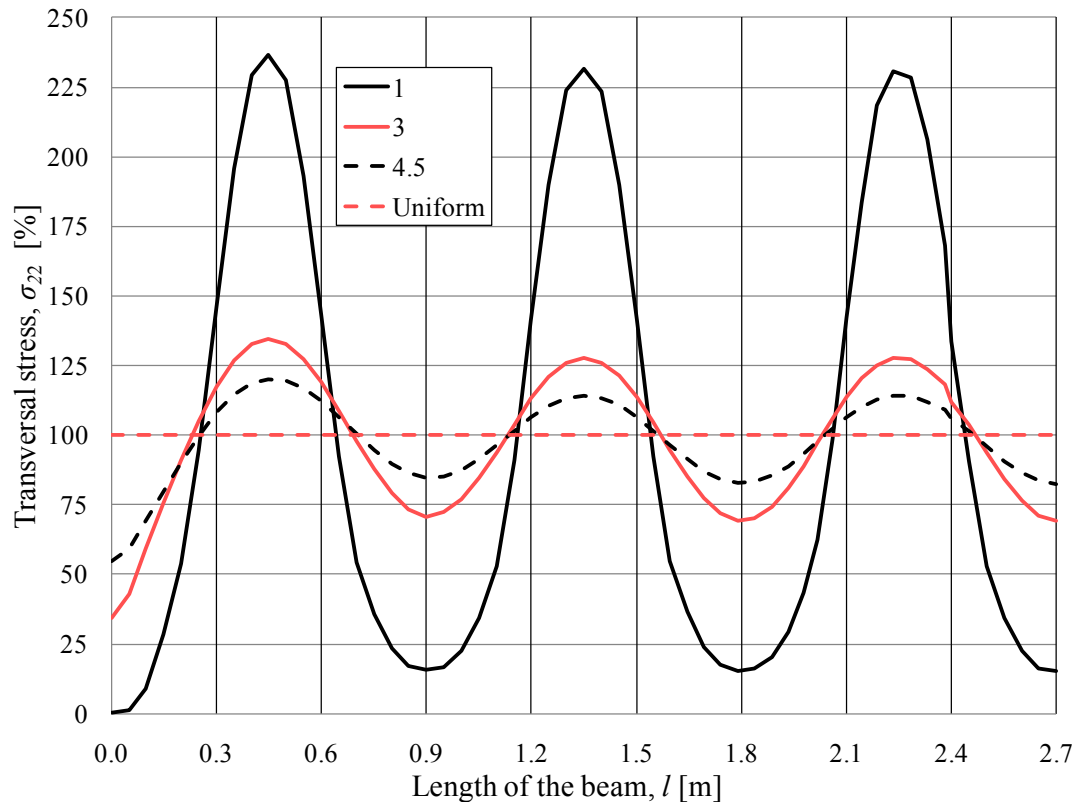


Figure 5.18 Transversal stress distribution of the model with nine beams with 600 kPa of pre-stress for uniform and local application. The numbers 1, 3 and 4.5 indicate at what number of laminations into the deck the results were taken for the local pre-stressing typ, see Figure 5.16.

Despite this difference between different pre-stress types, equal pressure was used in model with three beams since the purpose was to study the influence of other parameters.

Different elastic slip was examined in order to check what influence it has on the pre-stress distribution as shown in Figure 5.19. The pre-stress distribution was taken at the mid-section of the deck width, i.e. section 4.5 in Figure 5.16, to get the most even distribution. For elastic slip between 0.1 mm to 1.0 mm range, it was observed that varying the elastic slip has no significant influence on the pre-stress distribution.

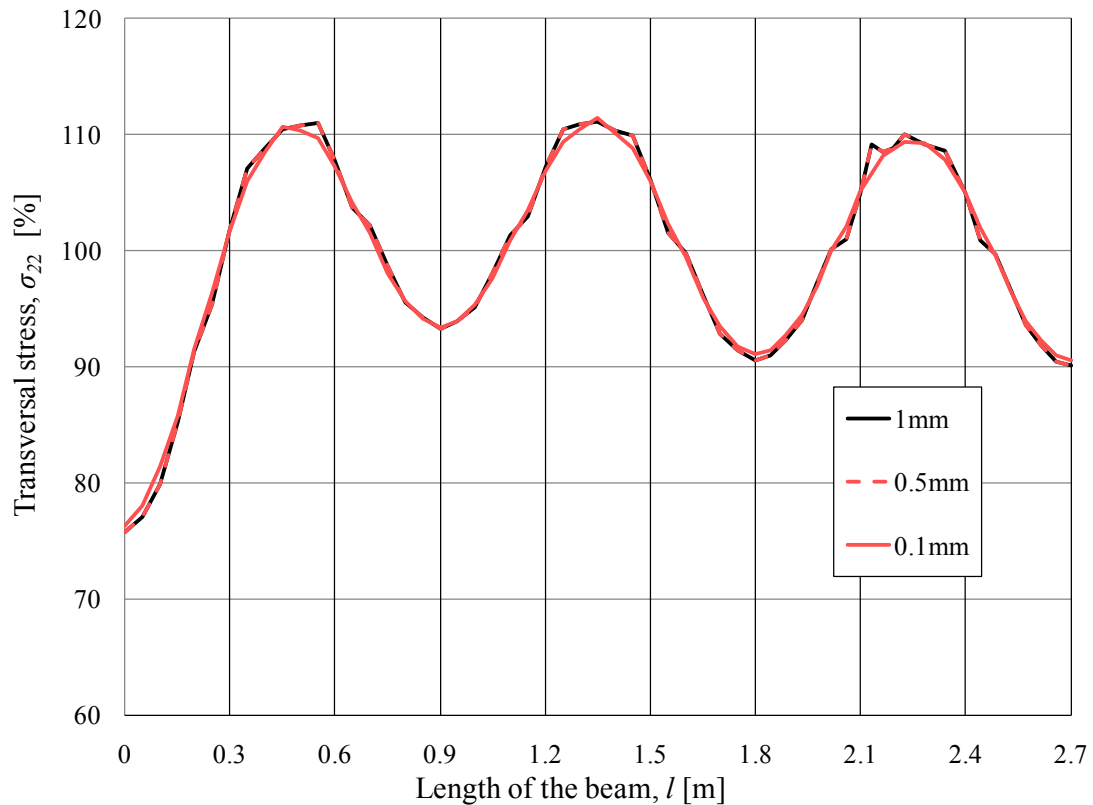


Figure 5.19 Pre-stress distribution at section 4.5 for different values of elastic slip and a 600 kPa pre-stressing.

In order to be able to see what effect mesh density has on pre-stress distribution in the longitudinal direction of the beam, two different mesh sizes, 50 mm and 100 mm, were examined. A finer mesh yields more accurate pre-stress distribution compared to a coarse mesh even though the difference is rather small, see Figure 5.20. For the full-scale model 50 mm mesh size was chosen for meshing in the longitudinal direction of the beam.

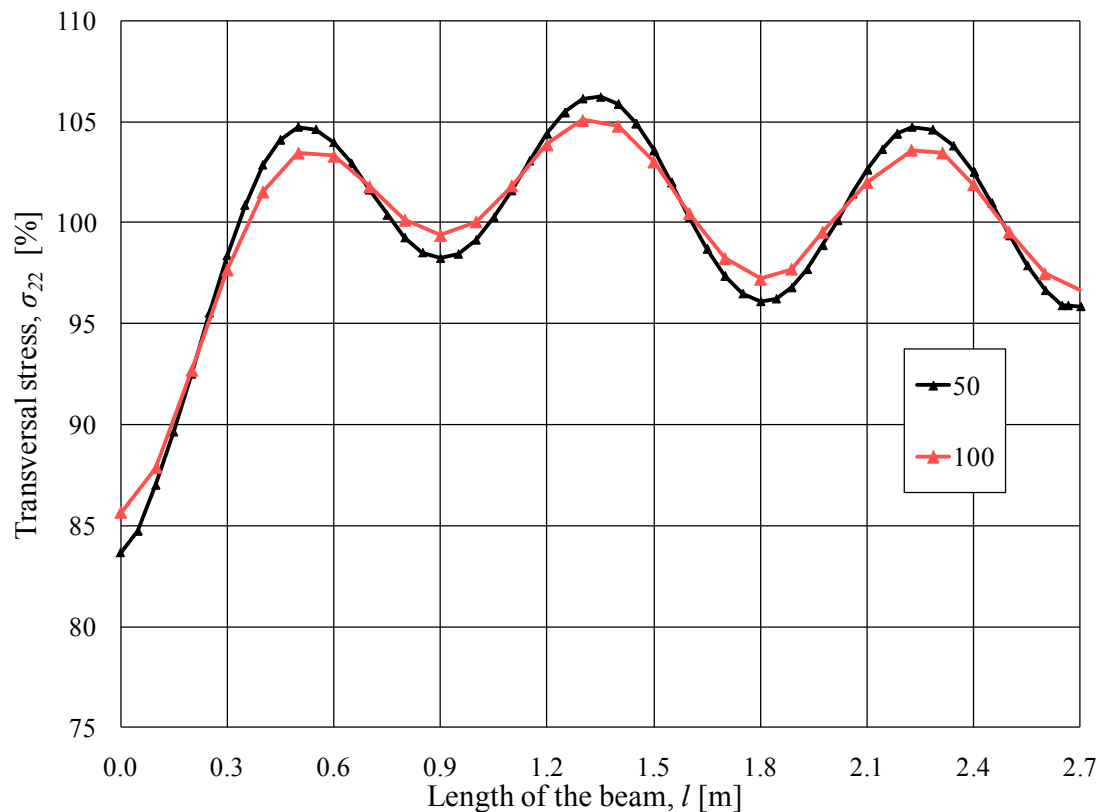


Figure 5.20 Comparison between 50 and 100 elements along the longitudinal direction of the deck.

### 5.3.4 Influence of pre-stress level

To study the resulting behaviour of different pre-stress levels, analyses were made with pre-stressing levels of 100 kPa, 300 kPa and 600 kPa while keeping other parameters constant. Different parametric comparisons were made for different pre-stress levels.

#### 5.3.4.1 Beam deflection

The overall behaviour of load versus deflection can be seen in Figure 5.21. All three pre-stress levels display a linear behaviour up until a certain point where they start to deviate from the straight line corresponding to fully linear elastic behaviour and is plotted for reference. These points of deviation mark the initiation of interlaminar slip (see Figure 3.4) in the deck which is continued while the stiffness approaches approximately one third of the initial stiffness. When slipping initiates the behaviour of the loaded part of the deck will shift from that of an orthotropic plate with a width of three beams to that of a single beam with an effective width, which in this case simply will be the middle part of the three beams.

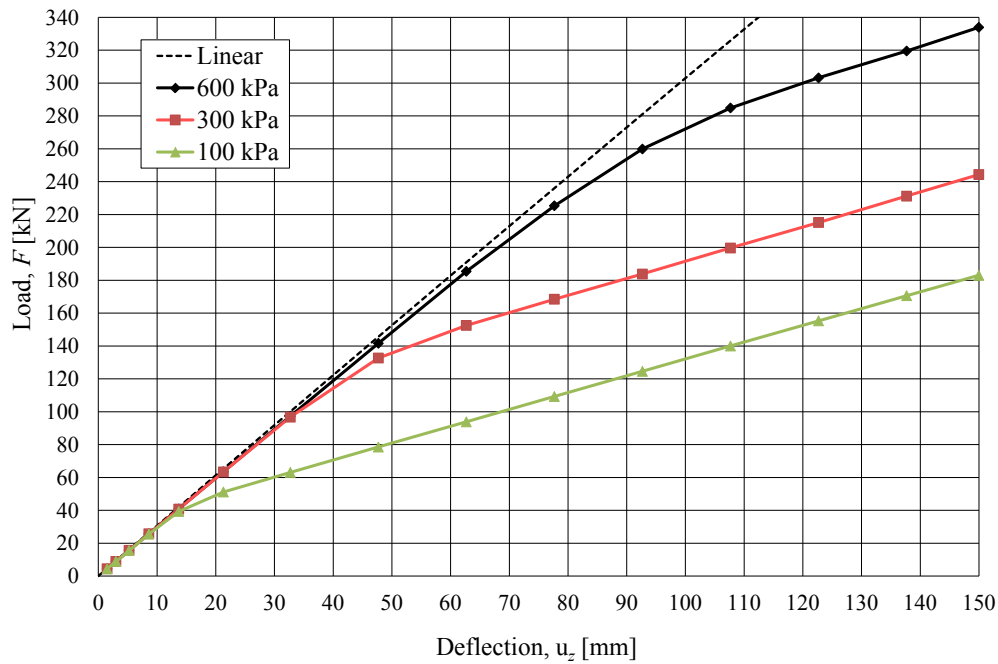


Figure 5.21 Load versus deflection for the different pre-stress levels.

Load and deflection results were normalized from analyses with time step increments set to distribute equally after normalization. This was done in order to get as similar results as possible by having the increments divided equally for all pre-stress levels. It can be observed that the overall behaviour when it comes to load-deflection is very similar for all levels, see Figure 5.22. The minor deviation for 600 kPa could be due to the multiple layers of numerical error margin tolerances when the solver is trying to obtain equilibrium.

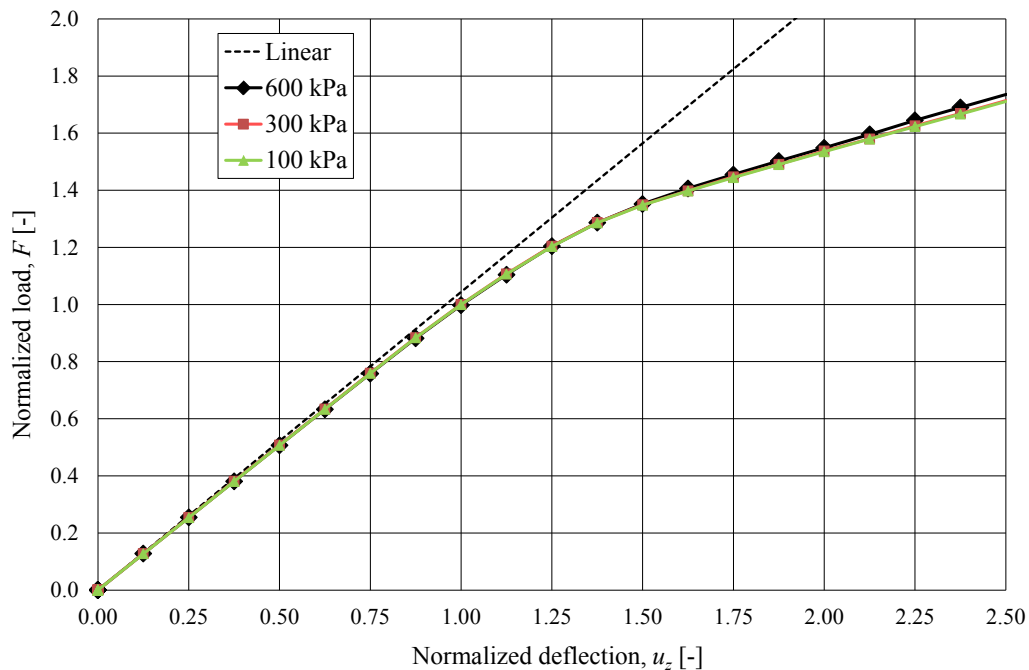


Figure 5.22 Normalized load-deflection curves for the three different pre-stress levels where 1 signifies the approximate point of irreversible slip initiation.

A node set was assigned to the model in order to be able to take out results at critical sections in a systematic manner, see Figure 5.23.

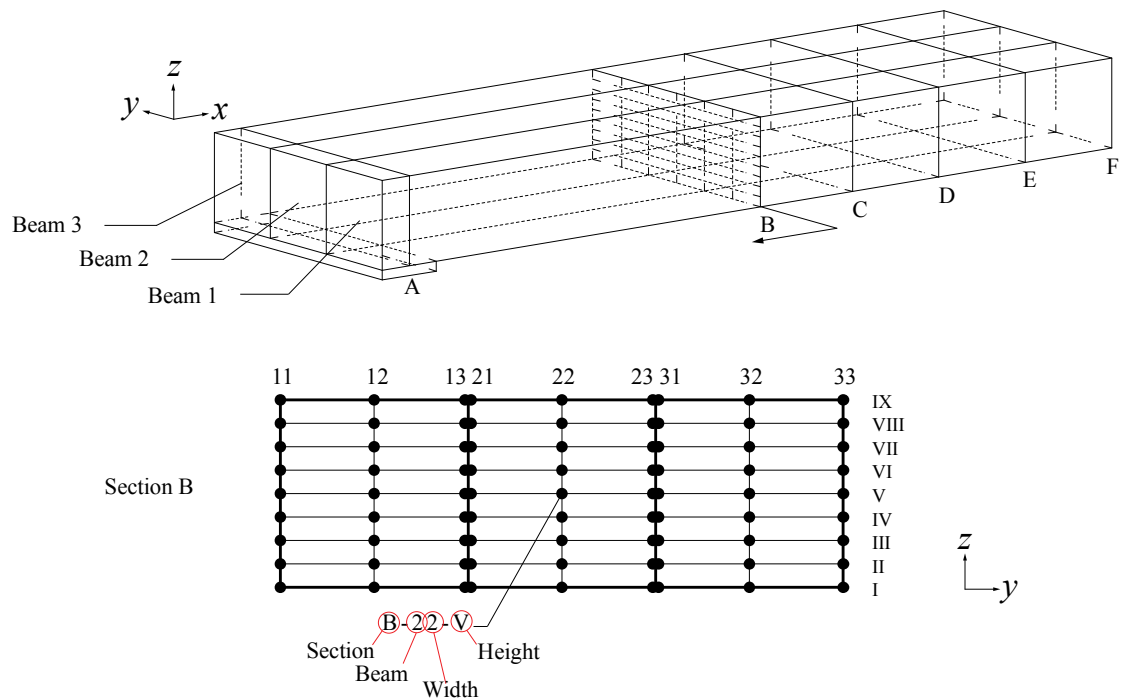
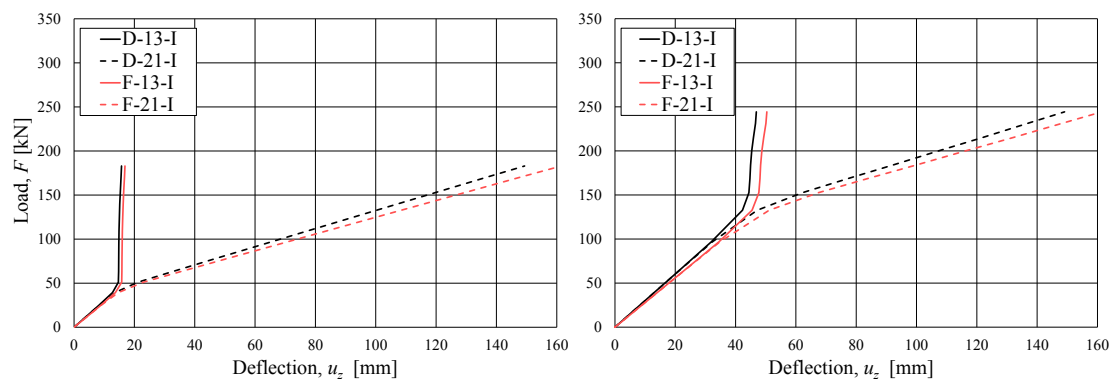


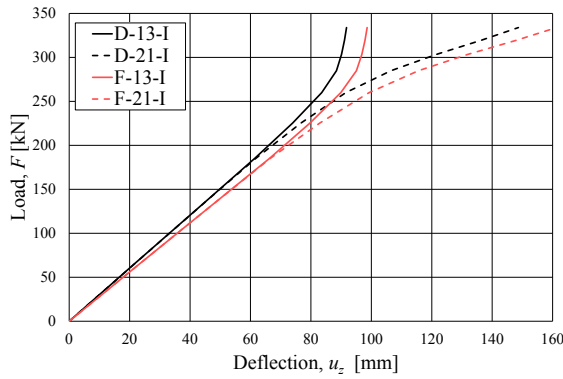
Figure 5.23 Definition of the node set names.

Load versus deflection was checked for an outer beam and the middle beam at two different sections of the deck, see Figure 5.24 (a)-(c). Two adjacent nodes on an outer and the middle beams were compared in order to observe the effect of pre-stress levels on the SLT deck. The load-deflection curve shows a linear behaviour until the middle beam starts slipping. The linear behaviour can be extended by increasing the pre-stress level on the deck. After the development of full slip the middle beam carry almost all the applied load which leads to a stiffness similar to that of a single beam for the deck. The outer beams stop taking any more load once the slip has developed fully. The deflection at section F, the mid-section of the deck, showed higher values than section D, as expected.



(a) 100 kPa pre-stress

(b) 300 kPa pre-stress

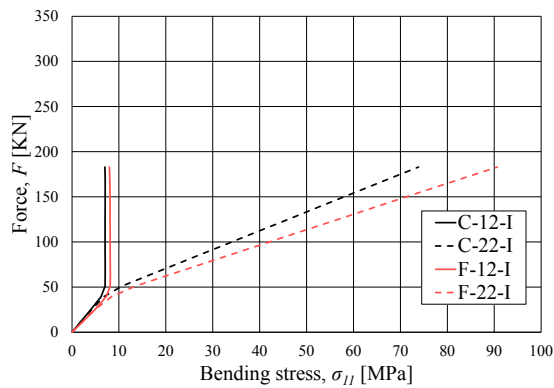


(c) 600 kPa pre-stress

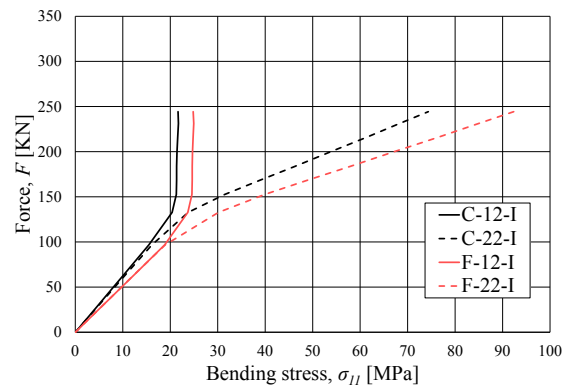
Figure 5.24 Load-deflection curves for different pre-stress levels and different nodes in the deck.

### 5.3.4.2 Longitudinal bending stress

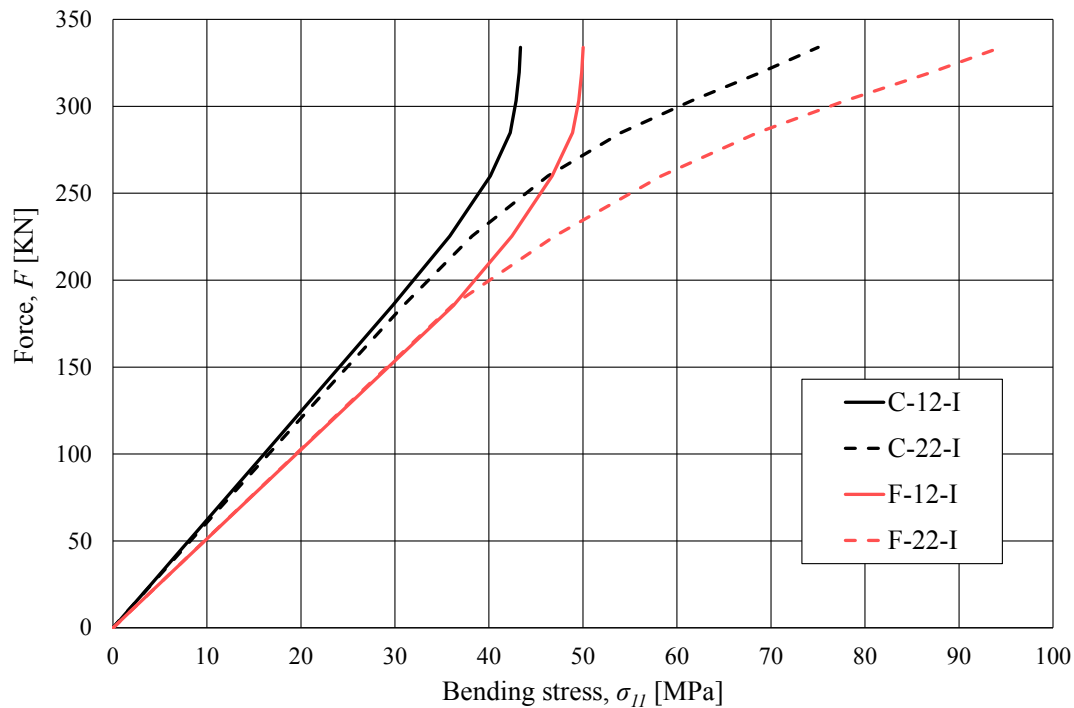
The influence of different pre-stress levels on bending stresses was examined by comparing the bending stress of two nodes from the bottom centre of the outer and middle beams, at different load levels and on different sections, see Figure 5.25 (a)-(c). The bending stresses on the outer and middle beam showed a linear behaviour until slipping starts between the beams. Once slip initiates, stress redistribution occurs which results in that the load is carried only by the middle beam. An increase in the pre-stress level extends the linear behaviour of the deck by delaying the slip between the beams.



(a) 100 kPa pre-stress



(b) 300 kPa pre-stress



(c) 600 kPa pre-stress

Figure 5.25 Load versus longitudinal bending stress for different pre-stress levels.

The values in Figure 5.25 were taken directly from Abaqus without any correction for the slight deviation, at most a 2.9 % underestimation, when taking data out from outer nodes as mentioned in Section 5.2.4.

### 5.3.4.3 Vertical shear stress between beams

The vertical shear stress is of key interest when examining vertical slip in an SLT deck. The propagation of the vertical shear stress and the resisting pressures are shown in Figure 5.26. The resisting pressure is calculated from the contact pressure multiplied with the coefficient of friction. Due to the transversal bending moment in the deck, the resisting pressure will have an inclined shape and the parabolic shape of the shear distribution will also be affected. After the vertical shear stress curve reaches the resisting curve an irreversible redistribution occurs which results in further vertical slipping in the interaction of the surfaces. Eventually the slipping surface will lose contact and all stresses in that area will become zero, see Figure 5.26 for 150 mm applied displacement. The interaction area is reduced when this occurs which leads to an increase of stress on the remaining area in contact. By increasing the pre-stress level the resisting pressure will be increased, which delays the vertical slip of the beam.

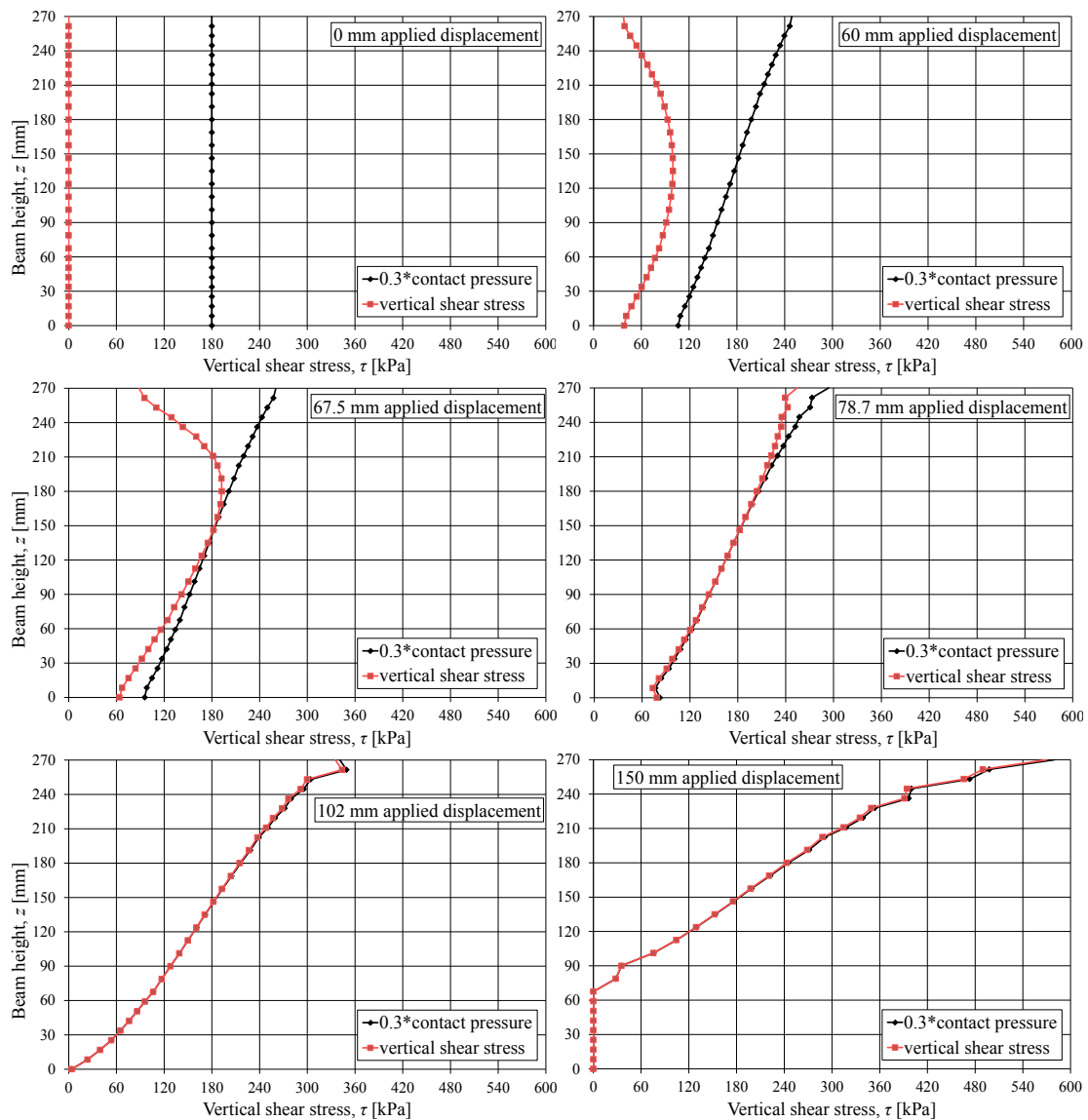


Figure 5.26 Development during loading of acting vertical shear stresses and resisting stresses at section B, the quarter-span of the beam, for 600 kPa of pre-stress.

#### 5.3.4.4 Horizontal shear stress between beams

The horizontal shear stress was also investigated before and after the middle beam starts slipping. The horizontal slip occurs when the horizontal shear stress reaches the resisting pressure. An increase in pre-stress level also delays the horizontal slip between the beams by increasing the resisting pressure. The propagation of the horizontal shear stresses and the resisting pressures are shown in Figure 5.27.

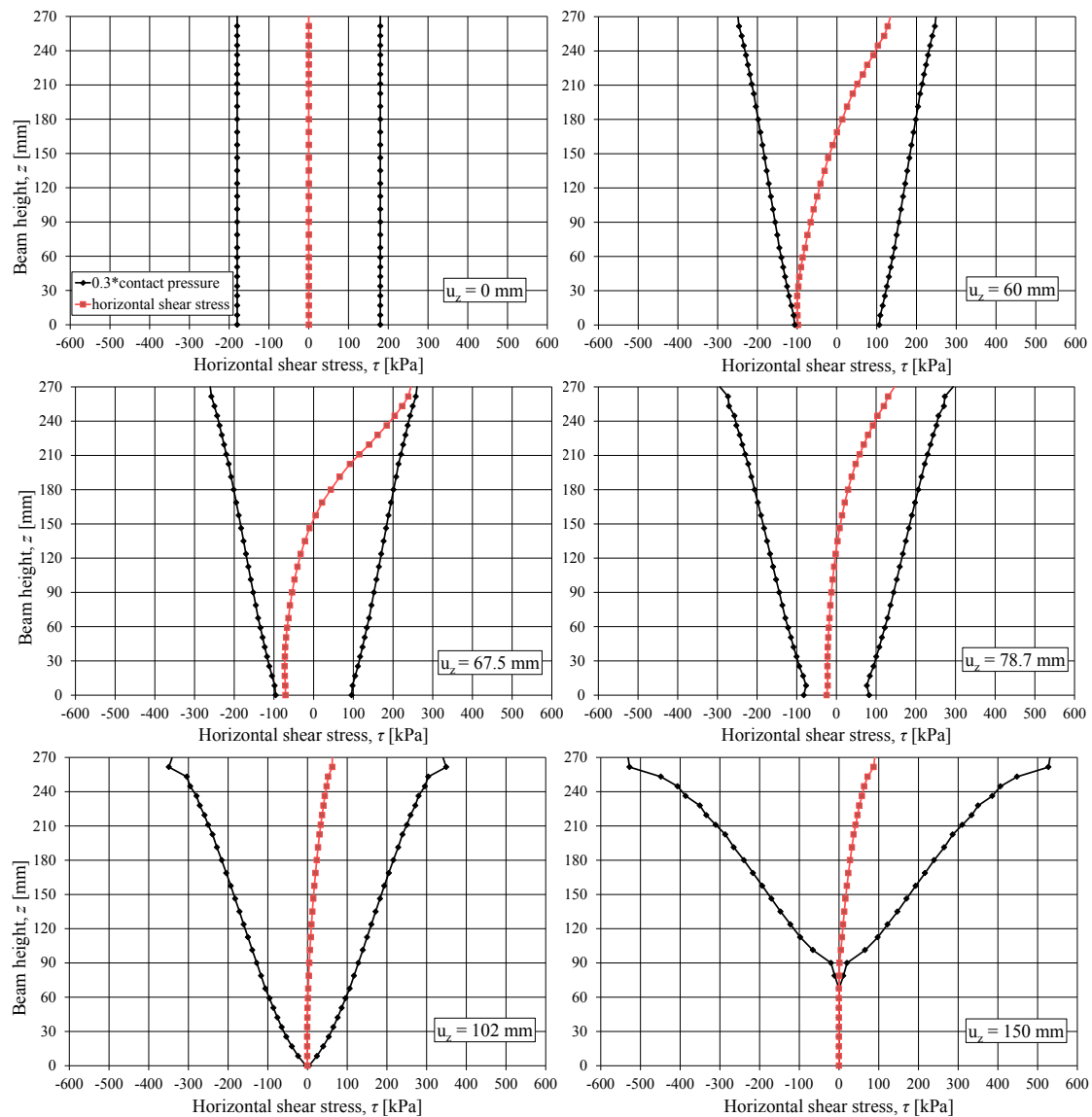


Figure 5.27 Development during loading of acting horizontal shear stresses and resisting stresses at section B, the quarter-span of the beam, for 600 kPa of pre-stress where  $u_z$  denotes the applied displacement.

The theoretical horizontal shear stress is linear which is not observed in Figure 5.27 because it has already redistributed along the height towards the parts where resistance is higher. When interlaminar slip has occurred the laminations lose contact which is why the stresses, which are taken along the height of the middle beam, are zero in the lower part when the applied displacement,  $u_z$ , exceeds 102 mm.

### 5.3.4.5 Reaction force

The reaction force at different load levels were taken from the outer (Beam 1) and middle (Beam 2) beams of the deck to investigate the influence of the pre-stress level on the distribution and development of the reaction force, see Figure 5.29. The notation used for the three beams is explained by Figure 5.28.

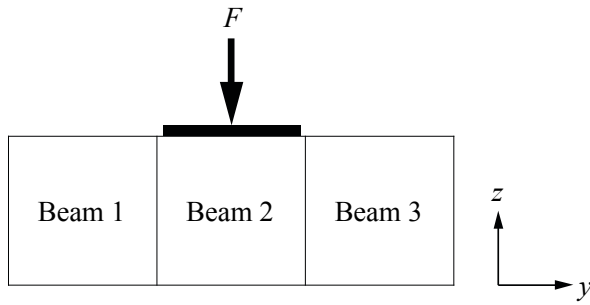


Figure 5.28 Section of the deck with the notation used for the three beams.

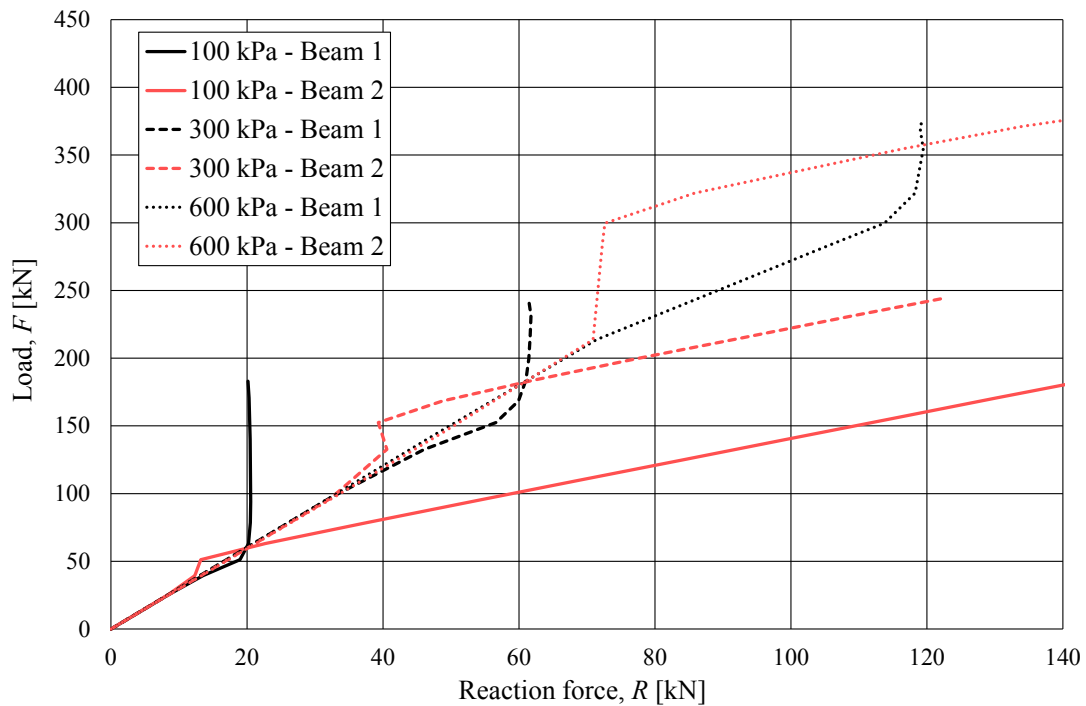


Figure 5.29 Reaction forces for outer and middle beams for different pre-stress levels.

When interlaminar slip is initiated and the applied load continues to increase, the reaction forces cease to increase linearly as seen in Figure 5.29. During a certain interval, reaction forces are concentrated to the outer beams (Beam 1 and Beam 3) before they are concentrated to the middle beam (Beam 2) exclusively. Normalization of the results in Figure 5.29 indicates that the behaviour is more or less identical for the different pre-stress levels. The reason why the loaded middle beam is unloaded at the support for this brief interval can be explained by Figure 5.30.

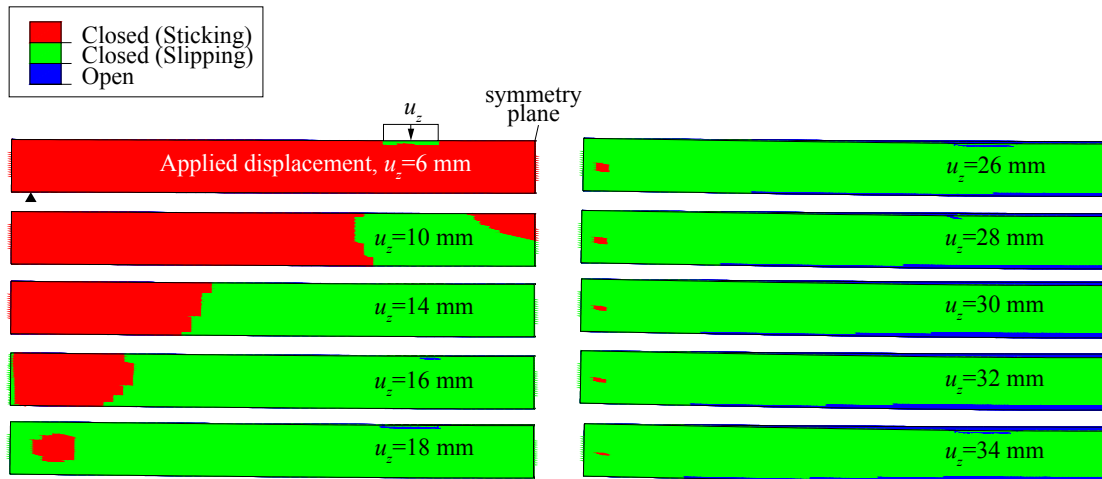


Figure 5.30 Contact status for a deck with a pre-stress level of 100 kPa showing the interlaminar slip propagation and a resulting centre of rotation for the middle beam.

When slip is initiated, the middle beam starts rotating in relation to the other beams and its centre of rotation is temporarily shifted from the support. This creates an upward force at the end which will have to be compensated by the outer beams in order to maintain vertical equilibrium.

The magnitude of vertical and horizontal slip can be seen in Figure 5.31. The vertical slip is the first to initiate in this case and propagates from underneath the loaded area. At 16 mm of applied displacement, vertical slip can be observed left of the support and the sticking area and horizontal slip has also initiated which implicates that the middle beam has begun to rotate in relation to the outer beams.

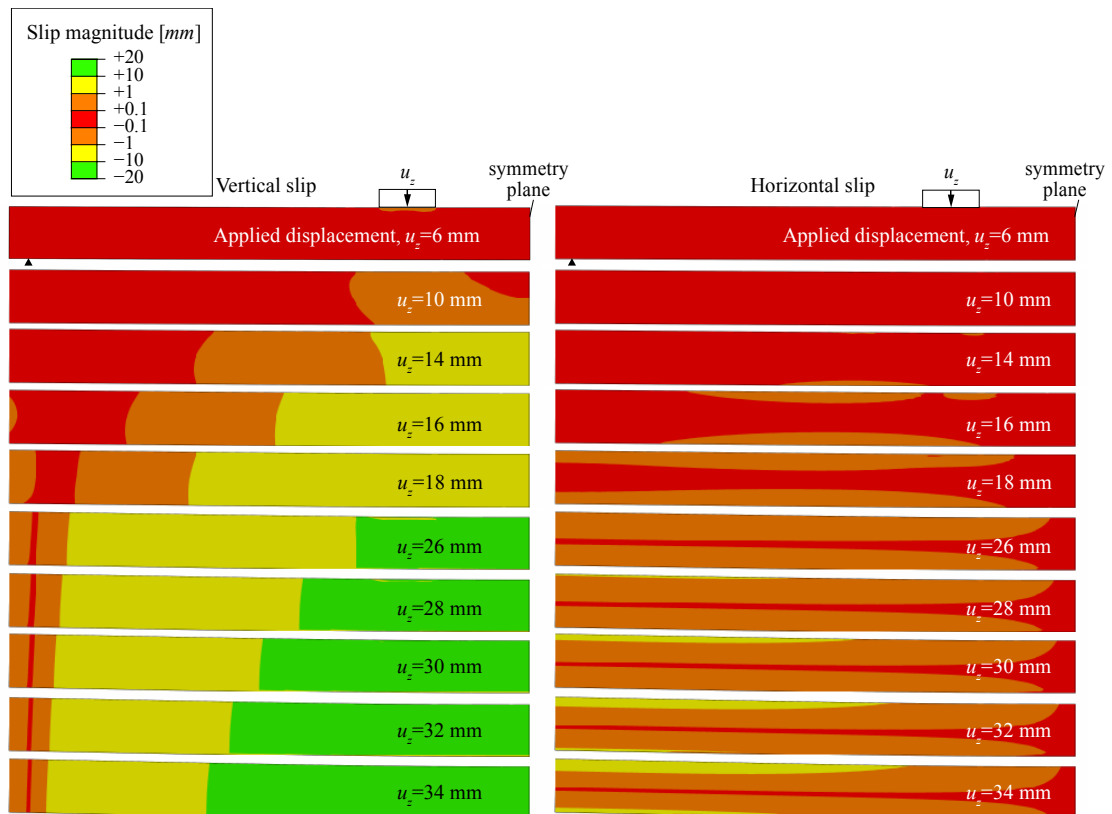


Figure 5.31 Development of vertical and horizontal slip with contour plot of magnitude for the same load levels as in Figure 5.30.

This rotation is continued until slip is propagated over the whole interaction surface which occurs around 35 mm of applied displacement correlating to a load level of just over 60 kN, which can be seen in Figure 5.32.

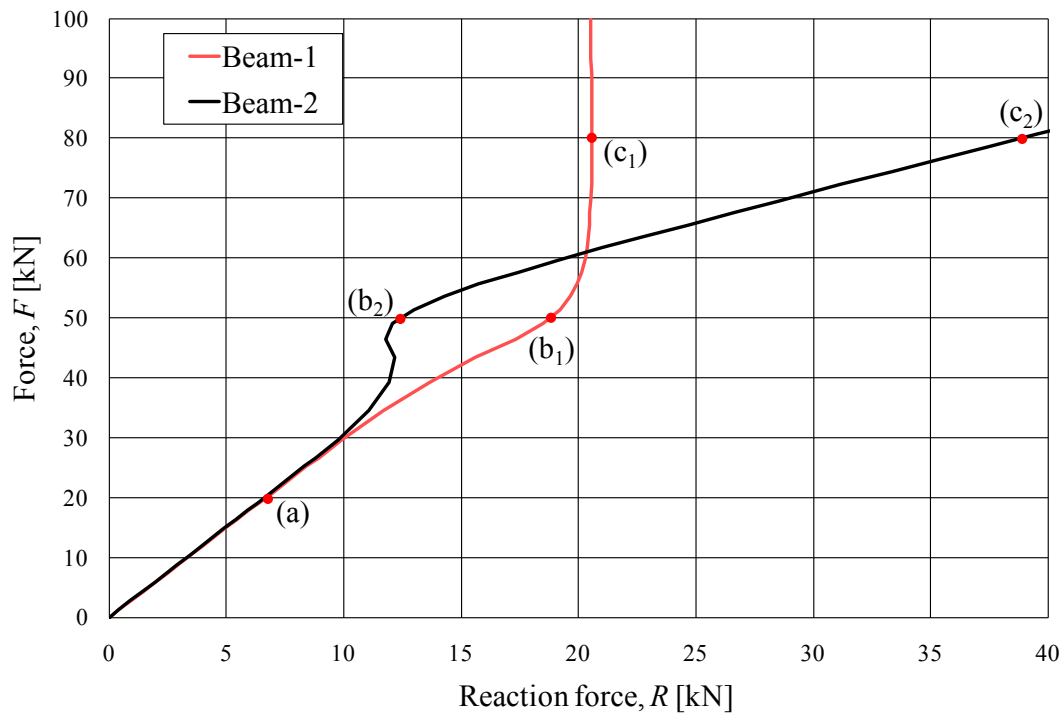


Figure 5.32 Development of reaction forces per beam for a deck with 100 kPa of pre-stress.

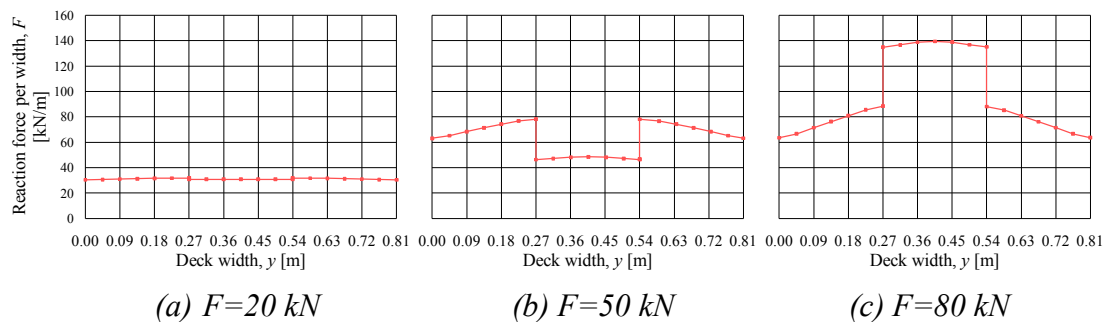


Figure 5.33 Reaction forces distribution along the support at different load level for 100 kPa of pre-stress.

Different reaction force distributions are shown at different load levels in Figure 5.33. The reaction force is distributed uniformly at lower load levels before it starts slipping, see Figure 5.33 (a). At a load level where the middle beam starts rotating in relation to the other beams and its centre of rotation is temporarily shifted from the support, the reaction force is reduced on the middle beam resulting in increased reaction forces for the outer beams, see Figure 5.33 (b). After full development of the slip, the additional load is taken by only the middle beam resulting in an increased reaction force of the middle beam, see Figure 5.33 (c).

### 5.3.5 Elastic slip

Different levels of elastic slip were introduced in the model with three beams to observe the influence on slip behaviour in an SLT deck. Different parametric comparisons were made for different elastic slips. Elastic slip of 0.1 mm and 5.0 mm were used for comparison in order to be able to observe the extreme effects.

#### 5.3.5.1 Beam deflection

Influence of elastic slip on a load-deflection curve was examined by considering two adjacent nodes on an outer and the middle beams, see Figure 5.34. It was observed that an increase in elastic slip leads to an earlier slip, the difference in the case shown here is not large though, creates early deviation of the two corresponding load-deflection curves.

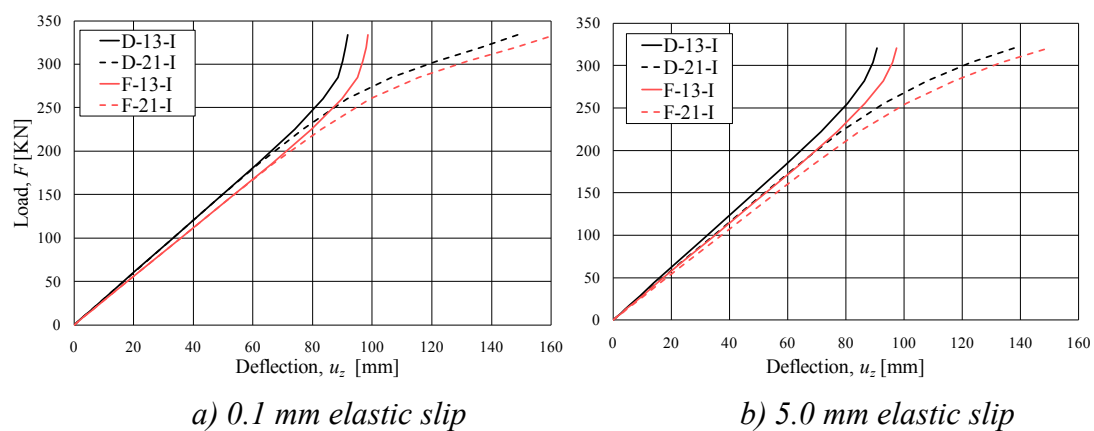


Figure 5.34 Load-deflection curve for different levels of elastic slip with 600 kPa pre-stress level.

#### 5.3.5.2 Longitudinal bending stress

The influence of elastic slip on bending stress was also examined by comparing the bending stresses of two nodes from the bottom centre of the outer and middle beams, at different load levels and in different sections, see Figure 5.35. It was observed that an increase of the elastic slip leads to an earlier slip which creates an earlier redistribution of bending stresses in the deck. However, the bending stress is not affected by elastic slip magnitude once the slip is fully developed.

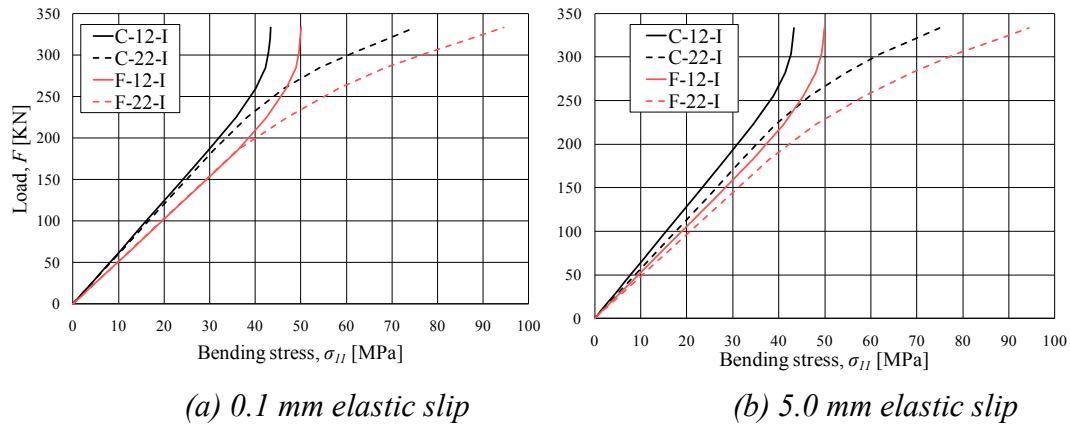


Figure 5.35 Load versus bending stress curve for different elastic slip for 600 kPa of pre-stress.

### 5.3.5.3 Vertical shear stress between beams

The vertical shear stress for different levels of elastic slip was investigated at different load levels, see Figure 5.36. Before the beams start slipping the vertical shear stress on the interface shows slightly higher values at the top and bottom part of the beam surface while the vertical shear stress shows lower value at the middle part of the beam surface for a higher level of elastic slip. On the other hand, the elastic slip has no significant influence on the vertical shear once the beams start slipping.

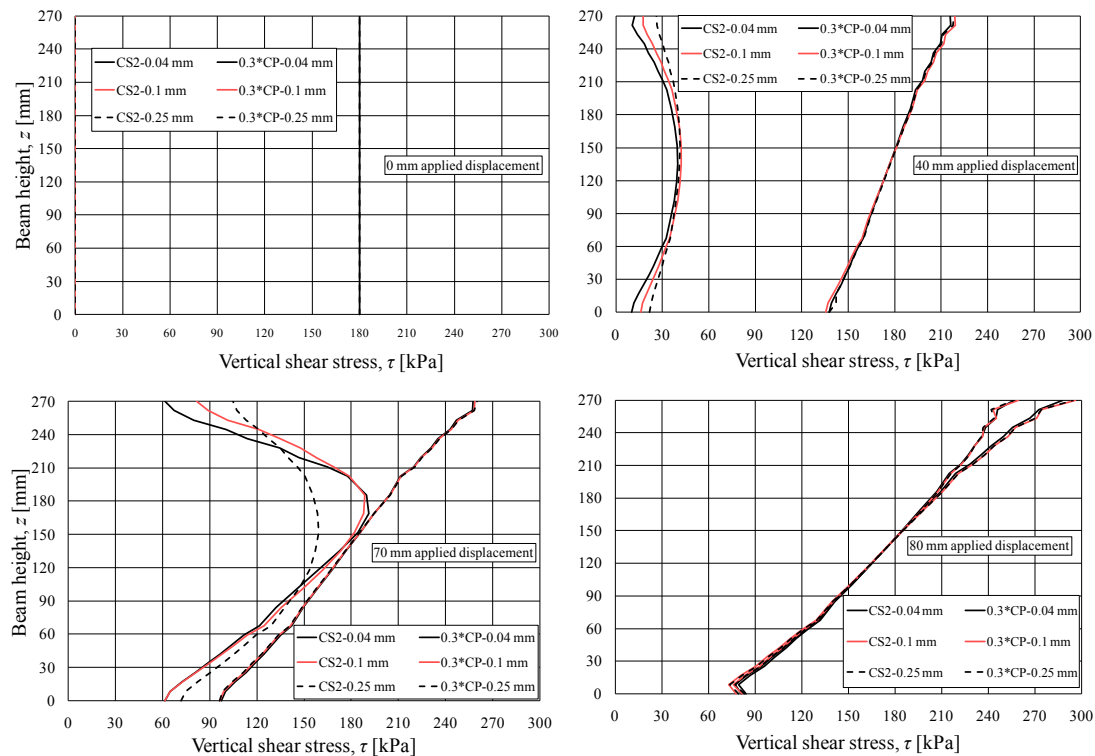


Figure 5.36 Illustration of vertical shear stress for different elastic slip at different load levels. The notations CS2 and CP signify vertical shear stress and contact pressure respectively.

### 5.3.5.4 Reaction force

The reaction force for the outer and middle beams were compared with different elastic slip values at different load levels as shown in Figure 5.37. The middle beam starts carrying a higher reaction force compared to the outer beams at an earlier stage for a higher elastic slip. This is due to the initiation of interlaminar slip at an early stage for a higher elastic slip.

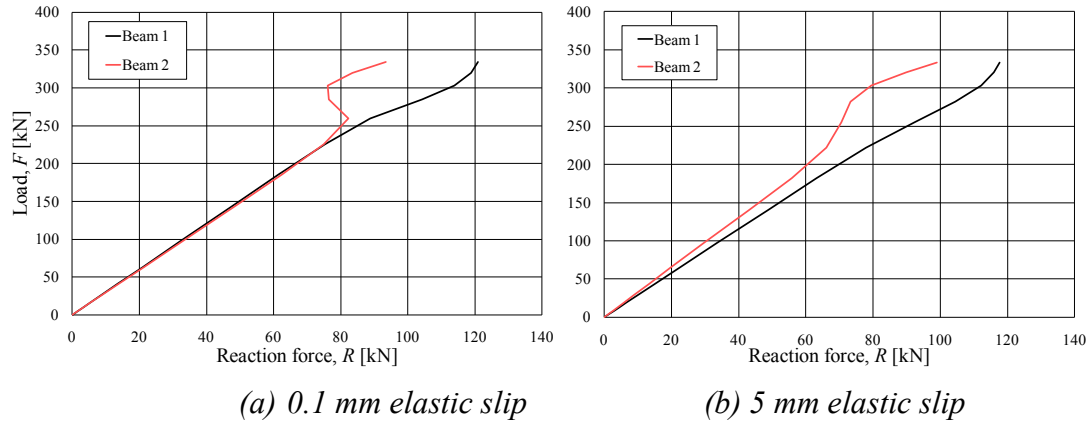


Figure 5.37 Reaction force development for two different levels of elastic slip for 600kPa pre-stress.

### 5.3.6 Modulus of elasticity in longitudinal direction

In reality the material properties of the beams in a stress-laminated timber deck can vary a great deal. To capture the effect of variation in material properties in an SLT deck, models were analysed with different material properties for different elements of the deck. Using the model with three beams, different combinations of moduli of elasticity were analysed. The different combinations are given in Table 5.2. The moduli of elasticity were chosen in order to be able to see the behaviour of the interlaminar slip in different combinations of weak and stiff laminations. The pre-stress level was set to 600 kPa for all analyses in this section.

Table 5.2 Combinations of different longitudinal moduli of elasticity.

Combination	Beam 1	Beam 2	Beam 3
1	$E_1$	$E_1$	$E_1$
2	$E_1$	$E_1$	$E_2$
3	$E_1$	$E_1$	$E_3$
4	$E_2$	$E_1$	$E_2$
5	$E_2$	$E_1$	$E_3$
6	$E_3$	$E_1$	$E_3$

Where:  $E_1 = 12.0 \text{ GPa}$ ,  $E_2 = 10.8 \text{ GPa}$ ,  $E_3 = 13.0 \text{ GPa}$

### 5.3.6.1 Beam deflection

Section D in Figure 5.23 was chosen in order to examine the effect of different combinations of moduli of elasticity on the deflection of the beams, see Figure 5.38. A middle beam combined with stiff outer beams resulted in less deflection. The outer beams with the lower stiffness displayed a higher level of deflection as expected.

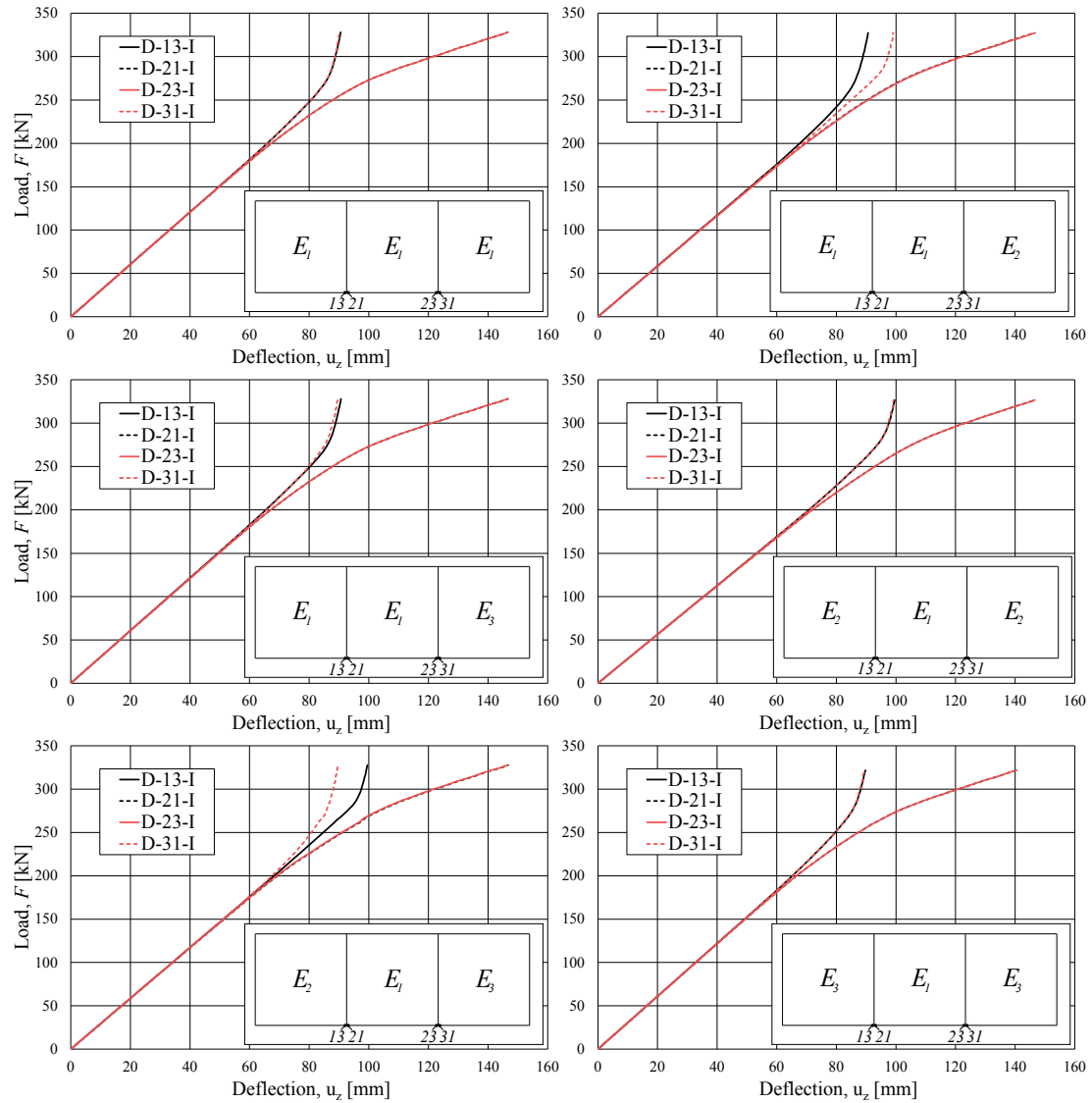


Figure 5.38 Load-deflection curves for the different combinations of moduli of elasticity, taken from section D in Figure 5.23.

### 5.3.6.2 Longitudinal bending stress

The bending stresses were examined for different beams with different modulus of elasticity combinations at different load levels, see Figure 5.39. A stiff outer beam takes more bending stress compared to a weak outer beam. Outer beams with the same modulus of elasticity have the same bending stress at different load levels. It was also observed in Table 5.3 that the bending stresses for different combinations of moduli of elasticity have no significant difference.

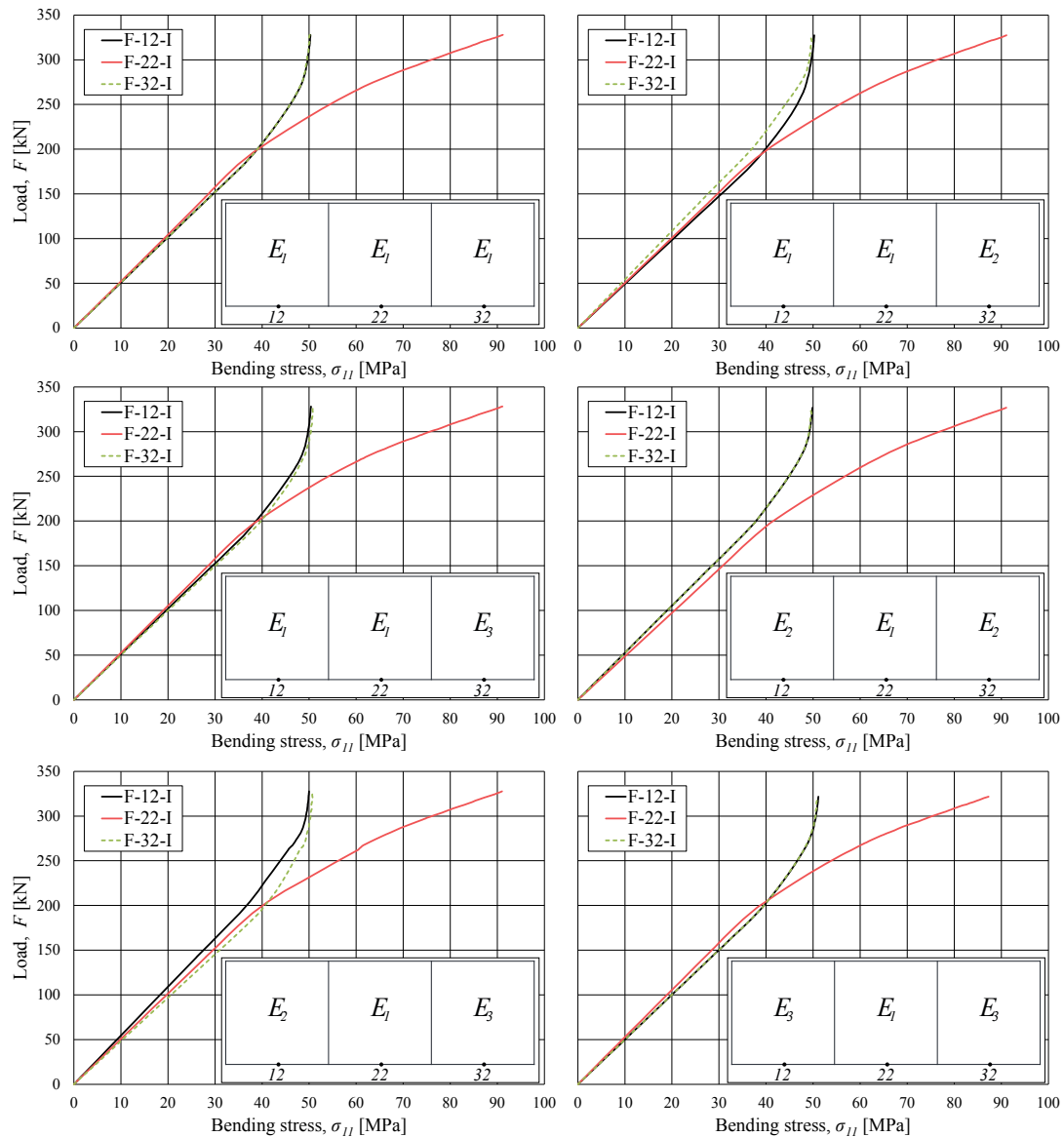


Figure 5.39 Bending stresses for the different combinations of moduli of elasticity for 600 kPa pre-stress in the beams at section F in Figure 5.23.

Table 5.3 *Bending stress at section F for various combinations of beams with different modulus of elasticity at different load level.*

	$u_z$ [mm]	$F$ [kN]	$\sigma_{x,12}$ [MPa]	$\sigma_{x,22}$ [MPa]	$\sigma_{x,32}$ [MPa]
$E_1, E_1, E_1$	50	145.9	28.8	27.8	28.8
	100	268.5	48.0	61.1	48.0
	150	328.0	50.3	91.2	50.3
$E_1, E_1, E_2$	50	141.1	28.7	27.9	25.9
	100	264.0	47.9	60.4	46.0
	150	327.4	50.2	91.1	49.7
$E_1, E_1, E_3$	50	146.5	28.8	27.8	29.3
	100	268.6	48.0	60.9	48.6
	150	328.2	50.4	91.1	50.9
$E_2, E_1, E_3$	50	141.8	26.0	27.9	29.3
	100	262.5	45.6	60.5	48.0
	150	327.6	49.9	91.0	50.9
$E_2, E_1, E_2$	50	136.5	25.9	28.0	25.9
	100	259.8	46.0	60.0	46.0
	150	326.8	49.8	91.0	49.7
$E_3, E_1, E_3$	50	147.2	29.4	27.9	29.4
	100	269.1	48.8	60.8	48.7
	150	328.5	51.2	91.0	51.1

### 5.3.6.3 Vertical shear stress between beams

The vertical shear stress for different combinations of modulus of elasticity was investigated to observe how it influences the slip initiation and where the first slip develops. For the given combinations, see Table 5.2, it was observed that the slip developed at different load levels depending on combination. Table 5.4 shows the load level at which the model with three beams starts slipping for different modulus of elasticity combinations. A deck with weaker outer beams gives the highest load at slip initiation. This is because the weaker outer beams deflect together with the middle beam with little resistance which delays the slipping phase. It is also shown by the large values of deflection in the outer beams.

Table 5.4 Load levels at slip initiation for different combinations of modulus of elasticity.

Combination	MoE	Applied displacement [mm]	Applied load [kN]
1	$E1, E1, E1$	68.7	209
2	$E1, E1, E2$	70.8	203
3	$E1, E1, E3$	70.8	210
4	$E2, E1, E2$	80.7	222
5	$E2, E1, E3$	70.9	204
6	$E3, E1, E3$	72.0	214

Figure 5.40 shows a vertical shear stress distribution and the resisting shear capacity for combination 1 with the same modulus of elasticity for all three beams. The slip develops at the same load level for both interfaces.

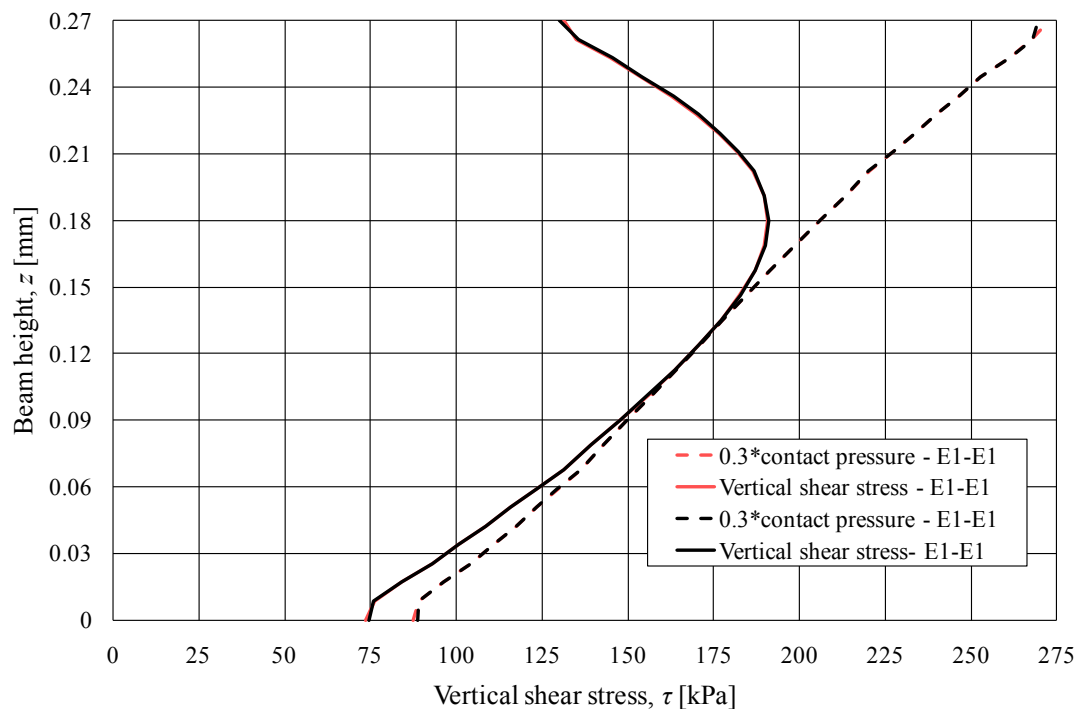


Figure 5.40 Point of slip initiation at 68.7 mm of applied displacement for combination 1 –  $E1, E1, E1$ .

Figure 5.41 shows a vertical shear stress distribution and the resisting shear capacity for combination 2 with a weaker modulus of elasticity for beam 3. The first slip develops at the interface between the two beams with the same modulus of elasticity, beam 1 and beam 2. This is because the stiffer outer beam is resisting more to stay in its original position when the middle beam deflect, while the less stiff outer beam resists less and is consequently more prone to follow the deflection of the middle beam.

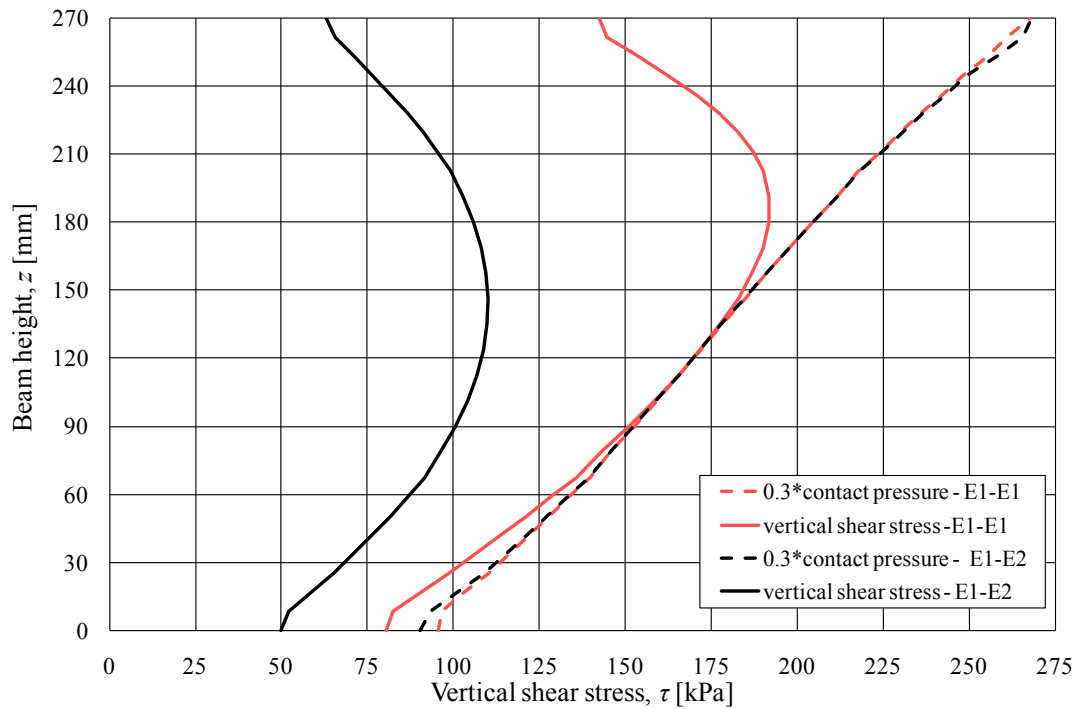


Figure 5.41 Point of slip initiation at 70.8 mm of applied displacement for combination 2 – E1, E1, E2.

Figure 5.42 shows a vertical shear stress distribution and the resisting shear capacity for combination 3 with a higher modulus of elasticity for beam 3. The slip develops at the same load level for both interfaces.

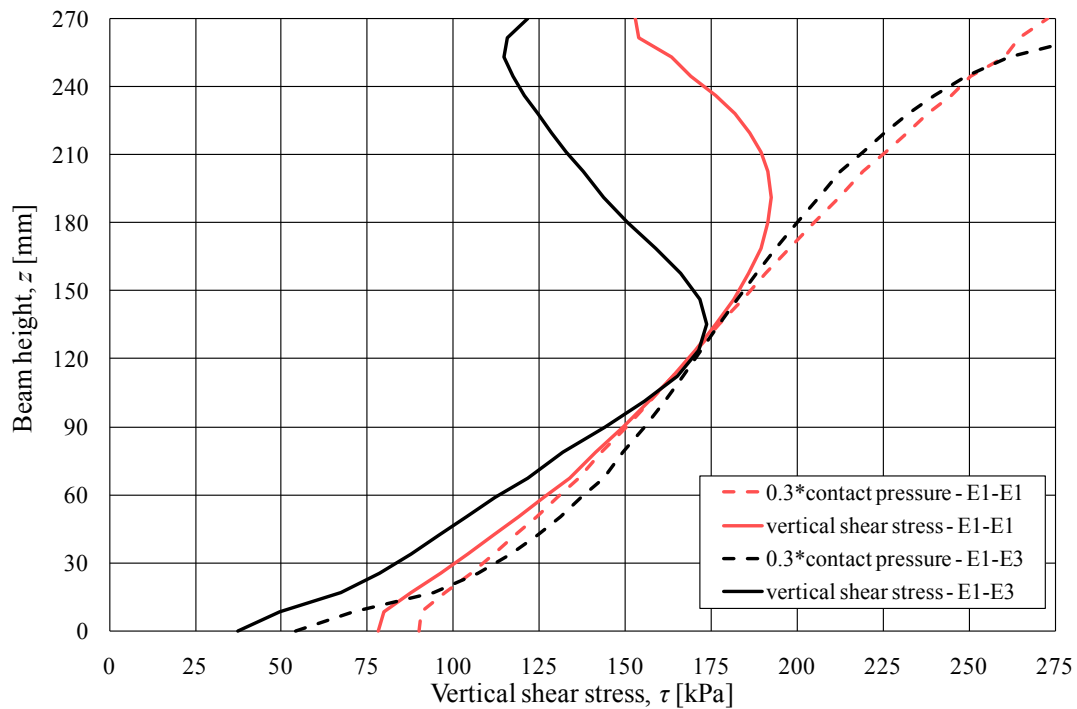


Figure 5.42 Point of slip initiation at 70.8 mm of applied displacement for combination 3 – E1, E1, E3.

Figure 5.43 shows a vertical shear stress distribution and the resisting shear capacity for combination 4 with a weaker modulus of elasticity for beams 1 and 3. The slip develops at the same load level for both interfaces and shows similarities to combination 1.

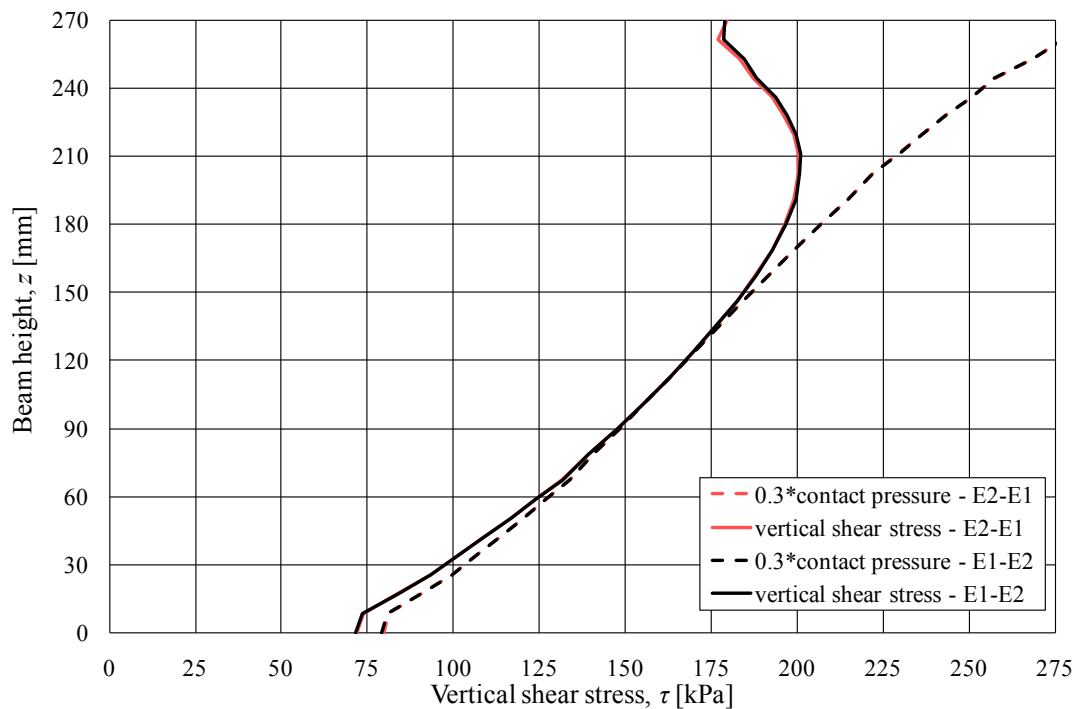


Figure 5.43 Point of slip initiation at 80.7 mm of applied displacement for combination 4 – E2, E1, E2.

Figure 5.44 shows a vertical shear stress distribution and the resisting shear capacity for combination 5 with a lower modulus of elasticity for beam 1 and higher modulus of elasticity for beam 3. The first slip develops at the interface between beams 2 and 3. This is because the stiffer beam is resisting the deflection of the middle beam.

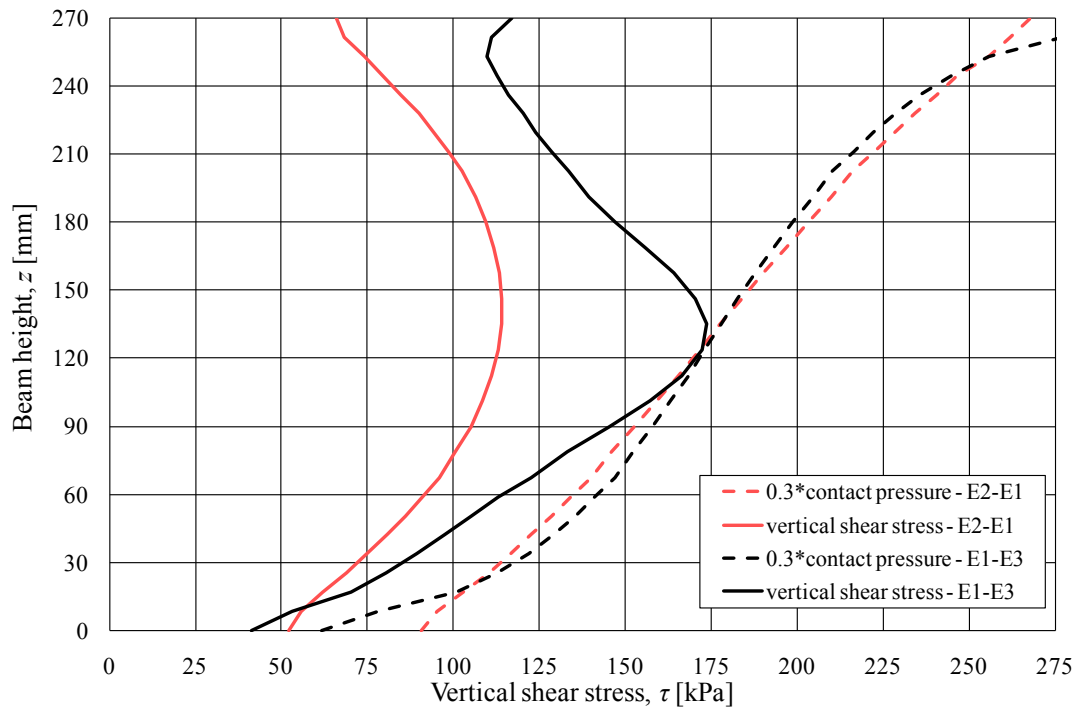


Figure 5.44 Point of slip initiation at 70.9 mm of applied displacement for combination 5 – E2, E1, E3.

Figure 5.45 shows a vertical shear stress distribution and the resisting shear capacity for combination 6 with a higher modulus of elasticity for the outer beams. The slip develops at both interfaces at the same load level similarly to combinations 1 and 4.

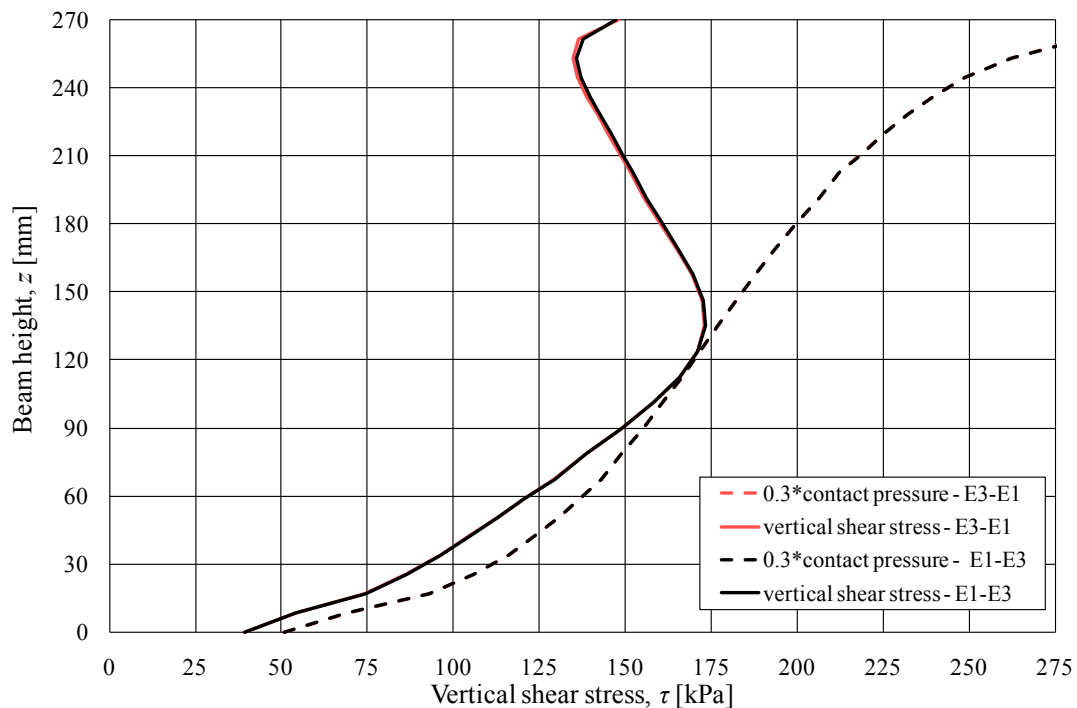


Figure 5.45 Point of slip initiation at 72.0 mm of applied displacement for combination 6 – E3, E1, E3.

### 5.3.6.4 Horizontal shear stress between beams

The horizontal shear stress for different combinations of moduli of elasticity was examined to observe how it influences the slip initiation and where the first horizontal slip develops. A typical example of the horizontal shear stress distribution along the height is shown for combination 5 with both weak and stiff beams in Figure 5.46. The first horizontal slip develops at the interface between beam 2 and beam 3. This is because the stiffer beam tries to stay in its original position when the middle beam is deflecting.

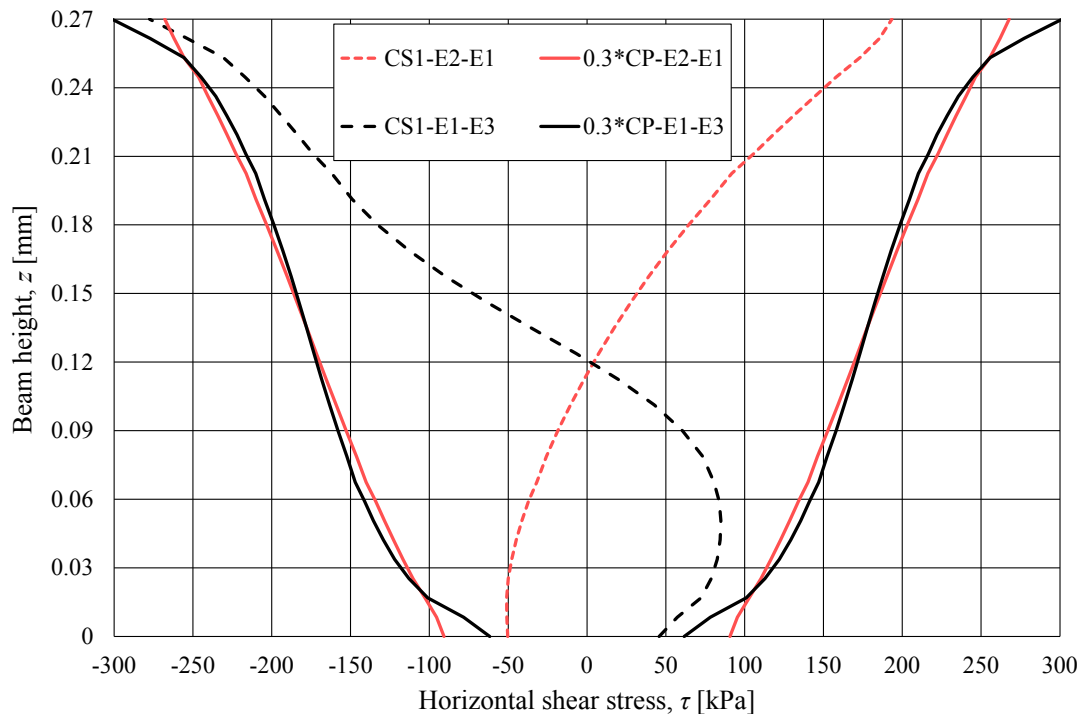


Figure 5.46 Horizontal shear stress distribution for different combinations of modulus of elasticity,  $E_2$ ,  $E_1$ ,  $E_3$ . The notations CS1 and CP signify horizontal shear stress and contact pressure respectively.

### 5.3.6.5 Reaction force

Reaction forces were examined for the different moduli of elasticity combinations. The overall behaviour during the loading phase was in all combinations similar to the case with three equally stiff beams displayed in Figure 5.29.

The distribution of reaction forces in transversal direction for combination 5, including all the stiffness variations can be seen in Figure 5.47.

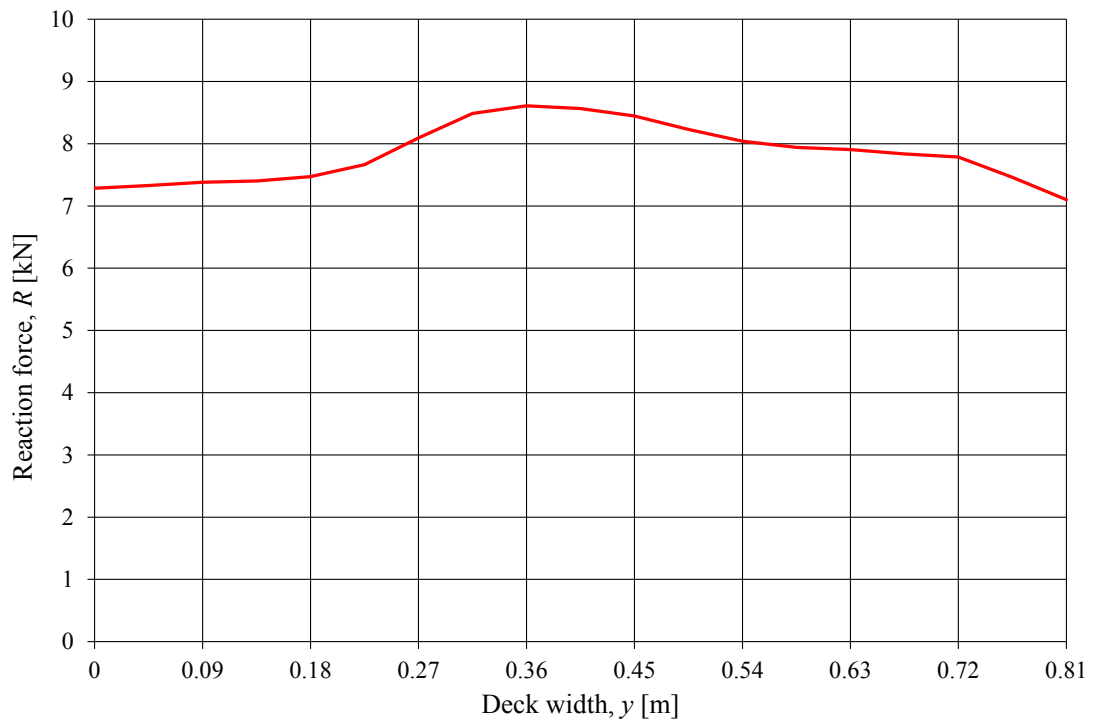


Figure 5.47 *Transversal distribution of reaction force under the support plate for combination 5, E2, E1, E3 taken at 50 mm applied displacement or 141 kN of applied load.*

## 6 Model 3 – Full-scale SLT deck

In order to be able to see how well the actual behaviour of an SLT deck can be simulated, a full-scale model was performed. A nine beam model with the actual measured material properties were analysed to compare the FE model with the laboratory test. This model was analysed using the background from chapter 5. In order to simulate the experimental test as thorough as possible, though, the supporting steel plate and loading plate were included in the model by giving an interaction property for the contacting surfaces with the SLT deck.

### 6.1 Material properties

The material properties from the laboratory test were assigned for all specific laminations, see Table 6.1 and Table 6.2. Longitudinal modulus of elasticity was given from test and other parameters were calculated based on EN 1995-2 (2004) as discussed in Section 3.3. The Poisson ratio was set to zero in order to simplify the analysis as it has no significant influence for this type of analysis. Two specimens were chosen to compare with the FE models. Three tests were made using specimen 1 with pre-stress level of 100 kPa, 200 kPa and 300 kPa and specimen 2 was used for testing a pre-stress level of 600 kPa.

Table 6.1 Material properties for specimen 1

Lamination	$E_{11}$ [MPa]	$E_{22}$ [MPa]	$E_{33}$ [MPa]	$G_{12}$ [MPa]	$G_{13}$ [MPa]	$G_{23}$ [MPa]	Density [kg/m <sup>3</sup> ]
1	11639	233	233	698	698	70	467
2	12897	258	258	774	774	77	483
3	13221	264	264	793	793	79	483
4	13125	263	263	788	788	79	483
5	14397	288	288	864	864	86	499
6	13061	261	261	784	784	78	499
7	11771	235	235	706	706	71	467
8	12878	258	258	773	773	77	467
9	12480	250	250	749	749	75	467

Table 6.2 Material properties for specimen 2

Lamination	$E_{11}$ [MPa]	$E_{22}$ [MPa]	$E_{33}$ [MPa]	$G_{12}$ [MPa]	$G_{13}$ [MPa]	$G_{23}$ [MPa]	Density [kg/m <sup>3</sup> ]
1	13386	268	268	803	803	80	483
2	12526	251	251	752	752	75	483
3	12547	251	251	753	753	75	475
4	13136	263	263	788	788	79	483
5	12991	260	260	779	779	78	483
6	12436	249	249	746	746	75	483
7	12260	245	245	736	736	74	483
8	12485	250	250	749	749	75	483
9	12981	260	260	779	779	78	499

Penalty friction formulation was used with anisotropic frictional behaviour for contacting surfaces between the laminations. The coefficients of friction used were 0.29 along the length of the deck,  $\mu_{\text{parallel}}$ , and 0.34 in the perpendicular direction,  $\mu_{\text{perpendicular}}$ , with an elastic slip of 0.1 mm. The coefficient of friction was taken as mean values from SP Trätek frictional test.

## 6.2 Boundary condition and load application

To simplify the analysis a symmetry boundary condition was assigned at mid-section of the deck length by setting  $u_x$  to zero, see Figure 6.1. On the left part of the model, the boundary was assigned on the bottom part of the steel plate on one line nodes by setting  $u_z$  to zero and  $u_y$  was set to zero at middle node of the bottom of the plate.

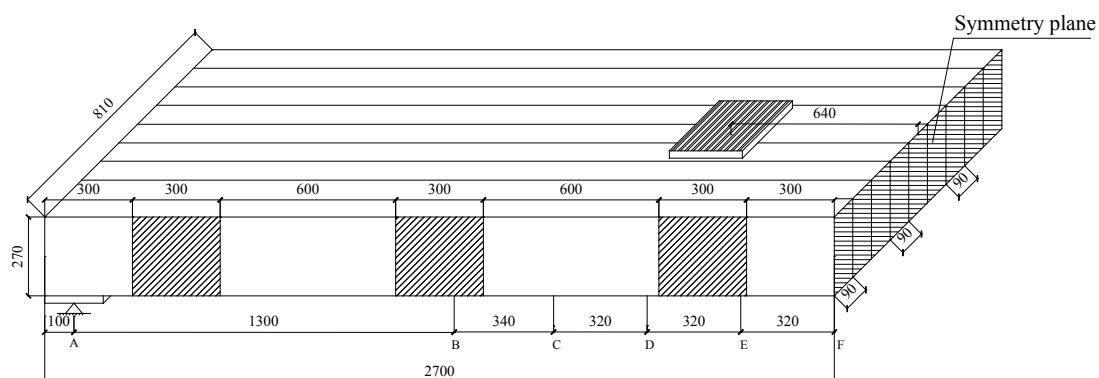


Figure 6.1 Illustration of full-scale model, dimensions in mm.

To restrain the uplift of the outer beams when the loaded part starts slipping it is important to include the self-weight, and consequently, the self-weight of the deck was introduced in the model as a gravity load. However, comparing the test result with the FE model the self-weight should be removed in order to get accurate results.

The pre-stress pressure was applied locally in the outer lamination surfaces in order to simulate the actual pre-stressing condition. Four models were analysed for different pre-stress levels, 100 kPa, 200 kPa, 300 kPa and 600 kPa, to compare with the full-scale test results.

Displacement control method was used as a load application method for the analysis, where a uniform displacement was prescribed at the mid-section of the loading plate.

### 6.3 Mesh

The mesh size used for the Full-scale laminations was based on the one beam mesh comparison in section 5.2 and from the mesh comparison for pre-stress distribution. The mesh for one beam in the stress laminated deck is illustrated in Figure 6.2.

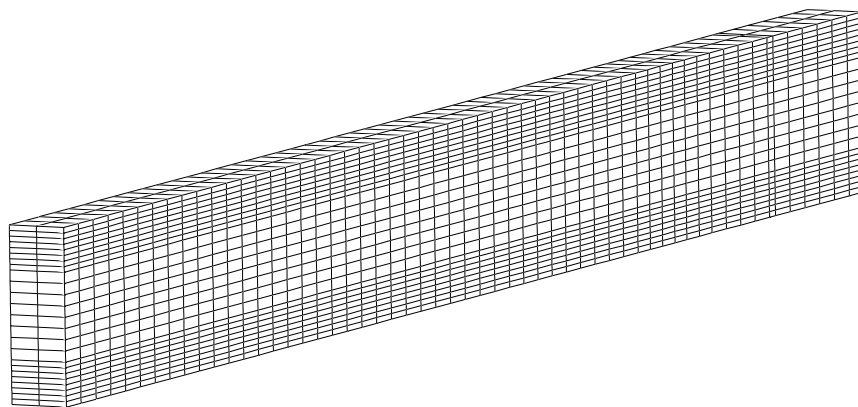
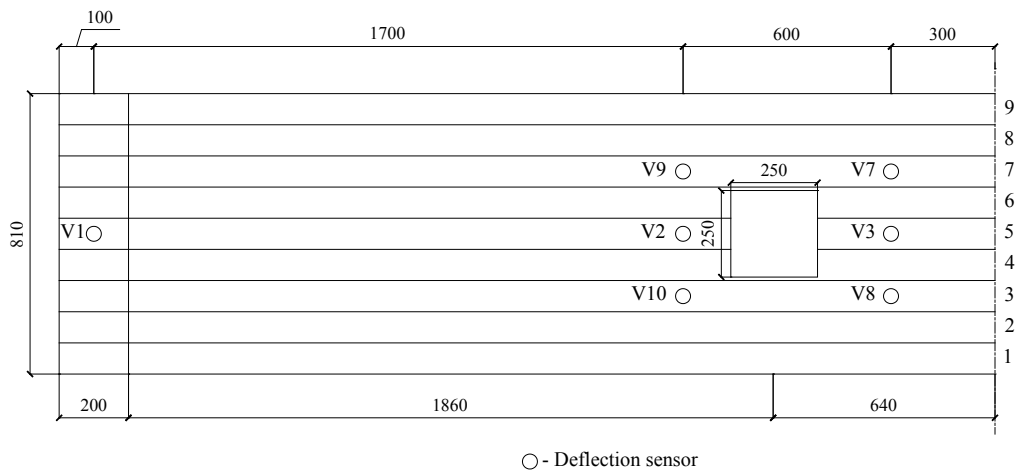


Figure 6.2 Mesh layout for one of the laminations.

### 6.4 Results

The finite element results were compared with the experimental test results to determine how well the finite element model captures the behaviour of the SLT deck when loaded until failure. The test results were taken out from several sensors measuring the deflection of the timber deck.

The points where the results for both the experimental test and finite element model were taken are shown in Figure 6.3. The sensors in the experimental test registered the vertical deformation on top of the SLT deck while the deck was loaded, see Figure 5.4.



*Figure 6.3 Arrangement of sensors in the experimental test for measurement of deflection, dimensions in mm.*



*Figure 6.4 Close-up of sensors and load plate on one of the narrow SLT deck specimens, clearly displaying interlaminar slip in laboratory tests by Ekholm (2012).*

## 100 kPa pre-stress level

A comparison between the results from the FE models and experimental tests were made at six different points of the SLT deck according to Figure 6.3. The results for a pre-stress level of 100 kPa are shown in Figure 6.5. A good correlation between the FE results and lab test was observed for both the loading and unloading portions of the graphs. The non-linear portion of the load-deflection curve starts at an early stage for pre-stress level 100 kPa which results in a difference between the load-deflection curves for the outer and middle sensors as discussed in Section 5.3.4.

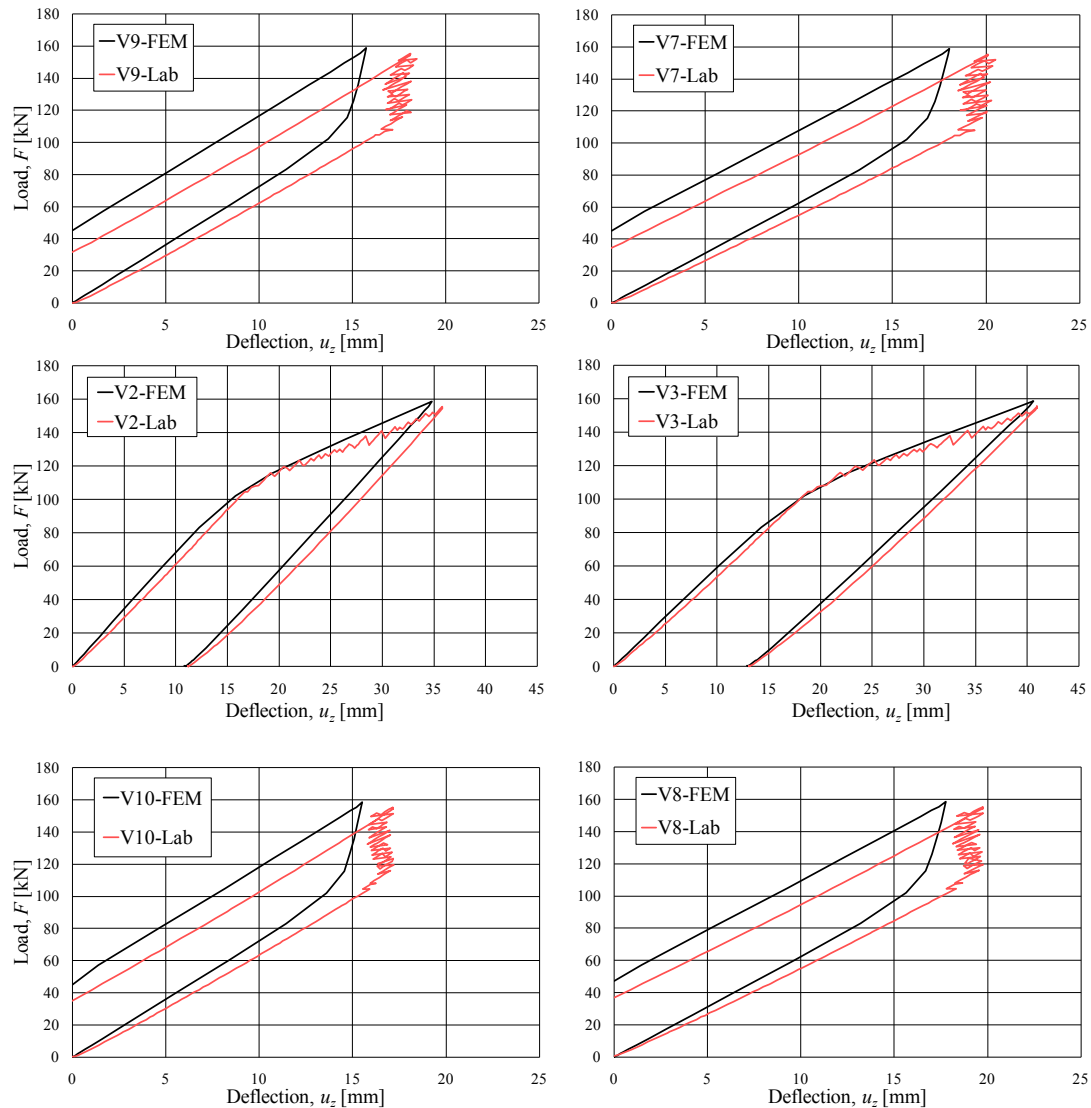


Figure 6.5 Comparison of load-deflection curves between FE model and lab test at 100 kPa of pre-stress.

## 200 kPa pre-stress level

The results for a pre-stress level of 200 kPa are shown in Figure 6.6. A good correlation between the FE results and lab test was observed for both the loading and the unloading portions of the graphs. Due to a higher pre-stress level, 200 kPa, compared to 100 kPa pre-stressing, the remaining deflection on the deck after unloading was smaller as the irreversible deformation was reduced, despite higher load levels.

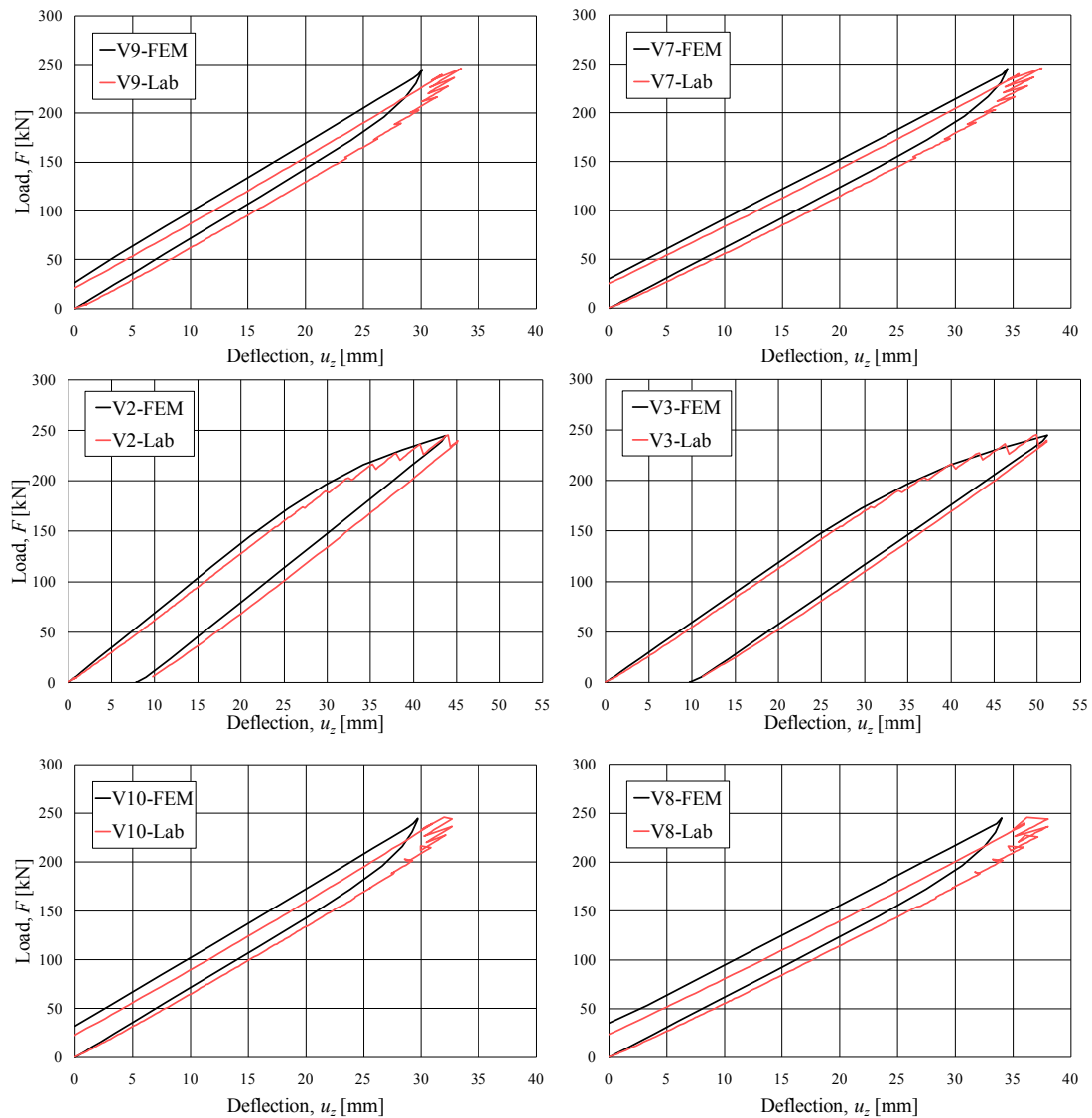


Figure 6.6 Comparison of load-deflection curves between FE model and lab test at 200 kPa of pre-stress.

### 300 kPa pre-stress level

The results for a pre-stress level of 300 kPa are shown in Figure 6.7. This test was performed by loading the specimen until failure. A good correlation between the FE and lab test results was observed.

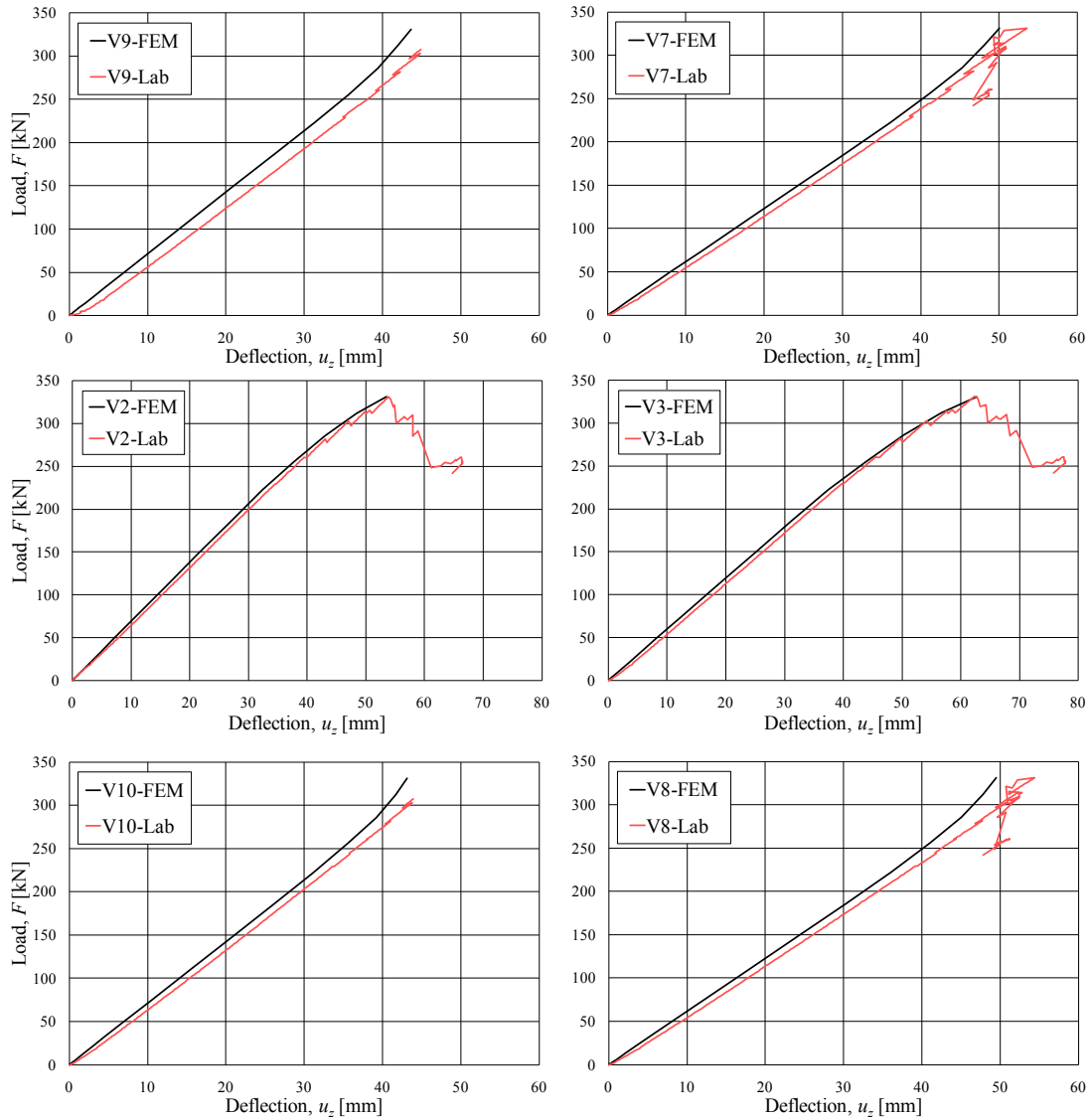


Figure 6.7 Comparison of load-deflection curves between FE model and lab test at 300 kPa of pre-stress.

### 600 kPa pre-stress level

The results for a pre-stress level of 600 kPa are shown in Figure 6.8. A good correlation between the FE and lab test results was observed. The higher pre-stress level maintains the linear behaviour and results in similar load-deflection curves for both outer and middle beams at higher load levels. The abrupt change in the load-deflection curve in the lab test was due to a local failure of the deck resulting in stiffness reduction of the structure.

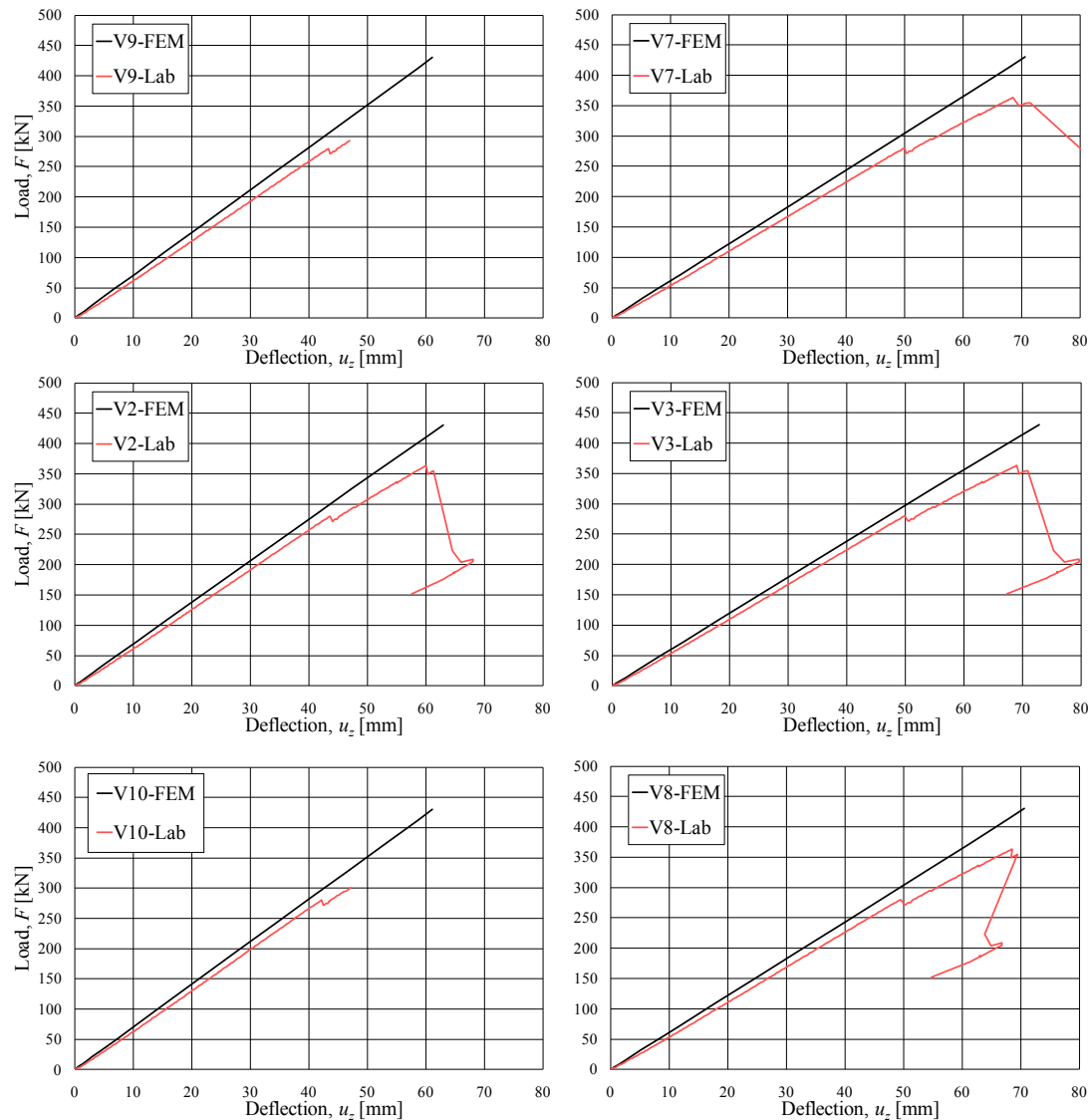


Figure 6.8 Comparison of load-deflection curves between FE model and lab test at 600 kPa of pre-stress.

## 7 Discussion

In this section the results found in chapter 4-6 are discussed. Analyses of three types of models were performed in order to observe the influence of different parameters in SLT decks.

### 7.1 Box on a plane

A simplified model was studied to gain knowledge of how to model friction and what parameters affect friction modelling with finite elements using Abaqus. There are different parameters that need to be set properly in order to get reasonable results for the friction behaviour in Abaqus. It was observed that the most important parameters were mesh size, time step and method of load application.

#### Mesh

It was observed that using locally increased mesh density on a region where there is stress concentration showed better results compared to a fully dense or coarse mesh when both computational time and the accuracy of the results are taken into consideration.

#### Time step

Depending on what parameters are to be studied the significance of the time step resolution varies. It may however be difficult to specify the time stepping which yields the exact real solution for complicated contact problems. Therefore using small time increments might provide better approximations but at the cost of longer computational time.

#### Load application

There are different ways to apply the load in a finite element model. Displacement-controlled load application was chosen to capture the non-linear behaviour at higher load levels. However, depending on its boundaries a uniform displacement does not necessarily equal a uniform load. It was observed that applying a uniform displacement on the surface of the box does not give the same result as applying a uniform pressure on the surface.

### 7.2 Model with three beams

Before the full-scale model was analysed, a simplification of the model was made by replacing the nine beams with three beams to reduce computational time and to make parametric studies.

#### Pre-stressing type

Two type of pre-stressing were examined by using uniformly distributed pressure applied along the full length of the beam and pressure applied in the local areas corresponding to the anchorage plates. It was observed that the two different models show significant difference in the pre-stress distribution. It is recommended to use locally applied pre-stress for the purpose of obtaining results that correspond to the real pre-stressing situation.

### **Pre-stress level**

An increase in pre-stress level increases the shear resistance which delays the slip of the laminations and extends the linear behaviour of the deck. Lower pre-stress levels showed an earlier slip initiation resulting in stress redistribution that creates a non-linear behaviour for the deck.

### **Elastic slip**

It was observed that an increase in elastic slip leads to an earlier slip which creates an earlier stress redistribution in the deck. For an elastic slip between 0.1 mm to 1.0 mm, no significant influence on the pre-stress distribution was observed.

### **Combination of different moduli of elasticity**

In reality the material properties of the beams in a stress-laminated timber deck varies a lot. To capture the effect of variation in material properties in an SLT deck, models were analysed with different material properties for different elements of the deck. Depending on the stiffness level each lamination assigned, the results showed that there were differences in the outputs across the sections.

## **7.3 Full-scale model**

A full-scale model was performed with nine beams and the actual measured material properties in order to observe how well the behaviour of the actual SLT deck specimens can be simulated using the methodology described in chapter 5. The comparison between the FE models with the lab test showed that it is possible to get accurate results using this type of modelling technique. Furthermore, simplifying the structure from the experimental tests by modelling the nine laminations as three beams was proven to be a good approximation concerning predictions of load-deflection behaviour, as can be seen in Figure 7.1. This modelling technique can be used to better understand how the distribution of load in transversal direction works.

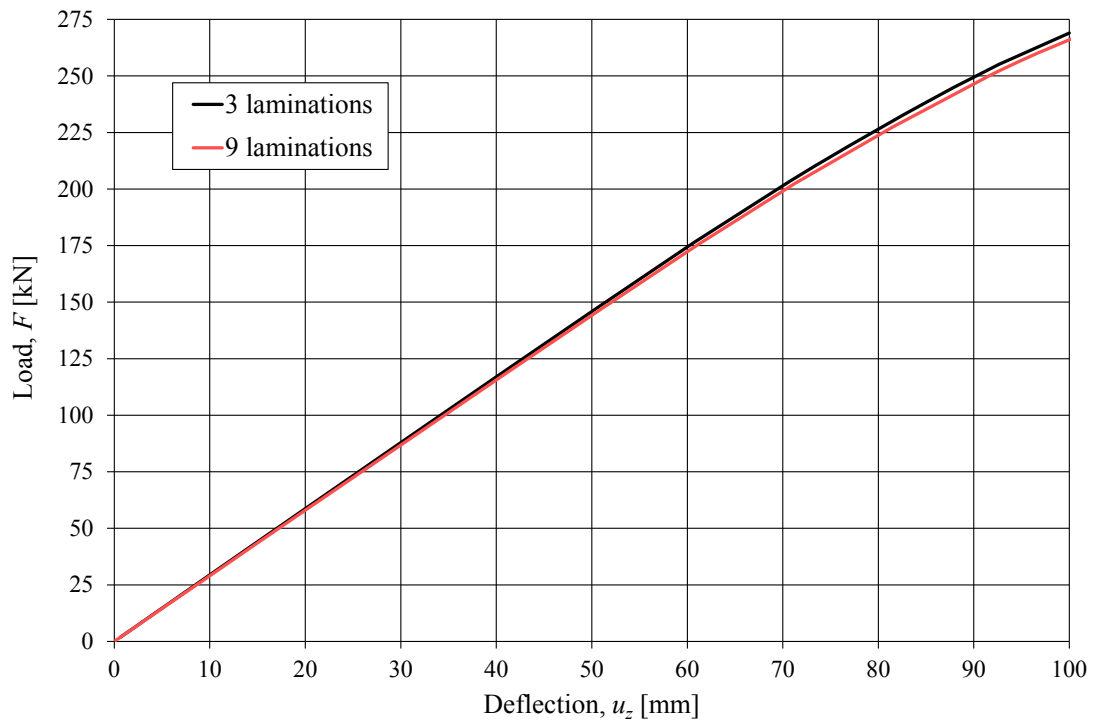


Figure 7.1 Comparison of the load-deflection behaviour of the simplified model with 3 and 9 laminations when all other parameters are constant.

## 8 Conclusion

### 8.1 General conclusions

- For analyses of non-linear problems, displacement-controlled loading is often more useful than the load-controlled method. When, as in this case, a linear elastic material model, non-linear boundaries and high load levels are combined, displacement-controlled loading has proven to be the better option in order to reach convergence.
- A finer mesh should be used at locations of stress concentrations in a model to get accurate results. This is to increase the resolution of data, e.g. when two elements in contact start slipping in relation to each other.
- The influence of different levels of pre-stress is only reflected in the order of magnitude of the results from the type of modelling that has been used in this thesis. Normalization of the outputs shows similar results for the different pre-stress levels.
- An increase in pre-stress level extends the linear behaviour of the deck.
- The modelling technique used has proven to produce results with good correlation to experimental tests. It would be powerful tool to further study and better understand the behaviour of SLT decks.

### 8.2 Suggestions for further research

#### **Elastic slip**

More studies are needed to further narrow the range of appropriate values used for elastic slip in the frictional formulation.

#### **Non-linear material property**

Anisotropic linear elastic materials were used in the full-scale models. However the real material property of timber shows non-linear behaviour. Introducing a non-linear material model would enable the simulation of failure mechanisms in an SLT deck.

#### **Detailed modelling**

A detailed model can be performed by introducing the pre-stress bars and the anchorage system. Introducing the bars in the model can give a good result by involving the dowel action when the lamination starts slipping.

#### **Butt joints**

A model can be analysed by introducing the butt joints in the full-scale model to further study the resulting effect on the overall behaviour of an SLT deck.

## 9 References

Abaqus (2010): *Abaqus 6.10 documentation*, Software Manual, Dassault Systèmes, 2010.

Barlow, J. (1976): *Optimal Stress Locations in Finite Element Models*, International Journal for Numerical Methods in Engineering, Volume 10, p. 243–251, 1976.

Bower, A. F. (2010): *Applied Mechanics of Solids*, Portland, Oregon, United States, 2010.

DiCarlantonio, G. (1988): *Prestressed timber bridges: An experimental study*, Master's Thesis, Pennsylvania State University, Pennsylvania, United States, 1988.

Ekholm, K. (2012): *Vertikalt glidbrott och stumskarvars inverkan på tvärsända träbroplattor*, Chalmers University of Technology, Göteborg 2012.

Ekholm, K. *et al.* (2011): *Non-linear analysis of a stress-laminated-timber bridge loaded to failure*, Chalmers University of Technology, Göteborg 2011.

Eurocode 5.2 (2004): *Eurocode EN 1995-2, Design of Timber Structures – Part 2: Bridges. European Standard EN 1995-2:2004*, Comité Européen de Normalisation CEN, 2004.

Forest Products Laboratory (2010): *Wood handbook - Wood as an Engineering Material*. Department of Agriculture, Forest Service, Forest Products Laboratory, Gen.Tech.Rep.FPL-GTR-190. Madison, Wisconsin 2010.

Hellgren, J. and Lundberg, L. (2011): *Finite Element Modelling of Local Interlaminar Slip in Stress-Laminated-Timber Bridges*, Chalmers University of Technology, Göteborg, 2011.

Johnson, K. L. (1985): *Contact mechanics*, Cambridge University Press, Cambridge, England, 1985.

Kalbitzer, T. (1999): *Stress-laminated-Timber Bridge Decks – Experiments regarding the Coefficient of Friction between Laminations*. Master's Thesis, Munich University of Technology, Germany, 1999.

Oliva, M. G. and Dimakis, A. G. (1988): *Behaviour of stress-Laminated Timber Highway Bridge*. Journal of Structural Engineering 114(8):1850-1869, 1988.

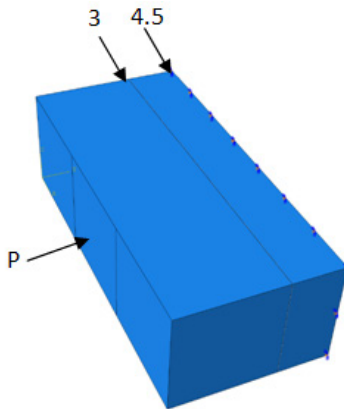
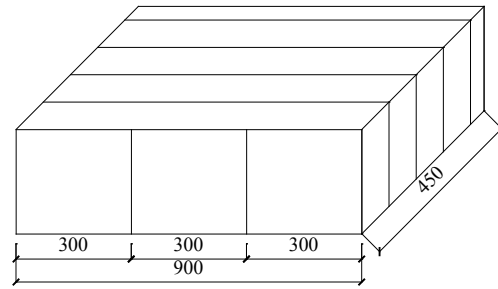
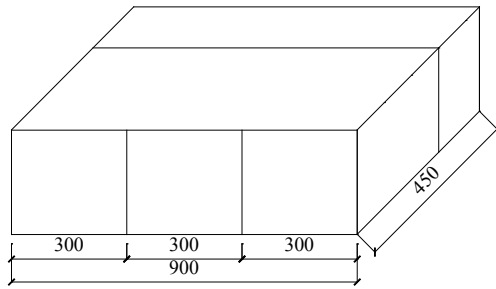
Ritter, M. A. (1990): *Timber Bridges: Design, Construction, Inspection and Maintenance*. U.S. Department of Agriculture, Forest Service: 944, Washington, D.C, USA, 1990.

Ritter, M. A., Wacker, J. P. *et al.* (1995): *Field Performance of Stress-Laminated Timber Bridges on Low-Volume Roads*. International conference on low-volume roads, Minneapolis, MN, USA, 1995.

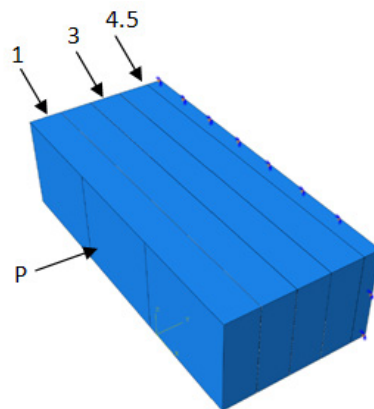
Sarisley, E. F. *et al.* (1990): *Prestress Level in Stress-Laminated Timber Bridges*, J. Struct. Eng, 116(11), 3003-3019, 1990.

Taylor, R. *et al.* (1983): *Prestressed wood bridges*. Ministry of Transportation and communication, SRR-83-01, Downsview, Ontario, Canada, 1983.

## Appendix - Simplified pre-stress model

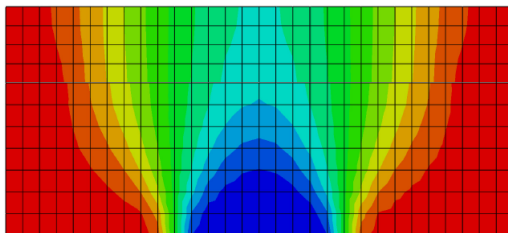


Model 1

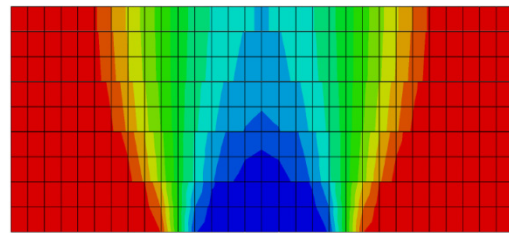


Model 2

### Isotropic



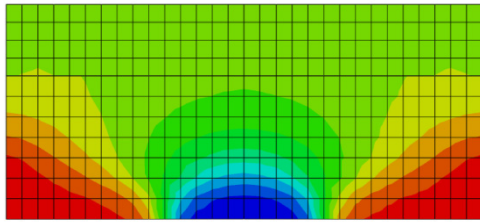
Model 1



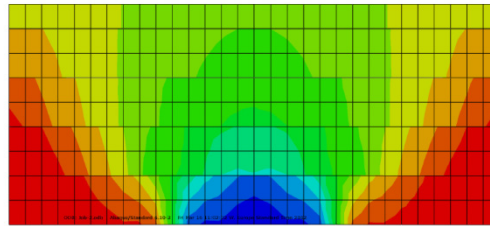
Model 2

**Anisotropic**

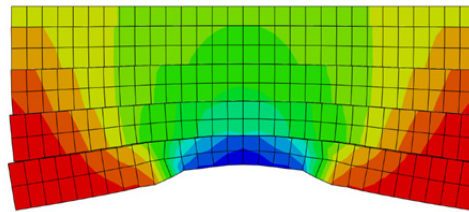
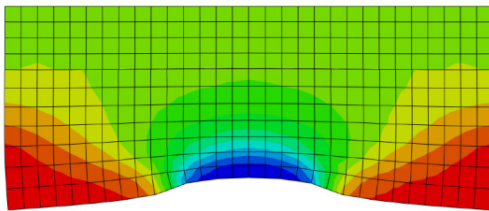
Model 1



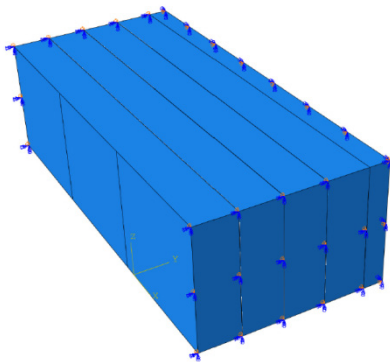
Model 2



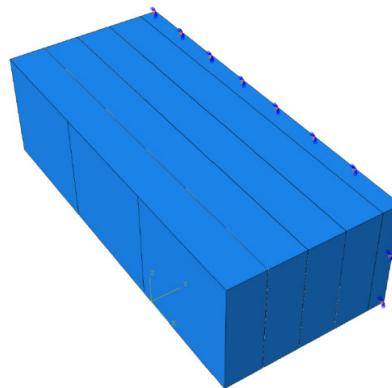
Scale factor -1



Scale factor -100

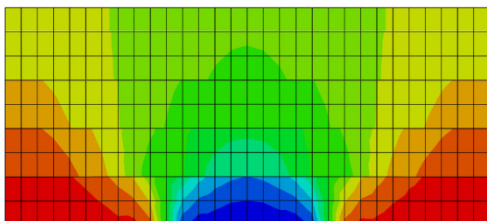


*With symmetric boundary condition*

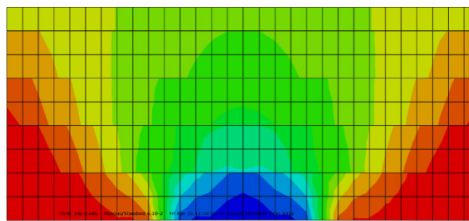


*Without symmetric boundary condition*

**Model-2**



*With symmetric boundary condition*



*Without symmetric boundary condition*

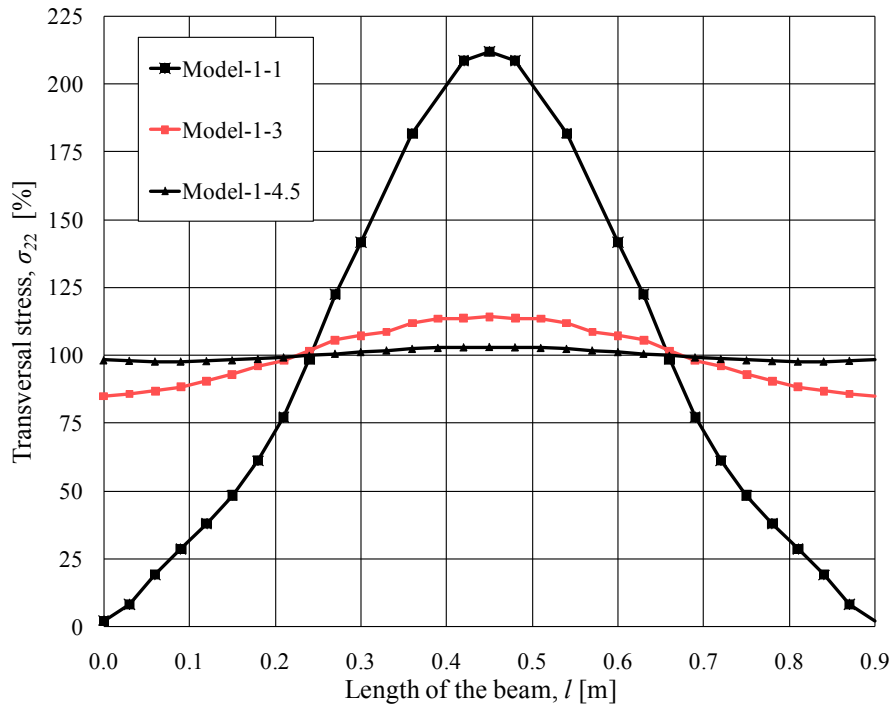


Figure 1 Pre-stress distribution for model-1 for 600 kPa pre-stressing without symmetric BC on the surface

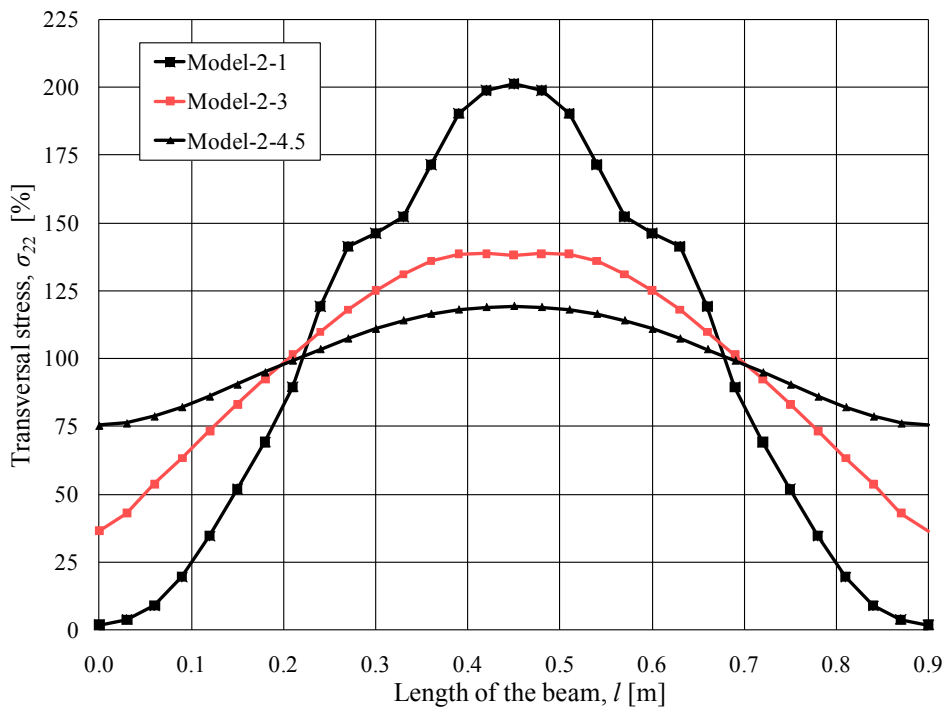


Figure 2 Pre-stress distribution for model-2 for 600 kPa pre-stressing without symmetric BC on the surface

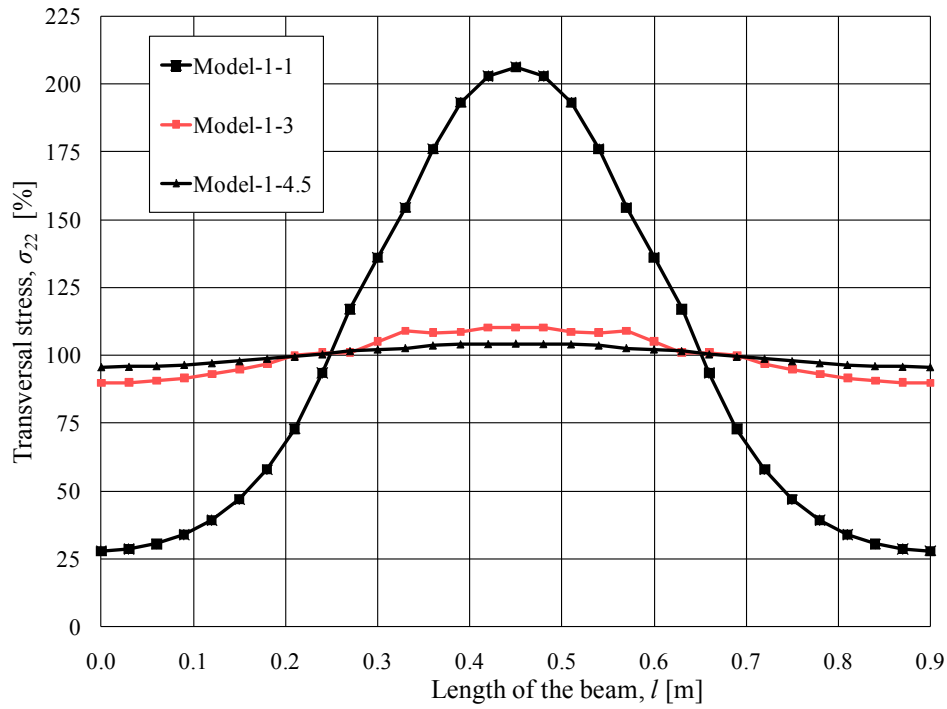


Figure 3 Pre-stress distribution for model-1 for 600 kPa Pre-stressing with symmetric BC on the surface

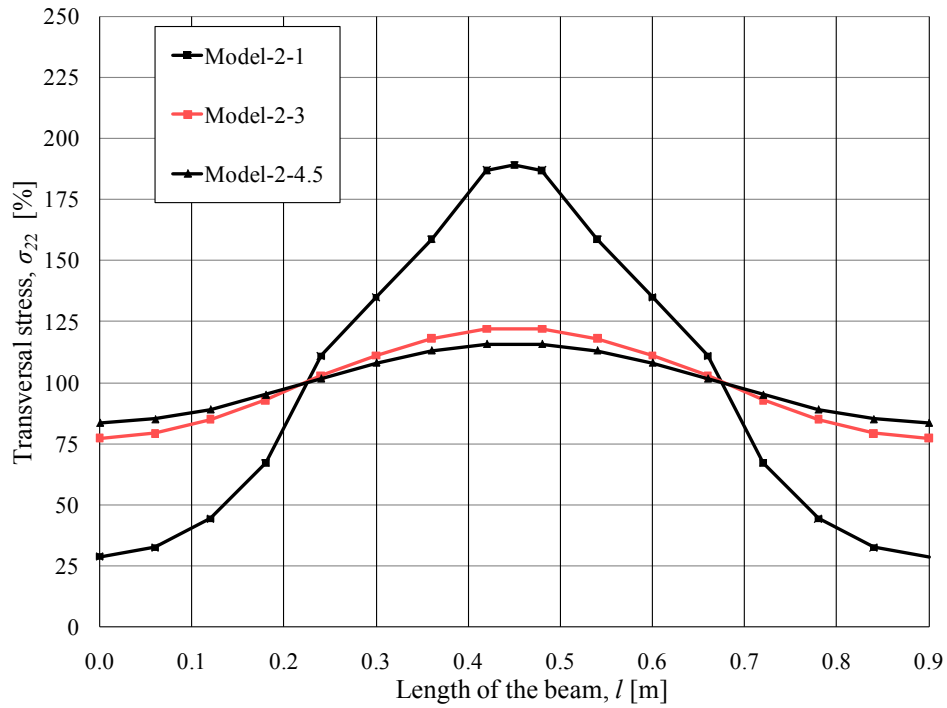


Figure 4 Pre-stress distribution for model-2 for 600 kPa Pre-stressing with symmetric BC on the surface

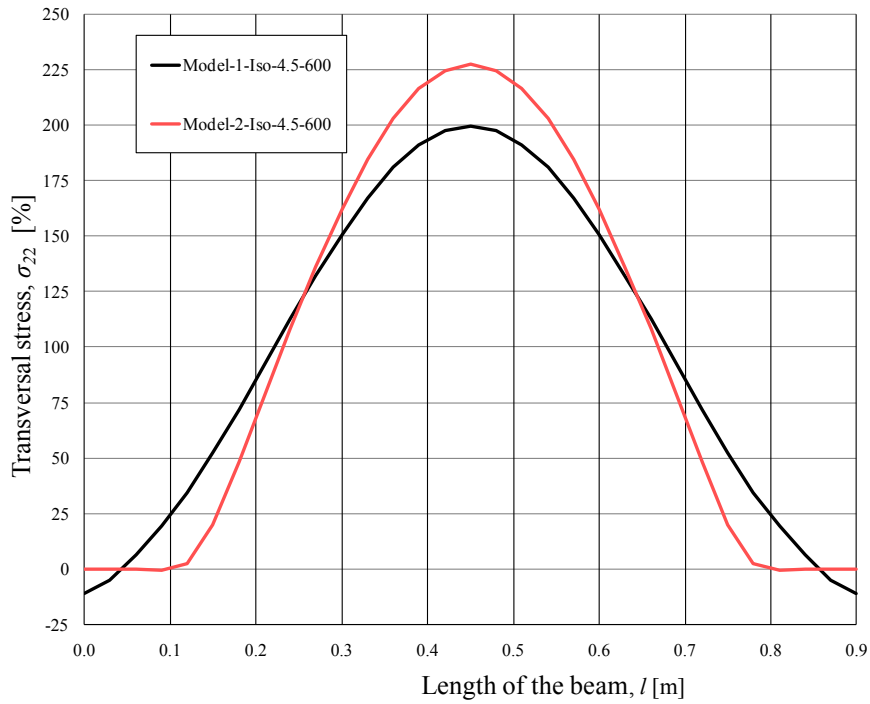


Figure 5 *Pre-stress distribution comparisons for Model 1 and Model 2 using isotropic material*

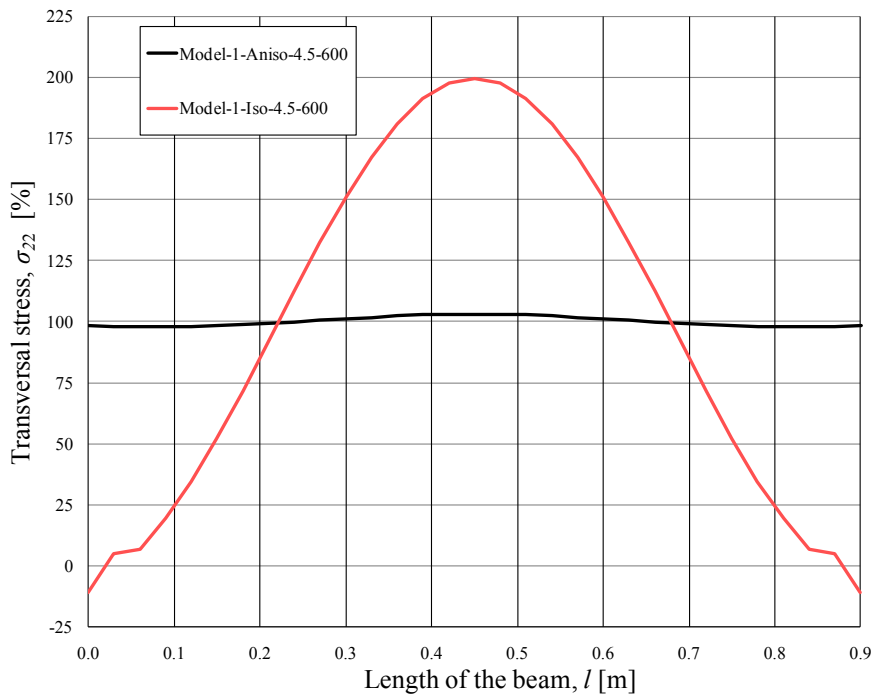


Figure 6 *Pre-stress distribution comparisons for anisotropic and isotropic material for 600 KPa pre-stressing*

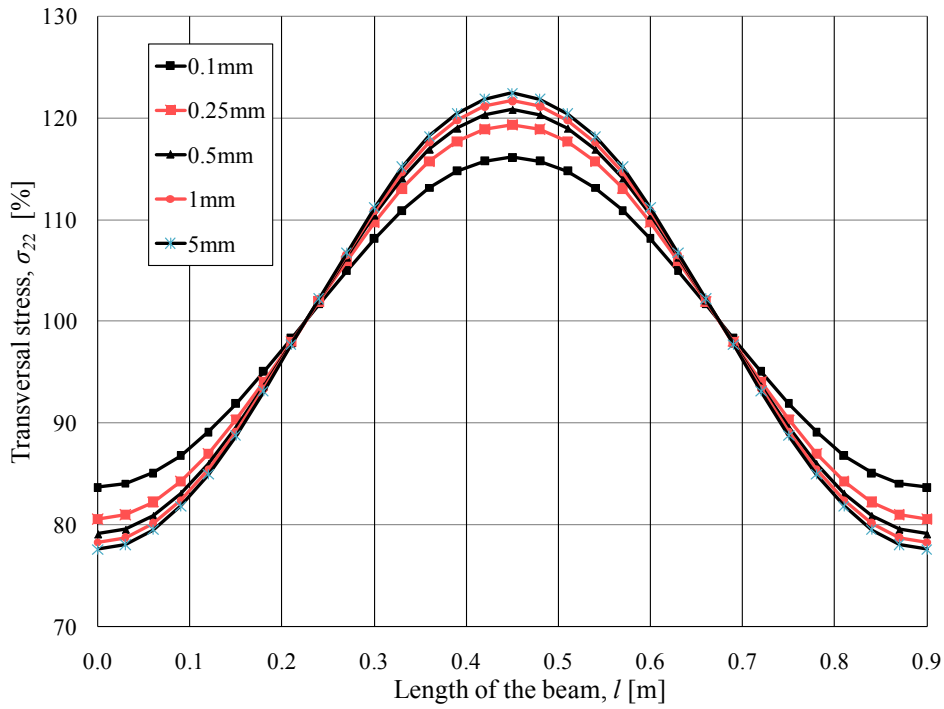


Figure 7 Pre-stress distribution comparisons for different elastic slip for 600 KPa Pre-stressing using model-2-Aniso-SYM-4.5.

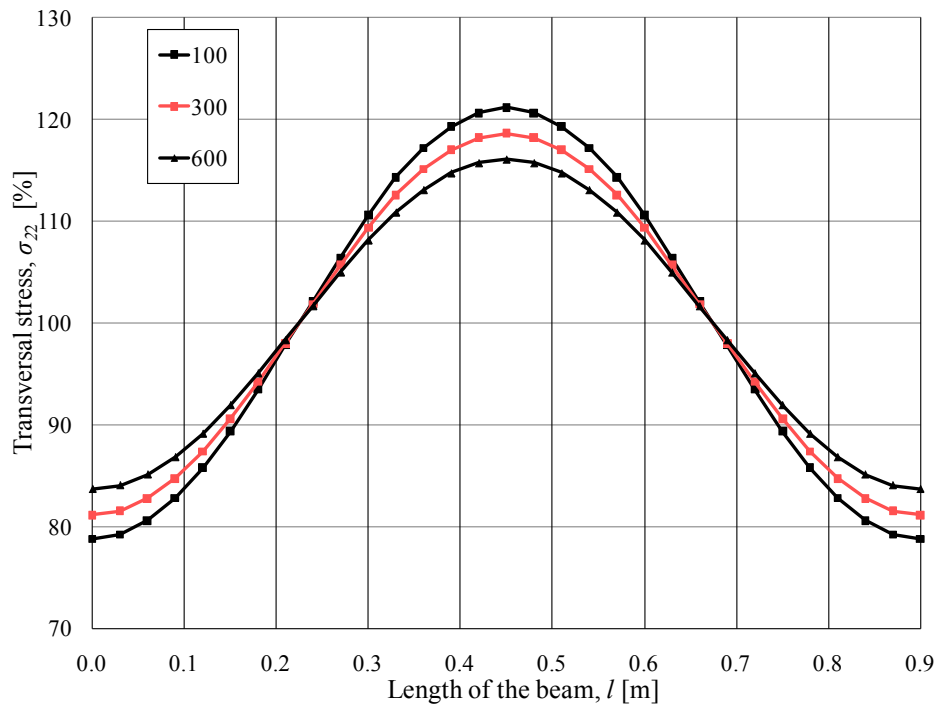


Figure 8 Pre-stress distribution comparisons for different pre-stress level using model-2-Aniso-SYM-4.5.